Title

Medical Imaging Technology Innovations to Minimize the Safety Risks of Angiography for Chronic Kidney Disease Patients

Author

Keselman, Paul

Publication Date

2016

Peer reviewed|Thesis/dissertation

Medical Imaging Technology Innovations to Minimize the Safety Risks of Angiography for Chronic Kidney Disease Patients

by

Paul Keselman

A dissertation submitted in partial satisfaction of the

requirements for the degree of

Joint Doctor of Philosophy with University of California, San Francisco

in

Bioengineering

in the

Graduate Division

of the

University of California, Berkeley

Committee in charge:

Professor Steven Conolly, Chair
Professor Chris Diederich
Assistant Professor Laura Waller

Summer 2016

Medical Imaging Technology Innovations to Minimize the Safety Risks of Angiography for Chronic Kidney Disease Patients

Abstract

Medical Imaging Technology Innovations to Minimize the Safety Risks of Angiography for Chronic Kidney Disease Patients

by

Paul Keselman

Joint Doctor of Philosophy with University of California, San Francisco in Bioengineering

University of California, Berkeley

Professor Steven Conolly, Chair

Cardiovascular Disease (CVD) is the leading cause of death in the United States. CVD is caused by a buildup of plaque in the blood vessels of the heart and brain. CVD is comorbid with Peripheral Vascular Disease (PVD), which is a buildup of plaque in the extremities and organs below the stomach. Medical imaging is a clinically indispensable tool for diagnosing CVD and PVD, as well as guiding real-time interventional procedures. Currently, the two main procedures for diagnosing CVD and PVD are X-Ray and CT angiography, both of which rely on injection of iodinated contrast agents. However, about 25% of patient undergoing these procedures suffer from Chronic Kidney Disease (CKD). For this patient subpopulation, iodinated contrast agents are risky and can lead to complete kidney failure. Physicians risk damaging patients' kidneys in order to alleviate the more imminent threat of death from a heart attack. Hence, an open challenge remains to develop a safer diagnostic angiography method that could match current methods in resolution, contrast, and speed. Here we introduce and develop two new imaging methods for imaging patients with CKD. The first method is MR Saline Angiography, an alternative Magnetic Resonance (MR) based angiographic method for coronary imaging. In combination with the inherent resolution and speed of traditional MR methods, MR Saline Angiography has the advantage of utilizing saline as a safe contrast agent. This approach is an improvement upon the commonly used Gadolinium-based contrast agent that is also toxic to patients with CKD. Using a novel electromagnetically shielded catheter and a tailored pulse sequence, we have demonstrated that MR Saline Angiography is a feasible alternative for imaging coronary arteries. The second method is Magnetic Particle Imaging (MPI), a tracer imaging modality, which images Superparamagnetic Iron Oxide nanoparticles. MPI is an emerging imaging technique with possible applications in angiography as well as targeted and non-targeted tumor imaging, hyperthermia, perufsion, cell tracking and targeted drug delivery. Here we study the feasibility of MPI as an angiographic imaging method by looking at short-term biodistribution and long-term iron clearance for two most common MPI tracers.

To my brother Eugene who will always be with me.

Contents

Contents **ii**

List of Figures **iv**

List of Tables **vi**

1 Challenges for Angiographic Imaging for Patients with Chronic Kidney Disease **1**
1.1 Prevalence and Prognosis of Chronic Kidney Disease 1
1.2 Comorbidity of Cardiovascular Disease, Peripheral Vascular Disease and Chronic Kidney Disease 1
1.3 Current Diagnostic Imaging Methods 2
1.4 Considerations in Imaging CKD Patients 3
1.5 Introducing Two Potentially Safer Approaches for Imaging Patients with CKD 3

2 Introduction: Safer Angiography with Magnetic Resonance Imaging and Magnetic Particle Imaging **4**
2.1 Basics of MRI 4
2.2 Basics of X-Space Magnetic Particle Imaging 9
2.3 Saline Angiography with MRI 12
2.4 MPI Imaging with SPIOs 13

3 Saline Angiography: Development and Evaluation of RF Shielding for Coronary Catheter **15**
3.1 Shielding Theory 15
3.2 Shielding Simulations 16
3.3 Experimental Shielding Measurements 20
3.4 Conclusions 21

4 Saline Angiography: Evaluation of Heating and Safety **22**
4.1 Conventional SAR in MRI 24
4.2 SAR and Heating in the presence of a metallic object 25
4.3 Experimental Heating Measurements 31

4.4 Conclusions 37

5 Saline Angiography: Design and Evaluation of Custom MRI Imaging Sequence 38
5.1 Robust Contrast in the presence of B_0 and B_1 variations and motion 38
5.2 Inversion Recovery Magnetization Preparation 39
5.3 Adiabatic Pulses 45
5.4 Multiple Inversion Recovery 50
5.5 Spectral Spatial Pulses 54
5.6 Flow Phantom Testing 58
5.7 Real-Time MRI with RTHawk 59
5.8 Conclusions 61

6 MPI Angiography: Experimental Evaluation of Feasibility - Tracer Biodistribution and Clearance 62
6.1 SPIO Tracers 62
6.2 Experimental Setup 63
6.3 Blood Half-Life 66
6.4 Long-term Clearance 69
6.5 Iron Localization with *ex vivo* MPI 73
6.6 Iron Clearance Validation with ICP 74
6.7 Conclusions 75

7 Conclusion 76

Bibliography 78

List of Figures

2.1 $B_1(t)$ pulse shapes . . . 5
2.2 MRI Precession and Magnetization Flip . . . 7
2.3 K-space and image space. . . . 8
2.4 MRI Pulse Sequence Diagram . . . 8
2.5 Langevin Curve . . . 10
2.6 Field-free Point (FFP) . . . 11
2.7 MPI 1D Point Spread Function (PSF) . . . 12
2.8 Neel vs. Brownian Relaxation . . . 12
2.9 Diagram of Saline Angiography . . . 13

3.1 Conceptual model of shielding . . . 16
3.2 Catheter shielding designs . . . 17
3.3 Simulation of magnetic field penetration into the shielded catheter . . . 19
3.4 Diagram depicting RF penetration measurements in three different regions of the phantom. . . . 21

4.1 Tissue Current Loops . . . 23
4.2 Simplified Cylinder Model for Estimating Conventional SAR . . . 24
4.3 COMSOL Simulation Region . . . 27
4.4 B and E fields in a quadrature coil. . . . 28
4.5 Heating simulation of rectangular phantom . . . 29
4.6 Calculated square of the voltage and the corresponding simulated heating of the continuous copper catheter vs. length. . . . 29
4.7 Electric Field simulation of segmented vs. continuous catheter . . . 30
4.8 Heating simulation of segmented vs. continuous catheter . . . 31
4.9 Heating Measurement of Tissue Phantom . . . 33
4.10 Segmented vs. Continuous tubes for heating tests. . . . 34
4.11 Measured heating curves over a 15 minute period . . . 35
4.12 Measured heating of continuous and segmented catheter versus length . . . 36

5.1 Inversion Recovery . . . 39
5.2 Flow Phantom . . . 41

5.3 MPRAGE RF pulses and corresponding M_{xy} magnetization 42
5.4 Simulated MPRAGE Signal and Contrast 43
5.5 Flow phantom images comparing saline injections with and without a shielded catheter 44
5.6 Adiabatic Pulse 45
5.7 Graph of simulated magnetization after an adiabatic pulse 46
5.8 Effect of Pulse Amplitude on Magnetization 47
5.9 Inversion profile for an Adiabatic Frequency (BW = 10 ppm) 47
5.10 Measured Signal vs. Power for an Adiabatic Pulse 48
5.11 Measured Signal vs. TI time after an Adiabatic Pulse 49
5.12 Multiple Inversion Recovery 50
5.13 Simulated longitudinal magnetization of 3 background tissues and saline during a MIR sequence 51
5.14 Sequence Diagram of MIR Sequence on the 7T Bruker Scanner 52
5.15 Oil and Cupric Sulfate Phantom demonstrating Single and Multiple Inversion Sequence 53
5.16 Predicted longitudinal magnetization for 2 solutions after a 2-Inversion MIR sequence 53
5.17 Gradient and RF Waveforms of Spectral Spatial Pulse 55
5.18 Simulated and Measured Spectral and Spatial Profiles for SS pulse 56
5.19 Comparison of water/oil phantom with and without a Spectral Spatial pulse . . 57
5.20 Flow Phantom 58
5.21 Flow Phantom Images 59
5.22 Flow Phantom and RF Catheter. 60
5.23 RTHawk images of flow phantom 60

6.1 TEM Images of MPI Tracers 63
6.2 Flowchart of the Tracer Biodistribution and Clearance Experiment 65
6.3 Short-term Biodistribution MPI Images for Ferucarbotran and LodeSpin (LS-008). 67
6.4 Short-term Biodistribution Curves for Ferucarbotran and LodeSpin (LS-008). . . 68
6.5 Long-term Clearance MPI Images for Ferucarbotran and LodeSpin (LS-008). . . 70
6.6 Long-term Clearance Curves for Ferucarbotran. 71
6.7 Long-term Clearance Curves for LodeSpin (LS-008). 72
6.8 *Ex vivo* Organ Image and corresponding MPI Images for Ferucarbotran and LodeSpin (LS-008) at day 2 and day 70 73
6.9 *Ex vivo* Organ Measurements for Ferucarbotran and LodeSpin (LS-008) at day 2 and day 70 74
6.10 ICP Organ Measurements for Ferucarbotran and LodeSpin (LS-008) at day 2 and day 70 75

List of Tables

1.1 Table of Radiation and Contrast Doses for typical diagnostic angiographies. . . 2

2.1 Table of T_1 and T_2 Relaxation Times at 1.5T and 3T. 6
2.2 Table of typical MRI parameters. 7

4.1 Table of FDA set SAR limits. 23
4.2 Table of simulation parameters. 26
4.3 Tissue Conductivity. 31

5.1 Table of parameters used in designing a Spectral Spatial Pulse 54
5.2 Table of SS Pulse Characteristics 54

6.1 Table of MPI Tracer Characteristics 63

Acknowledgments

I would like to acknowledge my entire lab, without whom, I would not be able to get as far as I did. Specifically, I would like to thank Steve for his advice and positive feedback. I would like to thank Bo for answering my countless questions. I would like to thank Elaine for keeping me on point and being so positive all the time. I would like to thank Xinyi for being a good friend and baking with me. I would like to thank Ryan, Daniel and Zhi Wei for being awesome labmates. I would like to thank Michael Wendland at the Preclinical Berkeley Imaging Center for helping me set up my MRI Imaging protocols and for always being jolly. I would like to thank Ben Inglis at the Brain Imaging Center for his good advice. I would like to thank Emine for helping me get started and for being such a warm and caring person. I would like to thank Malav for, in addition to countless other things, helping me with my first imaging phantom. I would like to thank my family and my wife Taylor for their love and unconditional support. And finally my countless friends for keeping me sane and going hiking and climbing with me.

In addition, I would also like to acknowledge the funding sources: NIH 1R01 EB013689, CIRM RT2-01893, Keck Foundation 009323, NIH 1R24 MH106053 and NIH 1R01 EB019458, and ACTG 037829.

Chapter 1

Challenges for Angiographic Imaging for Patients with Chronic Kidney Disease

1.1 Prevalence and Prognosis of Chronic Kidney Disease

Chronic Kidney Disease (CKD) is a gradual loss of kidney function that usually afflicts older adults over the age of 60. In the United States, about 10% (or 26 million) of adults have CKD and millions of others are at increased risk [1]. This statistic is worse in adults over 60; 22% of patients in their 60's and 47% of patients over 70 have CKD [2]. Without early detection and treatment of underlying causes (such as high blood pressure or high cholesterol levels), progression of kidney disease will lead to severe loss of function and even kidney failure. Clinicians use glomerular filtration rate (measured in mL/min/1.73 m^2) to estimate kidney function. A persistent presence of proteinuria (urine albumin or serum creatinine) is an indication of CKD. CKD has 5 stages of severity: Stage 1 GFR > 90; Stage 2 GFR = 60-89; Stage 3 GFR = 30-59; Stage 4 GFR = 15-29; and Stage 5 GFR < 15 [2]. Stage 5 patients required dialysis or a kidney transplant to survive. Heart disease is the major cause of death for all patients with CKD [1].

1.2 Comorbidity of Cardiovascular Disease, Peripheral Vascular Disease and Chronic Kidney Disease

CKD is often comorbid with cardiovascular disease (CVD), and peripheral vascular disease (PVD) [3, 4]. CVD is the blockage of blood vessels that supply oxygen and nutrients

to the heart and brain. On the other hand, PVD typically affects blood vessels that supply the arms, legs, and organs located below the stomach. The blockage occurs when cholesterol combines with fat and calcium in the blood, and slowly builds up and hardens in the vessels. Like CKD, CVD and PVD are chronic and present slowly over time. According to the American heart association, CVD is the leading global cause of death, accounting for more than 17.3 million deaths per year [5]. It is also estimated that, globally, over 200 million people are living with PVD [6]. The majority of cerebrovascular and peripheral vascular problems can be identified through diagnostic imaging tests.

1.3 Current Diagnostic Imaging Methods

Currently, the two main imaging techniques for diagnosing CVD and PVD are X-Ray fluoroscopic angiography and CT angiography [7]. Both of these techniques rely on injection of iodinated contrast agents. X-ray angiography has three principal risks: ionizing radiation, trauma from the arterial catheterization, and risks associated with the contrast agent, iodine. CT angiography shares the ionizing radiation risk, and the risk of iodine. It is predicted that 2% of future cancers will be caused by radiation from CT exposure, resulting in about 15,000 deaths annually [8]. Doctors typically weigh these risks on a patient-specific basis. Iodine is by far the most significant concern in the large subpopulation of patients who have Chronic Kidney Disease (CKD). These patients may suffer permanent kidney damage from even a single iodinated contrast study [9, 10, 11].

Table 1.1 shows typical radiation and iodinated-contrast dosage for common angiography procedures. Typical procedure is several times greater than the average background exposure and requires orders of magnitude more Iodine injection then the average dietary yearly intake.

Procedure	Radiation Dose (miliseiverts)	Contrast Dose (grams of Iodine)
X-Ray Coronary Angiography	15	35
CT Coronary Angiography	16	6 to 45
X-Ray Peripheral Angiography	10	3 to 21
CT Peripheral Angiography	7	35 to 40
CT Cerebral Angiography	14	26 to 35
Chest X-Ray	0.1	N/A
Average Yearly Dose	3	N/A
Recommended Yearly Intake	N/A	0.05

Table 1.1: Table of typical radiation and iodinated-contrast dosage for common angiography procedures. Typical procedure is several times greater than the average background exposure and requires orders of magnitude more Iodine injection then the average dietary yearly intake. [8, 12, 13, 14, 15, 16, 17, 18, 19, 20].

1.4 Considerations in Imaging CKD Patients

Roughly 25% of patients presenting to the X-ray angiography suite suffer from CKD [21]. Late stage CKD patients have a very high risk (30%-40%) of developing Contrast Induced Nephropathy from injection of the iodinated contrast agent [11], effectively tripling their 1-year mortality rate from 7% (for patients without CKD, but with CIN) to 24% (for patients with CKD and CIN) [3]. In many of these cases patients will have to be put on permanent kidney dialysis [9]. The risk of CID is considered clinically significant for Stage 3 CKD or above [22]. In an informal interview, five out of five cardiologists at Stanford and UCSF stated that given the risks of radiation, catheter trauma and contrast, iodine was by far the most significant risk for CKD patients undergoing an iodinated X-ray angiography study.

An obvious alternative for CKD patients is to undergo a Magnetic Resonance Angiogram (MRA). This has an advantage of avoiding ionizing radiation and iodinated contrast. However, a clinically relevant contrast between the blood vessels and the background tissue typically requires an injection of a Gadolinium (Gd) based contrast agent. Unfortunately, Gd induces Nephrogenic Systemic Fibrosis (NSF) in 9% of late-stage CKD patients, and NSF is fatal in 60% of the cases [23, 24]. Therefore Gd based contrast agents are contraindicated for this patient population [25, 26, 8]. **For the CKD subpopulation, we simply have no safe contrast agent. Due to the high chance of comorbidity of CKD with CVD and PVD, these patients are frequently in need of angiograms, so millions of risky iodinated angiograms are performed each year on CKD patients.** An open biomedical imaging challenge remains to develop a safe and robust imaging method for diagnosing CVD and PVD in CKD patients.

1.5 Introducing Two Potentially Safer Approaches for Imaging Patients with CKD

In this work, I describe two potentially safer imaging methods for imaging patients with CKD. The first method is for imaging Coronary Artery Disease. My method is a catheterized MRI angiogram using a much safer contrast agent – saline. My goal in this work is to show that this approach is not only feasible, but also a safer angiography method for CKD patients – one with no ionizing radiation risk and more importantly no contrast agent risk.

The second method is using a novel imaging modality, currently in development, called Magnetic Particle Imaging (MPI), which relies on injection of superparamagnetic iron oxide (SPIO) nanoparticles into the body. SPIOs are excreted through the liver and spleen rather than the kidneys. Therefore, these are safe for patients with CKD and have even been approved by the US Food and Drug Administration (FDA) as a treatment of anemia in this population [27]. A 2010 FDA report showed greater mean blood hemoglobin concentration (Hgb) in CKD patients on an SPIO containing drug called Ferumoxytol as compared to Hgb in patients on oral iron supplements [28]. In this work, I show that MPI is able to visualize vasculature *in vivo*, and then track eventual clearance of the nanoparticles from the system.

Chapter 2

Introduction: Safer Angiography with Magnetic Resonance Imaging and Magnetic Particle Imaging

In this section I will first introduce Magnetic Resonance Imaging (MRI) and Magnetic Particle Imaging (MPI), and then introduce application of these techniques for safer iodine-free Angiography aimed at patients with CKD.

2.1 Basics of MRI

MRI uses a uniform magnetic field, $\mathbf{B_0}$, Radio Frequency (RF) field $\mathbf{B_1}$, and linear gradient fields, $\mathbf{G}$, to image the distribution of certain atoms in the body. Atoms with odd number of protons possess a nuclear angular momentum (spin) and can be imaged with MRI. All clinical MRI scanners look at hydrogen (^{1}H) atoms, which is the most abundant atom in living organisms. However, atoms such a phosphorus (^{31}P), carbon (^{13}C), and fluorine (^{19}F) can also be detected with properly tuned hardware. For the purpose of this discussion we will assume that we are only imaging ^{1}H molecules, and refer to them as "spins".

In the absence of an external magnetic field, spins are oriented in different directions and have a bulk magnetic moment of zero. Once a field is applied, spins will reorient themselves to a new equilibrium, and there will be a net magnetic moment in the direction of the external magnetic field. The spins will also exhibit resonance at a frequency called the Larmor frequency, f, where

$$f = \frac{\gamma}{2\pi} B \tag{2.1}$$

where γ is a constant called the gyromagnetic ratio (for ^{1}H, $\gamma/2\pi = 42.58$ MHz/Tesla).

A $\mathbf{B_1}$ field at the Larmor frequency, will "excite" the spins causing them to produce a detectable signal at the same frequency. Essentially $\mathbf{B_1}$ applies a torque which rotates the magnetization vector away from equilibrium. The angle of rotation, or flip angle, depends

on the strength of the B_1 field and its duration. These RF pulses can be of many different shapes, $B_1(t)$, depending on the application. The flip angle, θ, is given by

$$\theta = \gamma \int_0^\tau B_1(t)\, dt \tag{2.2}$$

where τ is the pulse duration (usually measured in ms). Figure 2.1 shows two pulse shapes commonly used in MRI – Rectangular Pulse (hard pulse) and Sinc Pulse. In the simplest case where $B_1(t)$ is a rectangular pulse of magnitude $|B_1|$ and duration τ, the flip angle is given by

$$\theta = \gamma |B_1| \tau \tag{2.3}$$

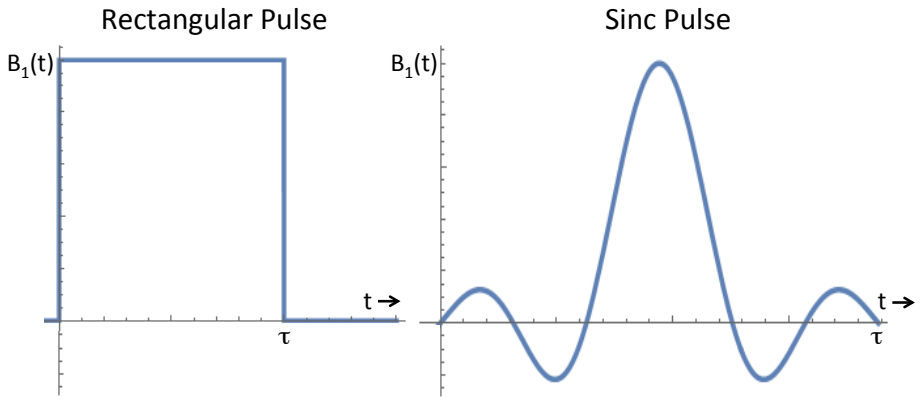

Figure 2.1: Example of two $B_1(t)$ pulse shapes commonly used in MRI.

Once the excitation field, $\mathbf{B_1}$, is turned off, the spins will precess back to equilibrium. This is called relaxation, and the time constant describing the return of the magnetization vector back to equilibrium is called T_1 (also called the spin-lattice relaxation time). The spins will also interact with each other and dephase – this decay time is called T_2 (also called spin-spin relaxation time). Both relaxation times are sensitive to the immediate environment of the spins and change depending on the tissue. In humans, T_1 times are on the order of a few hundred to a few thousand milliseconds, and the T_2 times are on the order of tens to hundreds of milliseconds. Table 2.1 is a table of T_1 and T_2 times for some tissue in the body. This is the source of contrast in typical clinical MRI images.

From Faraday's Law, a precessing (or rotating) magnetization vector will induce an electromotive force in a properly tuned and oriented coil. In order to pickup the signal the coils are oriented perpendicular to the direction of the main magnetic field. Only the magnetization vector perpendicular to the plane of the coil will be detected. Separate coils can be used to excite and receive signal, or the same coil can switch modes and do both jobs. The time signal received by a coil is called the free induction decay (FID).

	1.5T		3T	
Tissue	T_1 (ms)	T_2 (ms)	T_1 (ms)	T_2 (ms)
Muscle	1008	44	1412	50
Fat	288	165	371	133
Blood	1441	290	1932	275
Heart	1030	40	1471	47
Liver	576	46	812	42
Kidney	690	61	1194	56
White Matter	884	79	1084	69
Gray Matter	1124	95	1820	99

Table 2.1: T_1 and T_2 Relaxation times at 1.5T and 3T [29, 30].

By convention the $\mathbf{B_0}$ field in MRI points along the (+) z-direction (or longitudinal direction). This is also the direction of the net magnetization vector at equilibrium. When an excitation pulse is applied, a portion of the available magnetization is tipped into the xy-plane. The component of magnetization left pointing along the z-direction is called the longitudinal magnetization, M_z, and the component of magnetization tipped into the xy-plane is called the transverse magnetization, M_{xy}. In general, the behavior of the magnetization vector, $\mathbf{M}$ is given by the Bloch Equation

$$\frac{d\mathbf{M}}{dt} = \mathbf{M} \times \gamma\mathbf{B} - \frac{M_x\hat{i} + M_y\hat{j}}{T_2} - \frac{(M_z - M_0)\hat{k}}{T_1} \tag{2.4}$$

where $\mathbf{B}$ is the sum of the total magnetic fields applied, M_0 is the initial equilibrium magnetization, and T_1 and T_2 are the relaxation times described above. Note that only the M_{xy} component is detected by the receive coil. Figure 2.2 shows a magnetization vector under the influence of a $\mathbf{B_1}$ field in the x-direction. A $\mathbf{B_1}$ field of long enough duration or large enough magnitude will be able to rotate the net magnetization vector 180° or opposite the direction of the main magnetic field, $\mathbf{B_0}$.

With only the $\mathbf{B_0}$ field, all the spins will precess at the same frequency, and the receive coil will pick up the net signal from all the excited spins. In this situation, it is not possible to spatially localize the signals. In MRI, the spatial localization is achieved by applying linear gradient fields along the three spatial axes. These fields are added to the main magnetic field so that the total field seen by the spins at some location, x, is given by

$$B_x = B_0 + G_x x \tag{2.5}$$

where x is one of the three spatial direction x,y and z. The frequency of the the spins now becomes a function of position, such that

$$f = \frac{\gamma}{2\pi}(B_0 + G_x x) \tag{2.6}$$

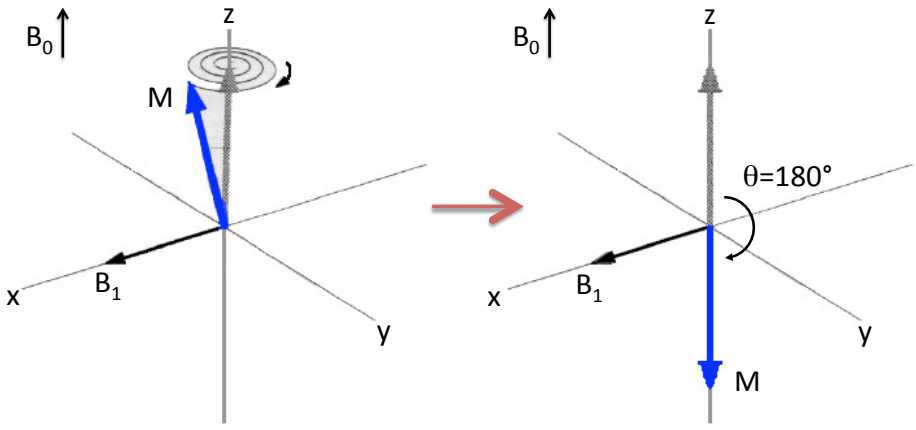

Figure 2.2: A diagram depicting a net magnetization precessing away from pointing along the direction of the main magnetic filed, B_0 (+z direction). A flip of $\theta = 180°$ yields a net magnetization that points opposite the direction of B_0 (-z direction)

Now, if we turn on the gradient our receive coil will pick-up a range of frequencies. A Fourier transform of the FID signal will determine the contribution from each frequency, which in turn will map to a particular position. With the gradients, it is also possible to excite only certain frequencies–which gives rise to spatially selective excitation.

Table 2.2 shows typical clinical and pre-clinical values of the imaging parameters.

Parameter	Clinical Value	Pre-clinical Value
Main Field magnitude, B_0	1.5T, 3T	7T, 9.4T
RF field magnitude, $\|B_1\|$	few μT	tens μT
Gradient strength, G	20 mT/m to 80 mT/m	100 mT/m to 400 mT/m
Spin-Lattice Tissue Relaxation, T_1s	100 ms to 4000 ms	
Spin-Spin Tissue Relaxation, T_2s	10 ms to 100 ms	

Table 2.2: Typical clinical and pre-clinical MRI scanner parameters.

An MRI image is collected in the spatial frequency domain, called k-space. A Fourier Transform is taken to reconstruct the image (see Figure 2.3). A series of temporally separated RF pulses combined with switching gradient fields are used to acquire an image. This series of pulses is a called an MRI pulse sequence. A pulse sequence can be used to tease out different physical properties from the object of interest. The image depends on a variety of system and physical factors, such as pulse and gradient strengths, excitation and reception timing, as well as the desired contrast, resolution and signal-to-noise ratio (SNR). Figure 2.4 shows a typical pulse sequence. Shown are the RF transmit (θ) and RF receive signals (FID) and the three orthogonal gradients (G_{Read}, G_{Phase}, G_{Slice}) versus time. Briefly, the read and phase gradients are responsible for traversing the spatial frequency content of the image,

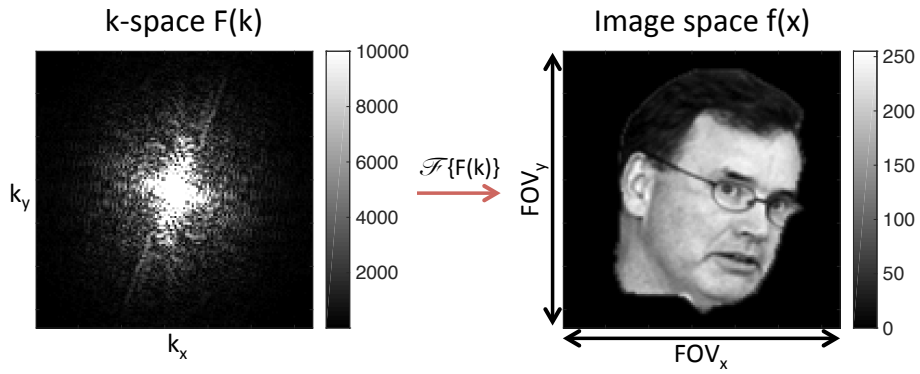

Figure 2.3: On the left is a typical k-space image. A Fourier transform reconstructs the acquired image (image on the right). The field of view, FOV_x and FOV_y depend on the sampling, Δk_x and Δk_y, along k_x and k_y such that $FOV_x = 1/\Delta k_x$ and $FOV_y = 1/\Delta k_y$

,

while the slice gradients pick out an imaging slice from the field of view (FOV). Also shown are timing parameters TR (repetition time), and TE (echo time).

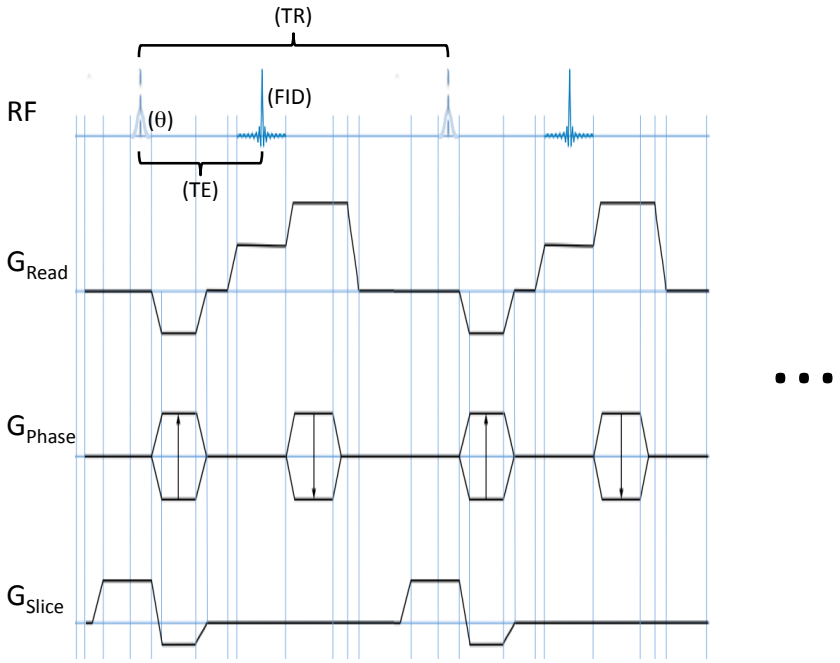

Figure 2.4: A depiction of an MRI pulse sequence diagram.

The main source of noise in MRI is thermal noise arising from random electrical fluctuations in the body and coil. Out of the two, the body is the dominant source–MRI is said to

be body noise dominant. The signal to noise in the MRI image is given by

$$SNR \propto (\delta_x)(\delta_y)(\delta_z)\sqrt{\text{total readout interval}}\, f(\rho, T_1, T_2) \tag{2.7}$$

where δ_i is the image voxel size, total readout interval is the time over which the receiver coil is collecting data, and $f(\rho, T_1, T_2)$ is a pulse sequence dependent function that determines the signal amplitude during readout.

There are several safety concerns that arise in MRI. The first, is the force that might be exerted by the main static magnetic field on any metallic materials. Even non-ferrous object are subject to forces when they move through the field. Primarily, this effect should be considered when dealing with implanted devices, especially near soft tissue. The second is heating due to high frequency changing magnetic fields during RF excitation. This should be considered for any conductive material introduced into the human body. And finally, the third is peripheral nerve stimulation caused by switching of linear gradient magnetic fields used for spatial encoding. Heating and peripheral nerve stimulation is of concern when developing new pulse sequences that require fast gradient switching.

2.2 Basics of X-Space Magnetic Particle Imaging

MPI [31, 32] is an emerging tracer imaging modality that directly images Superparamagnetic Iron Oxide nanoparticles (SPIOs). As with other tracer modalities such as Positron emission tomography (PET) and Single-photon emission computed tomography (SPECT), only the tracer produces signal, with no signal from background tissue. This property inherent to the modality results in high contrast-to-noise ratio.

Due to its high imaging contrast, MPI has exceptional promise for applications such as cell tracking [33, 34], angiography [35] and perfusion [36]. Currently, MPI images particles with a core diameter of around 25 nm made primarily of magnetite Fe_3O_4. These particles are then coated and functionalized, extending their hydrodynamic radius to about 100 nm. Some commonly used coating include dextran, cyclodextran and polyethylene glycol (PEG) [37]. The signal is linear with respect to amount of tracer [33], is not attenuated by tissue, has unlimited tracer magnetization half-life, and poses no radiation risk [38]. There are currently two different approaches in doing MPI. One approach, called X-Space MPI [39], was developed by our lab at Berkeley and is the one I will describe here. Another approach, called the system function approach, was developed by Philips [31].

In the absence of a magnetic field, SPIOs are randomly oriented in space. However, in an externally applied magnetic field these particles will saturate and orient themselves along the direction of the magnetic field. The net magnetization, M in A/m, of an ensemble of particles is described by the nonlinear Langevin equation

$$M = Nm\left(\coth\left(\frac{\mu_0 mH}{K_B T}\right) - \frac{k_B T}{\mu_0 mH}\right) \tag{2.8}$$

where N is the density of nanoparticles in the sample (units: particles/m^3), m is the magnetic moment (units: Am^2), μ_0 is the permeability of free space ($4\pi \times 10^{-7}$ H/m), k_B is the Boltzmann's constant (1.38×10^{-32} J/K), H is the applied magnetic field (units: A/m), and T is the absolute temperature (units: K). The Langevin curve is shown in Figure 2.5.

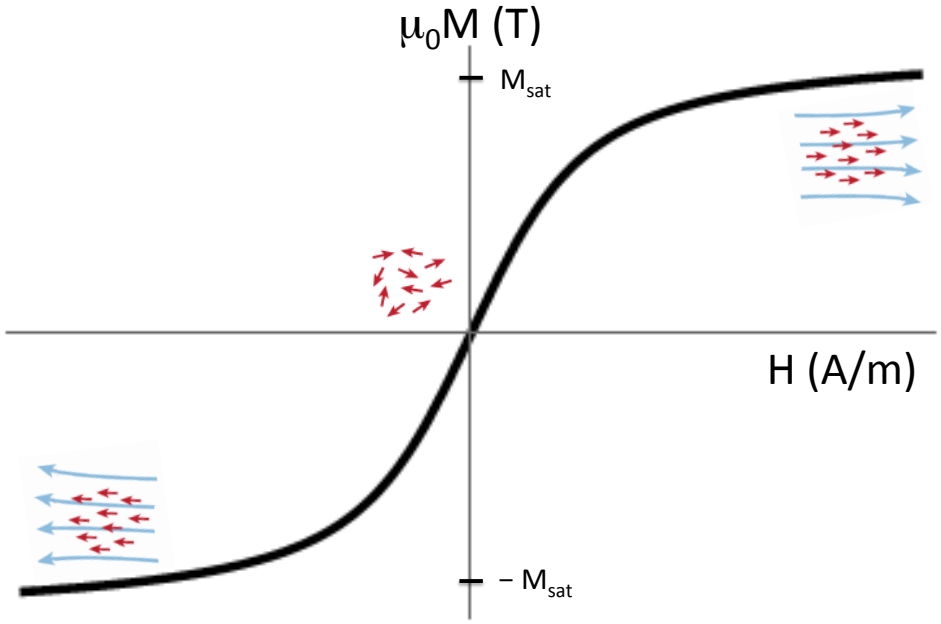

Figure 2.5: Langevin function describing the behavior of SPIOs in an external magnetic field. In the presence of negative applied field (left in diagram), particles point to the left. In the presence of positive applied field, particles point to the right. With no external field ($H \approx 0$), the particles are randomly oriented with a net magnetization of 0.

The ensemble particle magnetization can be made to traverse the Langevin curve by applying a high frequency (tens of kHz) sinusoidal field with an electromagnetic coil, called a transmit coil. As the particles flip from one side of the curve to the other, they generate a signal that can be detected by a nearby electromagnetic pickup coil, called a receive coil. Due to the non-linear nature of the particle response to the applied field, the received signal will be at harmonics of the transmit frequency.

As in MRI, the aforementioned approach will detect signal from all the particles within the receive coil without being able to discern the spatial location of the particles. In order to localize the detection to a specific region, and thus be able to form an image, a high static magnetic field gradient is utilized. In MPI, this is done with a combination of permanent magnets and electromagnetic coils. The simplest two-coil system is illustrated in Figure 2.6. With the two coils facing each other, and currents running in opposite direction, there will be a region of zero field between the coils – this is called a field-free point (FFP). The FFP

can be translated in 1D by varying current in the electromagnets. By adding another series of coils, the FFP can be translated within the imaging volume. As scanning occurs, only SPIO inside the field-free point are able to respond to the rapidly shifting transmit field and produce the signal. Everywhere outside the FFP, the particle magnetization will be saturate and produce almost no signal. The detected signal can then be assigned to specific location in space and a 3D image made.

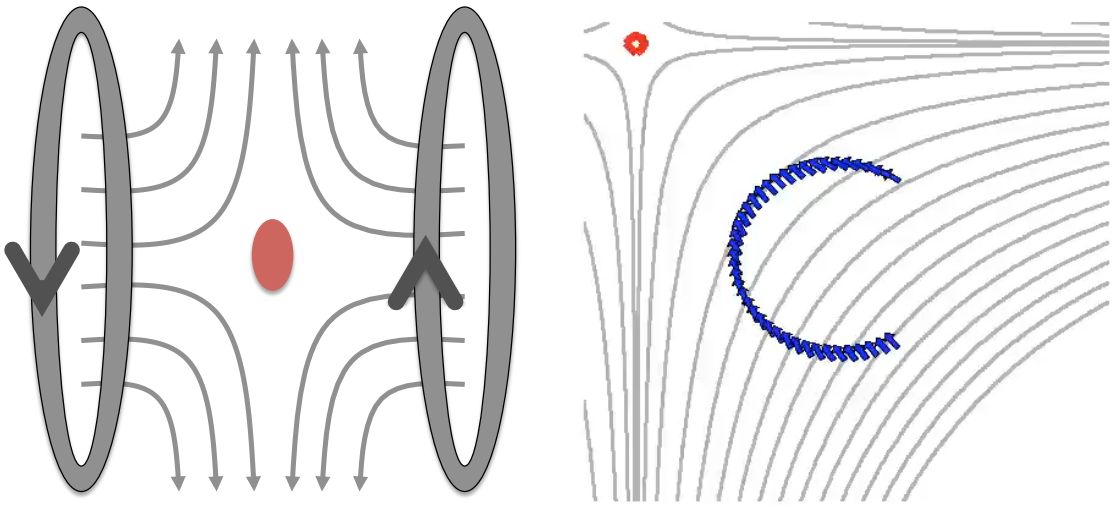

Figure 2.6: (Left) Illustration of a field-free point (FFP) generated by two opposing magnets. (Right) Illustration of SPIOs reorienting themselves in response to the movement of the FFP.

It turns out that the one-dimensional point spread function (PSF) in MPI is the derivative of the Langevin curve. The PSF depends on a variety of factors including particle physics as well as the system hardware. Stronger field gradient and bigger core particles produce smaller Full Width Half Max (FWHM), resulting in higher spatial resolution. Figure 2.7 illustrates the PSF in MPI.

Since the SPIO response to the transmit field is almost instantaneous (adiabatic assumption), both transmit and receive occur simultaneously. This results in a phenomenon called direct feedthrough, where the transmit field is detected along with the particle signal. To combat direct feedthrough, excitation frequency (first harmonic) filtering and low noise broadband electronics are required.

In reality, the response of SPIOs to the field is not instantaneous, but is influenced by thermal fluctuation as well as resistance to rotation. This phenomenon is known as relaxation. In general, particles can undergo two types of rotations to align with the magnetic field: Néel and Brownian. Particles under 25 nm core diameter are thought to undergo mostly Néel relaxation, while bigger particles undergo mostly Brownian relaxation. In Néel relaxation, the magnetic domain is reoriented within the magnetic material. On the other hand, in Brownian relaxation the entire particle undergoes rotation (See Figure 2.8).

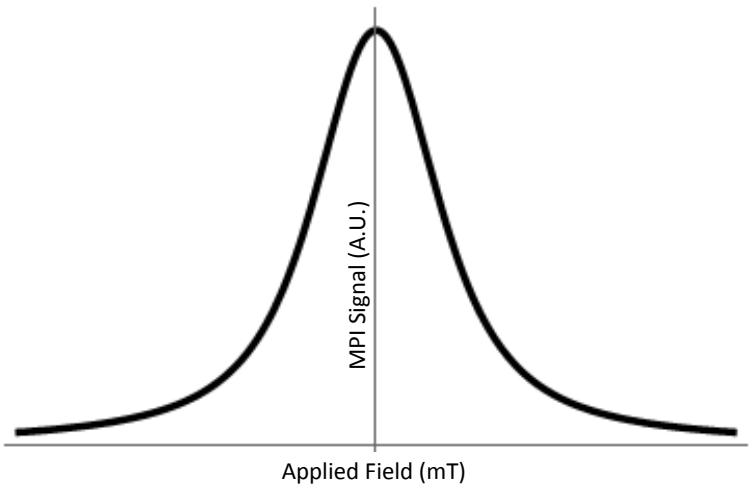

Figure 2.7: Illustration of the 1D point spread function (PSF) in MPI. The 1D PSF is the derivative of the Langevin curve.

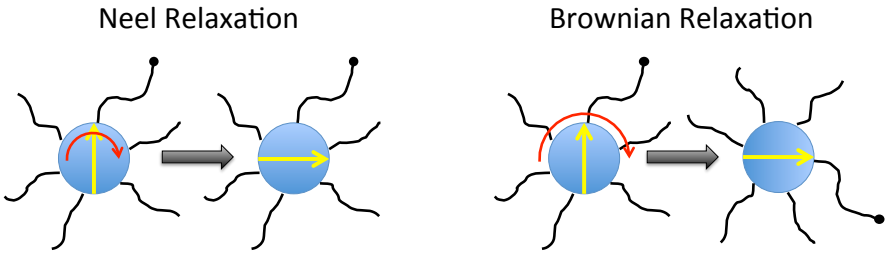

Figure 2.8: Illustration depicting Neel Relaxation (domain is reoriented within the magnetic material) vs. Brownian Relaxation (entire particle is reoriented).

2.3 Saline Angiography with MRI

Here I describe an alternative MRI based angiographic method for coronary imaging one that does not only provide great resolution, contrast and speed, but also has an advantage of using non-ionizing radiation and a safe contrast agent. Similar to X-Ray angiography, our contrast agent is delivered through an arterial catheter directly into the patients coronary tree. Catheter based angiograms have a non-trivial risk, with complications arising only in 1.35% of the time [40]. However, as described above, this risk is very small compared to risk from iodine and gadolinium injections for patients with CKD. Our catheter, unlike traditional catheters, will have a paper-thin metallic layer designed to shield out Radio Frequency (RF) excitation pulses present in the MRI environment. Saline is then injected through the catheter directly into the coronary arteries. To achieve clinically significant contrast, the background tissue, composed mainly of myocardial muscle, pericardial fat and

blood is almost perfectly nulled with a specially designed RF sequence. The saline coming out of the RF-catheter is electromagnetically shielded from the nulling pulses and thus has a high signal relative to the nulled background tissue. Our new angiography method shows promise for robustness to motion and magnetic field inhomogeneity, two of the predominant technical challenges in MRI. Figure 2.9 is a diagram of the saline angiography approach.

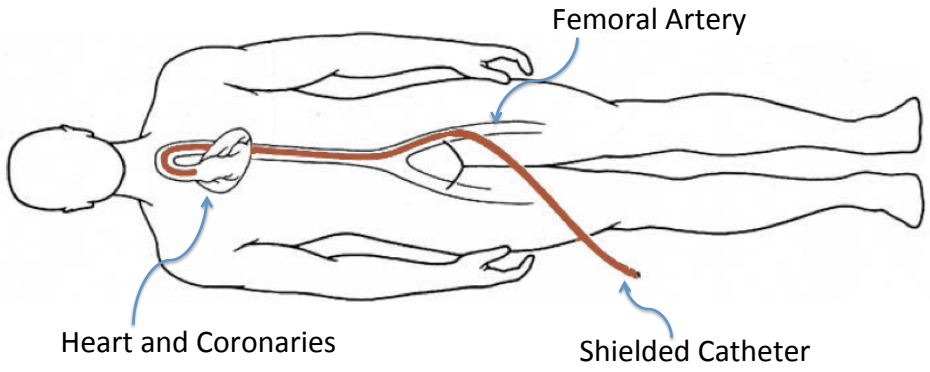

Figure 2.9: Diagram of Saline Angiography. As with current X-Ray angiography techniques, a catheter is inserted into the patients femoral artery and then advanced to the coronary tree. Saline is then injected and an image acquired with an MRI pulse sequence specifically tailored to produce high contrast between the injected saline and the background tissue.

In this new angiography method, the speed and the resolution matches existing MRI techniques. However, our method should surpass existing angiography techniques in safety, contrast and robustness. We use a much safer saline contrast agent, instead of the toxic Gadolinium based contrast agents that are currently used. The key innovation is the use of the RF-shielded catheter coupled with an optimized nulling MRI pulse sequence that not only allows for clinically relevant contrast between the saline and background tissue, but also is designed to prevent harmful metallic heating in the time-varying magnetic fields used in MRI.

To reiterate, the aim of this project was to demonstrate that this approach was able to provide a clinically relevant and robust contrast mechanism, while remaining safe. Specifically, I demonstrated that our specially designed RF-catheter did not heat above safety limits, while still able to effectively shield out the RF excitation pulses and produce a high contrast image.

2.4 MPI Imaging with SPIOs

As mentioned previously, SPIO nanoparticles are one of the only safe imaging tracers for patients with CKD. Currently, SPIO nanoparticles are mostly used for MRI. However, SPIOs show up as T2* dropouts (Negative Contrast), which is very challenging to distinguish from

regions with naturally dark MRI tissues (e.g., lungs, bones, tendons). This poses a barrier to clinical translation of SPIO nanoparticles for Imaging.

In previous work from my lab it has already been shown that MPI shows great promise in imaging vasculature [41, 36]. In addition, SPIO nanoparticles have been widely used in other biomedical applications. The size (1-100 nm) of SPIOs makes them an attractive candidate for use in both therapeutics and targeted drug delivery. Magnetic hyperthermia with SPIO nanoparticles is being widely researched for non-invasive treatment of tumors [42, 43, 44]. Also, since SPIOs are readily taken up by a wide variety of cells, they have been used in both immune cell tracking with MRI [45] and stem cell tracking with MPI [33, 34]. Use of SPIOs has also gained traction in non-targeted cancer imaging in MRI, due to the fact that nanoparticles exhibit an enhanced permeability and retention (EPR) effect [46], which increases their tendency to accumulate in tumor tissue over normal tissue. Lastly, drug delivery systems that rely on nanometer and micron sized delivery mechanism (e.g., liposomal, nebulized) have also taken advantage of using SPIOs for tracking in MRI [47, 48, 49]. Such a myriad of applications requires tailoring and optimizing of the nanoparticles. In assessing these tailored nanoparticles, it is important that we not only measure the short-term distribution of the particles, but also the long-term clearance out of the body. Excessively long clearance time could be a safety concern and also limit the ability to do consecutive imaging studies.

In this work we demonstrated that MPI is able to quantitatively asses short-term biodistribution, as well as able to do long-term tracking and clearance of SPIO nanoparticles *in vivo*.

Chapter 3

Saline Angiography: Development and Evaluation of RF Shielding for Coronary Catheter

We proposed in the introduction that saline angiography relies on an RF shielded layer for generating contrast between saline and the background tissue. It has been shown in the literature [50, 51] that in order to avoid significant heating, it is necessary to avoid continuous copper lengths that are on the order of $\lambda/2$ (13.2 cm inside the body at operational frequencies of clinical MRI scanners). Here we will show two things. First, we will show that we are able to shield out RF pulses with a thin conductive layer, and second, that introducing gaps in the conductive layer, will not compromise the copper layer's ability to shield out RF pulses.

3.1 Shielding Theory

As discussed before, MR scanners rely on high frequency magnetic field (called B_1 field) to transmit RF pulses that ultimately generate signal from ^{1}H atoms within the body. Most clinical scanners operate at radio frequencies of either 64 MHz (1.5 Tesla) or 128 MHz (3.0 Tesla). Shielding the saline from the RF pulses should significantly increase the contrast between the saline within the catheter and the tissues outside the shielded catheter.

According to EM theory a time varying magnetic field inside a conductor will decrease exponentially from its value at the surface (B_s) according to

$$B = B_s e^{-d/\delta} \tag{3.1}$$

where δ is the material specific skin depth in meters, and d is distance from the surface of the conductor, also in meters. The skin depth is given by

$$\delta = \frac{1}{\sqrt{\pi f \mu \sigma}} \tag{3.2}$$

with σ being the conductivity of the conductor, f being the frequency of the magnetic field, and μ being the absolute magnetic permeability of the material. For example, copper at f = 128 MHz has a skin depth of 6 μm. This means that a thin copper layer of about 30 μm around the catheter will attenuate the magnetic field to less than 0.7% (-45 dB).

Conceptually, an incident field, $\mathbf{B_1}(\mathbf{t})$, sets up an eddy current $\mathbf{I}_{\text{eddy}}$ in the copper shielding (Faraday's Law), that in turn set's up a counter field $\mathbf{B}_{\text{eddy}}(\text{t})$ in opposite direction (Ampere's Law). If the copper is thick enough (approximately 5δ thick), the opposing field will almost perfectly cancel out the incident field.

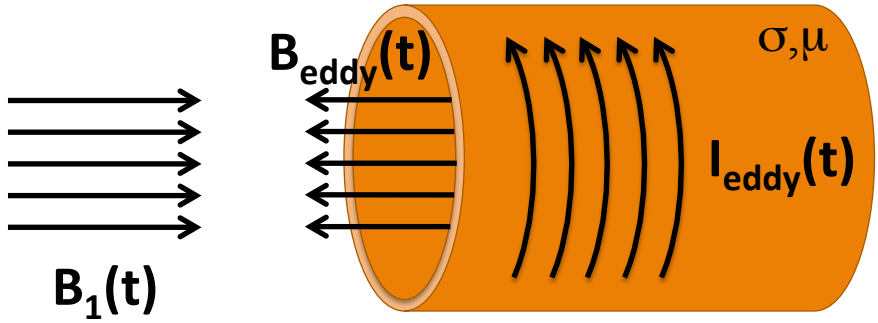

Figure 3.1: Diagram depicting a conceptual model of shielding. An incident field, $\mathbf{B_1}(\mathbf{t})$ set's up an eddy current $\mathbf{I}_{\text{eddy}}$ in the copper shielding, that in turn set's up a counter field $\mathbf{B}_{\text{eddy}}(\text{t})$ in opposite direction.

Segmenting the copper shielding should not significantly affect the shielding, as long as the gaps between the copper links are small. The shielding efficiency (SE_{db}) of an EM wave through a slit is given by [52]

$$SE_{dB} = 20\ log_{10}\left(\frac{\lambda}{2L}\right) \tag{3.3}$$

where λ is our wavelength (26.4 cm at 128 MHz), and L is the slit width. For a 1 mm slit, the shielding efficiency is about 42 dB, which is about the same as our 5δ copper shielding.

3.2 Shielding Simulations

Since we wanted to avoid a continuous shielding layer, we considered two different shielding designs. Both designs, are illustrated in Figure 3.2. In the first design, the copper links were made to overlap, with a thin insulating layer in between to prevent electrical conduction. In the second design, the copper links were made to have small insulating gaps.

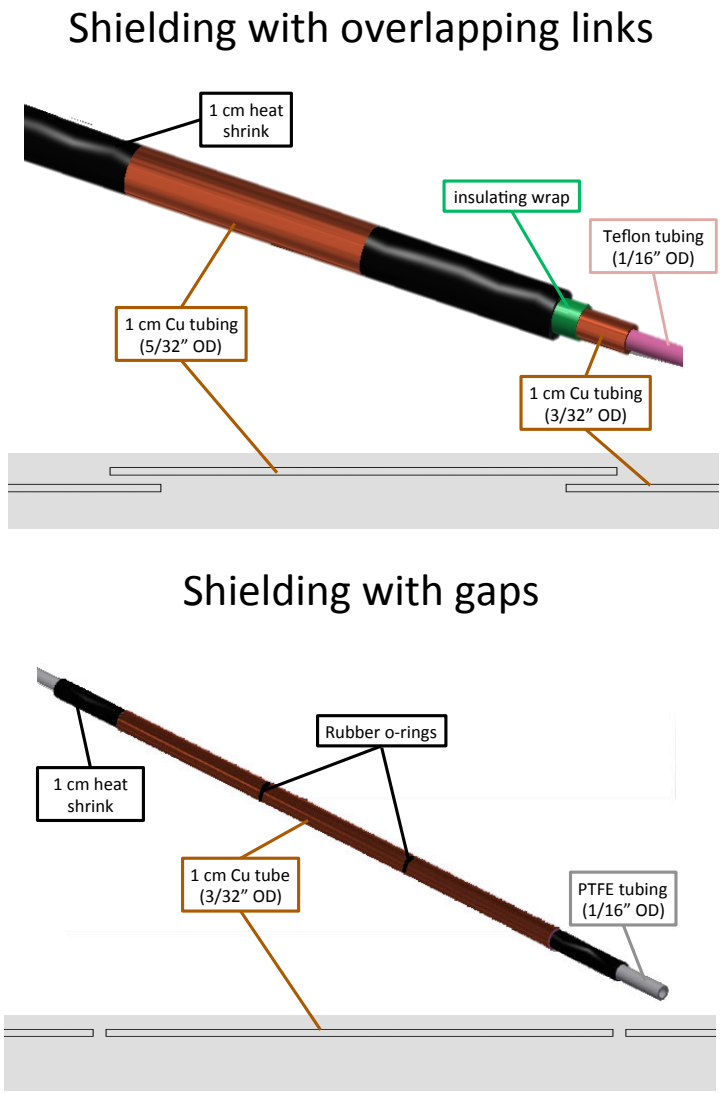

Figure 3.2: The top diagram is depicting a shielding scheme with overlapping links. An insulating layer prevents electrical contact between adjacent links. The bottom diagram is depicting a shielding scheme with insulating gaps between adjacent links. The gaps can be air or any other insulating material.

To evaluate the shielding efficiency of each design, a simulation was performed using the same simulation test bed described above. In both cases air was used as insulating material between each copper link. For the design with gaps, three 2 cm long (OD: 3/32 in) copper links were separated with a 1 mm gap. For the design with overlapping links, another two 2 cm long (OD: 5/32 in) copper links were positioned over the two gaps created by the 3 links, again with a 1 mm gap in between. The cross section of the geometry, along with the

results are shown in Figure 3.3. The graphs show the magnetic field penetration into the shielded catheter for both designs. It is clear that both designs are quite effective. For the design with overlapping links, simulation show over 100 dB suppression of the field inside the catheter. For the design with 1 mm gaps between the links, simulations show over 40 dB suppression of the field inside the catheter.

In practice the overlapping links design was too rigid to navigate the arterial tree, so was abandoned in favor of the more flexible design with insulating gaps.

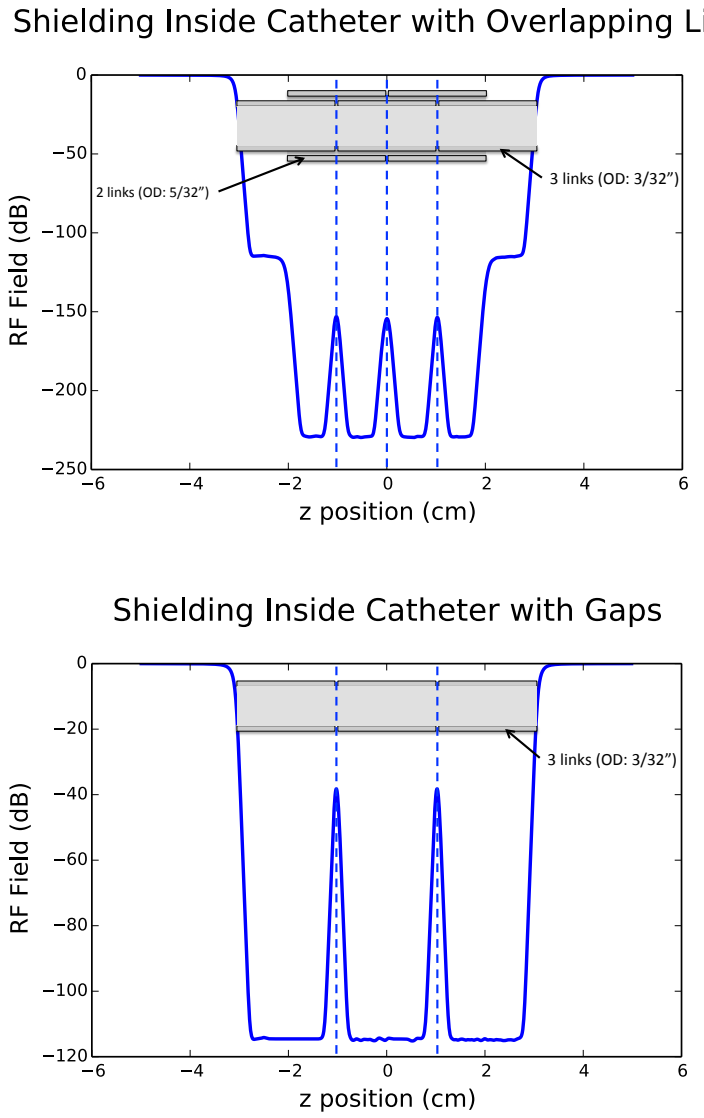

Figure 3.3: The figure on the top is simulated field versus z-position (position along the length of the catheter) of a 6 cm segment of the shielding scheme with overlapping links. There is over 100 dB suppression of the magnetic field inside the catheter. The figure on the bottom is simulated field versus z-position of a 6 cm segment of the shielding scheme with 1 mm gaps. There is over 40 dB suppression of the magnetic field even with the gaps between the copper links.

3.3 Experimental Shielding Measurements

To confirm simulation results and demonstrate the efficacy of the RF shield, we built a 2% agarose / 98% water phantom containing a small section of the shielded catheter (shown in Figure 3.4). The catheter was made from 1/16 in PTFE (Teflon^{TM}) tubing filled with the same solution as the phantom and then sealed at both ends with clay. Copper links, 3/16 in OD and separated by 1 mm rubber o-rings were used for shielding. The phantom was then imaged with a standard multislice 2D FLASH proton density weighted sequence [53], with TR of 637 ms, TE of 5.4 ms, flip angle of 40 degrees and 2 averages. Figure 3.4 contains axial image slices and intensity profiles through the center of the catheter for different location along the length of the catheter. The first slice, slice A, is through the section of the catheter that is not shielded. One can see both the phantom material outside and inside the catheter. The drops in intensity are in the wall of the plastic tubing of the catheter, but the signal remains high in the center that contains the phantom material. The second slice, slice B, is through the shielded portion of the phantom, taken right through the center of one of the copper links. As expected, the signal inside the shield is reduced down to the noise-floor. Finally, the third slice, slice C, is through the 1 mm thick o-ring separating two 1 cm segments of shielding. The signal in the center is still reduced to the noise-floor.

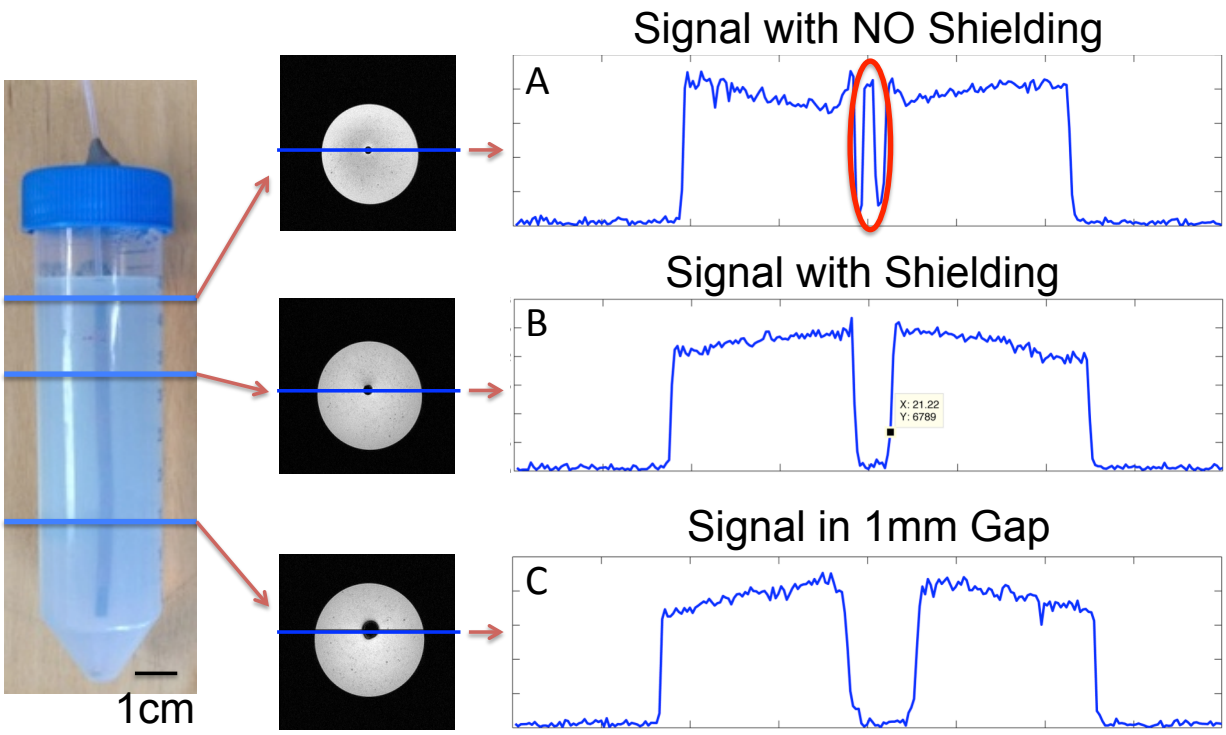

Figure 3.4: Diagram depicting RF penetration measurements in three different regions of the phantom. (A) is an image slice taken through the unshielded section of the catheter. The signal inside the catheter remains high. (B) is an image slice through the center of one of the copper links. The signal inside the catheter is reduced down to the noise floor. (C) is an image slice through the rubber o-ring separating the two copper links. Again, the signal inside the catheter is reduced down to the noise floor. The gaps between the copper links do not compromise the shielding ability of the catheter.

3.4 Conclusions

We showed that a thin, flexible copper layer can shield the inside of the catheter from RF-pulses, and also demonstrated that segmenting the shield to prevent heating does not affect its overall shielding ability. This was corroborated both with quasi-static calculations and COMSOL FEM simulations.

Chapter 4

Saline Angiography: Evaluation of Heating and Safety

We showed in the previous chapter that a thin metallic (in our case copper) layer will shield saline inside the catheter from the MR excitation pulses. In this chapter we will demonstrate that there should be no added safety concerns resulting from the added copper layer.

Copper coated with non-reactive material, such as silicone or polyurethane, is biocompatible inside the human body and non-reactive within the high magnetic field of the MR environment. However, in all MRI scans the RF field causes currents to flow through the tissue (a lossy dielectric) that in turn results in Joule heating. This mechanism has been well studied and understood. In the US, the Food and Drug Administration sets Specific Absorption Rate (SAR) guidelines for maximal amount of heating that can be deposited into human tissue. Table 4.1 is a table of SAR limits and corresponding temperature rise [54, 55].

Modern MRI scanners automatically monitor pulse sequences to operate within safe limits. However, the thin metallic layer on our RF-catheter could interact with the induced RF electric field and perhaps concentrate the current, creating dangerous hot spots in the body. It is known, for example, that there is substantial RF heating near the tips of a copper wire in the body [50, 51, 56]. This current crowding can be quite substantial when the conductor length is on the order of a half-wavelength ($\lambda/2$) [50, 51, 56]. Park *et al.* reported heating of as much as 30 °C for certain lengths of bare copper leads. Conceptually, metal objects act as low impedance resonant pathways in the tissue current loops [54] causing J-crowding at the tips. The conductor-body becomes a distributed transmission line circuit. The impedance of this circuit is a function of length, with the current path through the conductor becoming favorable at resonant length, $\lambda/2$ [56]. Figure 4.6A shows calculated voltage at the tips of a continuous copper catheter predicted by this model. The high heating at the ends of conductors of length $\lambda/2$ can be alleviated by adding an insulating layer over the conductor [57]. This slight raises the overall impedance of the conductor-body circuit, thus reducing the current density. Additionally, this also slightly affects the resonant length

FDA Limits for Whole Body Heating		
Mode	SAR (W/kg)	Temperature rise (°C)
Normal mode limit	2	0.5
First level (medical supervision)	4	1
Second level (IRB approval)	> 4	> 1
FDA Limits for Localized Heating (in a 10g mass)		
Mode	SAR (W/kg)	Temperature rise (°C)
Head (normal level)	3.2	1
Torso (normal level)	10	1.5
Extremities (normal level)	10	2
Head (first level)	3.2	1
Torso (first level)	20	3
Extremities (first level)	20	4

Table 4.1: Table of FDA set SAR limits and corresponding temperature rises.

[57]. This situation is in contrast to the regular heating in MRI where current loops are more or less uniform in the tissue and tend to cancel in the middle and add at the edges ($J \propto R$). Both models are shown in Figure 4.1.

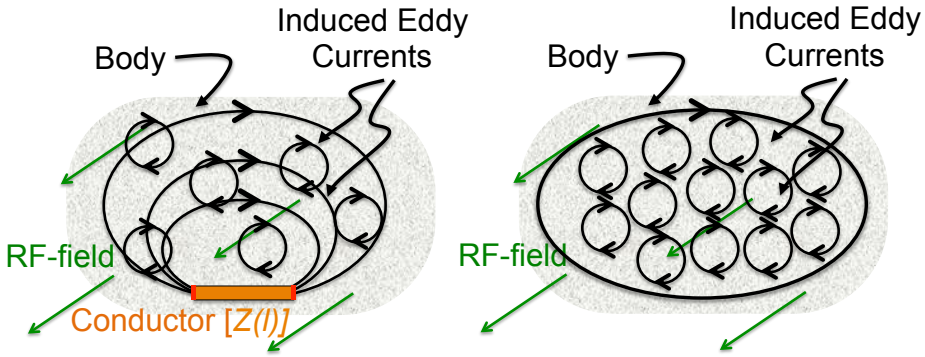

Figure 4.1: Conceptual model of metal objects acting as low impedance resonant pathways in the tissue current loops [54] causing J-crowding at the tips. The impedance of the conductor is a function of length. The current path through the conductor becomes favorable at resonant length, $\lambda/2$. This model with a conductor is in contrast to the regular heating in MRI where current loops are more or less uniform in the tissue and tend to cancel in the middle and add at the edges ($J \propto R$).

Our approach to verifying these results as well as the possible safety issues associated with our own design was to first simulate my catheter in a Finite Element Modeling software and then verify the results in a typical clinical scanner. All heating simulations were done

in COMSOL Multiphysics v4.2 software package and all experiments were carried out on a 3 Tesla Siemens scanner at UC-Berkeley's Brain Imaging Center.

4.1 Conventional SAR in MRI

To first order, without any metallic objects present, the SAR due to a uniform RF field, can be estimated using a simplified cylindrical model, where the body is modeled as an infinite cylinder of radius r (see diagram in Figure 4.2). We assume a quasi-static field approximation. This allows us to decouple $\mathbf{B}$ and $\mathbf{E}$ fields since at our frequency, ω and length scale, L,

$$\omega L \ll \frac{1}{\sqrt{\mu\epsilon}} \tag{4.1}$$

where in the human body $\mu \approx 1$ and $\epsilon \approx \epsilon_{r,H_2O}\epsilon_0$.

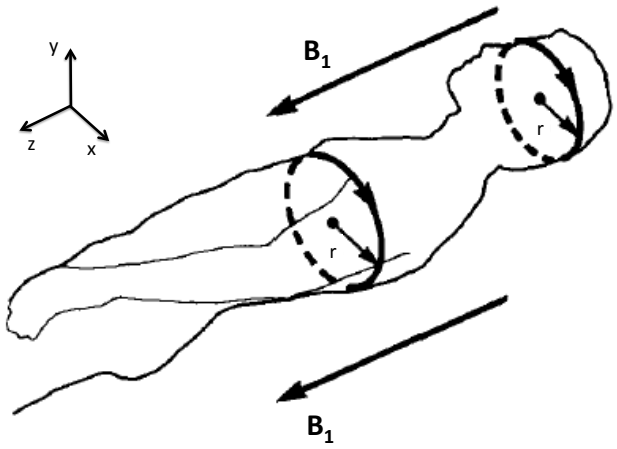

Figure 4.2: Simplified cylinder model for estimating conventional SAR.

With these assumptions the electric field induced can be estimated by a quasi-static approximation using Faradays Law.

$$\nabla \times \mathbf{E} = -\frac{\partial \mathbf{B}}{\partial t} \tag{4.2}$$

where $\mathbf{E}$ is the electric field, and $\mathbf{B}$ is the magnetic field.

Given a sinusoidally varying magnetic field along the z direction, Equation 4.2 gives

$$E_\phi = \pi f B_1 r \tag{4.3}$$

From the electric field, we can approximate the conventional SAR density, which is defined as the total RMS power absorbed per unit mass of tissue and is measured in watts per kilogram. This can be expressed in terms of the electric field as follow [58, 50]

$$SAR = \frac{|E|^2\sigma}{2\rho} \tag{4.4}$$

where σ is the conductivity of the dielectric media, and ρ is the mass density.

Putting everything together, we get the following relation

$$SAR \propto \sigma\rho^{-1}f^2B_1^2r^2 \tag{4.5}$$

The RF field is not on continuously, but is pulsed as data is acquired. To account for that, we can introduce a duty cycle factor D = $\frac{\tau}{T_R}$,where τ is the total time the RF pulse is on and T_R is the repetition time between each Pulse. So that average SAR, or SAR per unit time, is

$$\overline{SAR} \propto \sigma\rho^{-1}f^2B_1^2r^2D \tag{4.6}$$

4.2 SAR and Heating in the presence of a metallic object

A metallic object alters the Electric field, and can no longer be estimated with Quasi-static approximation used above. Hence, we decided to rely on finite element modeling (FEM) software package. COMSOL Multiphysics v4.2 was chosen because it allows for coupling of different physics in one simulation. In this case, the Radio Frequency (RF) module was used to calculate the electric field, which was then used in the Heat Transfer module to calculate heating and the corresponding temperature rise in the catheter.

Figure 4.3 illustrates the simulation environment and Table 4.2 is a list of parameters used in the simulations. Tissue specific constants are from references [59] and [60]. The simulation contains a large spherical air volume, a 16-rung birdcage coil, a tissue phantom, and a copper catheter. Geometries were chosen to correspond to the real life environment of the MRI scanner. The thermal and electric properties of the tissue phantom were chosen to be similar to that of real tissues. Note that the dielectric properties of the tissue phantom, such as conductivity, σ and relative permittivity ϵ_r were chosen to correspond to those of tissue at a frequency of 127.74 MHz, the operating frequency of a typical 3 Tesla clinical scanner (and the scanner used to collect heating measurements).

Electric field, **E**, was modeled in the Radio Frequency module, Frequency Domain form, which assumed that the resultant fields were wave-like and that the power transfer occurred primarily via radiation. The field was calculated according to

$$\nabla \times \mu_r^{-1}\left(\nabla \times \mathbf{E}\right) - \omega^2\epsilon_0\mu_0\left(\epsilon_r - j\sigma/\omega\epsilon_0\right)\mathbf{E} = 0 \tag{4.7}$$

where μ_0 (SI unit: H/m) and ϵ_0 (SI unit: F/m) are permeability and permittivity of free space, μ_r and ϵ_r are relative permeability and permittivity, ω (SI unit: rad/s) is the angular frequency, and σ (SI unit: S/m) is the conductivity of the material.

Geometry Parameters			
Coil and Tissue Phantom		Catheter	
Number of rungs:	16	tube OD:	3.97 mm
Coil diameter:	60 cm	tube ID:	2.39 mm
Coil length:	70 cm	tube length:	1.26 cm
phantom (l x w x h):	38 cm x 25 cm x 8 cm	tube gap:	1 mm
Simulation Parameters			
f0:	127.74 Mhz	total time:	15 minutes
duty cycle (D):	0.3	coil voltage:	70 V
Material Properties			
Phantom (Tissue)		Catheter (Copper)	
Density (ρ)	1000 kg/m^3	Density (ρ)	8700 kg/m^3
Rel. permittivity (ϵ_r)	77	Rel. permittivity (ϵ_r)	1
Rel. permeability (μ_r)	1	Rel. permeability (μ_r)	1
Elec. Cond. (σ)	1 S/m	Elec. Cond. (σ)	6×10^7 S/m
Therm. Cond. (k)	0.6 W/(m K)	Therm. Cond. (k)	400 W/(m K)
Heat Capacity (C_p)	4000 J/(kg K)	Heat Capacity (C_p)	385 J/(kg K)
Simulation Region (Air)			
Elec. Cond. (σ)	0 S/m		
Rel. permittivity (ϵ_r)	1		
Rel. permeability (μ_r)	1		

Table 4.2: Table of simulation parameters.

Once the resultant field was calculate, it was fed into the Heat Transfer module (Time Domain form) which assumed a purely conductive heat transfer according to

$$\rho C_p \frac{\partial T}{\partial t} + \nabla \cdot (-k \nabla T) = Q \tag{4.8}$$

where ρ is the material density (SI unit: kg/m^3), C_p is the specific heat capacity (SI unit: J/(kg K)), k is the thermal conductivity (SI unit: W/(m K)), T is absolute temperature (SI unit: K), and Q are the heat sources (SI unit: W/m^3). All heating simulations were run over a 15 minute period as per [54].

The first step in setting up the simulation was to calibrate the operating voltage on the simulated birdcage coil to produce the correct magnetic field. In MRI, the magnitude and duration of RF pulses are chosen to correspond to the amount of rotation the net magnetization experiences. Given the flip angle, θ, and RF pulse duration, τ, one can calculate the magnitude of the magnetic field from rearranging equation (2.2)

$$B_1 = \frac{\theta}{\gamma \int_0^\tau S(t)\, dt} \tag{4.9}$$

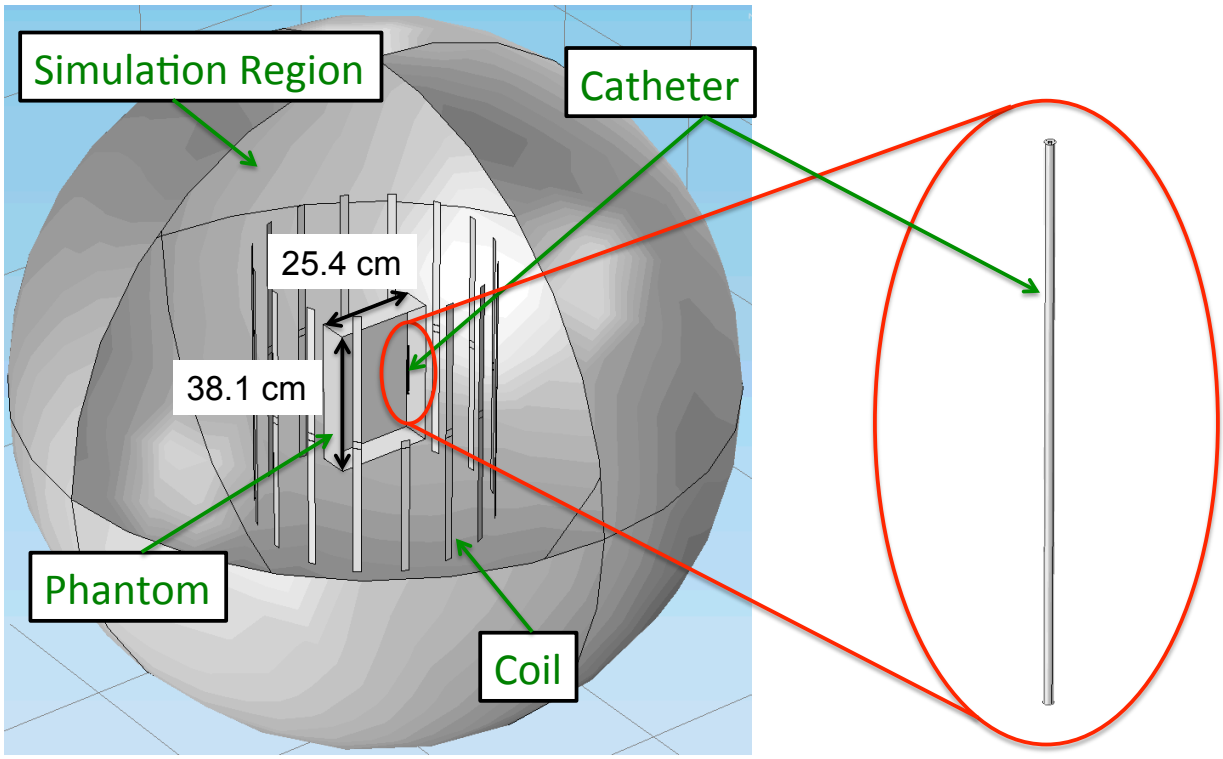

Figure 4.3: Illustration depicting COMSOL simulation region, birdcage coil, test phantom, and catheter.

where γ is the gyromagnetic ratio of ^{1}H nuclei with a value of 2.67513×10^8 rad/(s T), and S(t) is a term describing the normalized shape of a sequence specific pulse. On the 3 Tesla system at UC-Berkeley a typical B_1 is about 2 μT to 3 μT. Since magnetic fields are additive, the phantom and the catheter were removed from the simulation to get an accurate value of the field. The voltage was then adjusted to produce a field of about 2.5 μT (See Figure 4.4). The magnetic field is fairly uniform within the imaging volume, with small hyperintensities only occurring close to the rungs of the coil. The direction of the magnetic field will rotate at 127.74 MHz around the center of the coil. On the other hand the electric field increases radially outward, starting with $E = 0$ V/m at the center of the coil.

The next step was to introduce a rectangular tissue phantom into the simulation. To connect the RF Physics to the Heat Transfer physics, the entire phantom domain was set as a Heat Source, Q (W/m^3), with the value set using the Joule (resistive) Heating equation

$$Q = \sigma E^2 \tag{4.10}$$

where E is the Electric Field calculated by the RF Physics module. Results of the heating simulation are illustrated in Figure 4.5. The simulation showed a dependence on the size of the phantom with most heating occurring at the radial edges. This agrees with the results

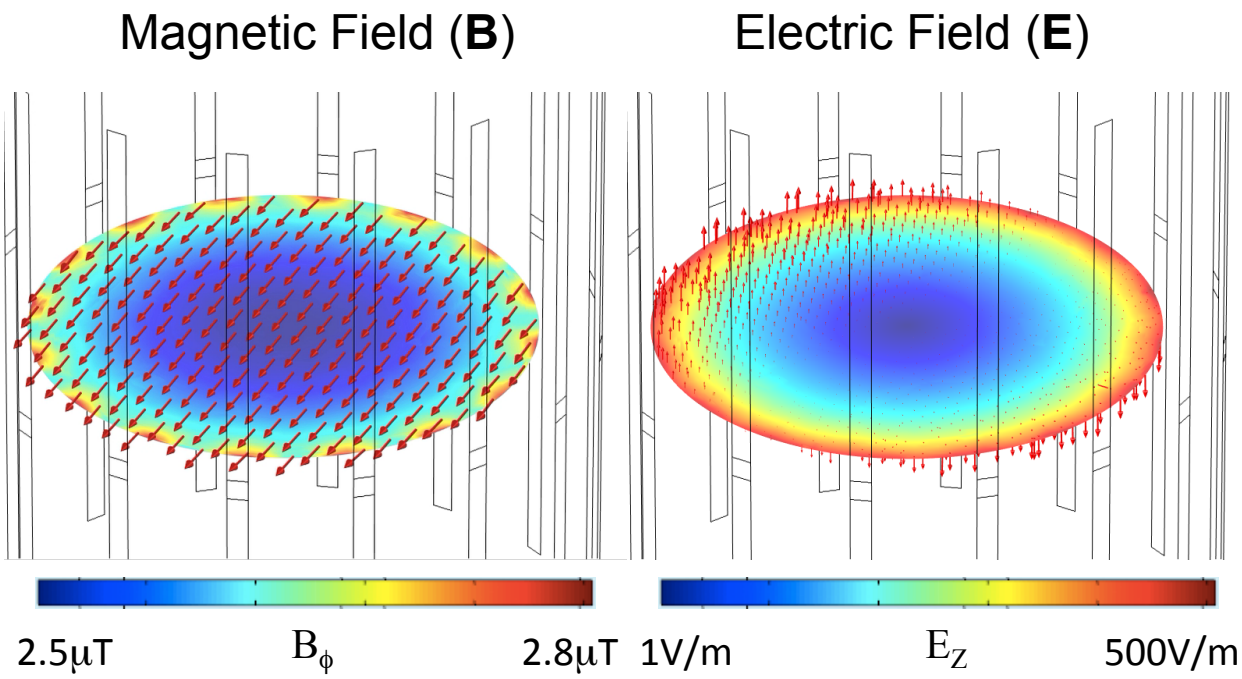

Figure 4.4: Illustration depicting simulated magnetic and electric field magnitude and direction inside a typical quadrature coil. The magnetic field is uniform and rotates circularly around the z-axis. On the other hand, the Electric field agrees with the quasi-static approximation of Equation 4.3, with 0 V/m at the center and increasing outward with the radius.

from Equation 4.6 as well as the fact that the Electric field increases radially from the center of the coil.

The final step was to introduce the copper catheter into the simulation. As mentioned earlier, heating in a metallic object increases significantly at half-wavelength lengths. The wavelength of an electromagnetic standing wave in any dielectric media is given by

$$\lambda = \frac{1}{\omega\sqrt{\mu_r \mu_0 \epsilon_r \epsilon_0}} \tag{4.11}$$

where $\mu_0 = 4\pi \times 10^{-7}$ H/m, $\epsilon_0 = 8.854 \times 10^{-12}$ F/m. For the purposes of the simulation we assumed that the values of relative permeability and relative permittivity were that of water at 20 °C and set to 1 and 77 respectively. Plugging all the numbers into Equation (4.11) we get $\lambda = 26.4$ cm, which is on the order of magnitude relevant to our design. Running the simulation show a significant dependence of heating to the catheter length. In fact, simulations predict dangerous heating of tissue at the tips of the catheter whose lengths are around $\lambda/2$. Figure 4.6 shows heating in °C versus catheter length. The temperature rises steadily to 11.4 °C at $l = \lambda/2 = 13.2$ cm and then drops again. As expected, most heating

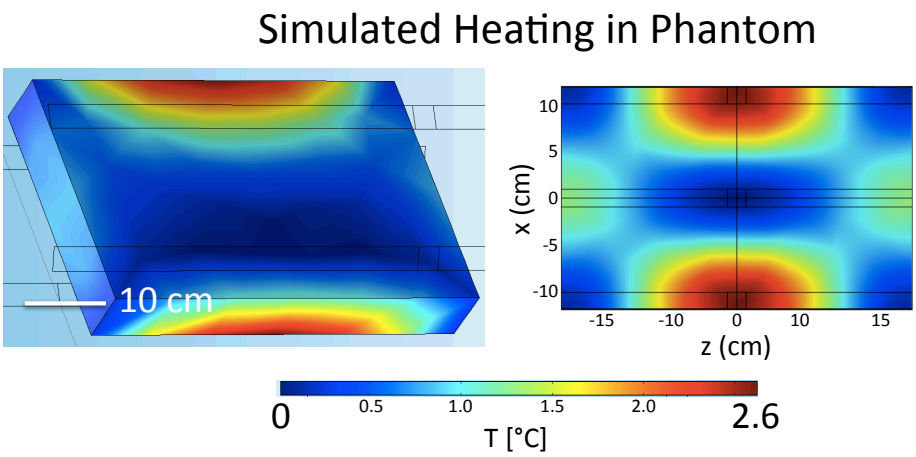

Figure 4.5: Illustration depicting COMSOL simulation depicting heating of a rectangular phantom. Image on the left is a 3D rendering of the phantom, and image on the right is a slice through the middle of the phantom. Simulation predict heating of about 2.6 °C at the edge of the phantom.

of tissue occurred at the tips of a catheter with a length equal to the half-wavelength of an electromagnetic wave in water.

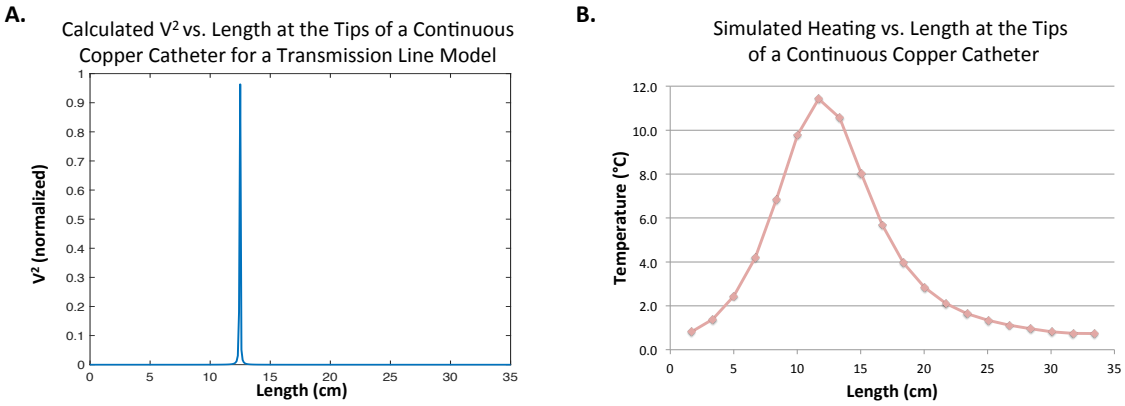

Figure 4.6: (A) Calculated square of the voltage at the tips of a continuous copper catheter for a transmission line model [56]. (B) Simulation of maximum heating of tissue at the tips of a continuous copper catheter vs. it's length. Simulations are in agreement with a transmission line model and show dangerous heating of tissue at the tips of the catheter whose lengths are around $l = 13.2$ cm which is the half-wavelength of an electromagnetic wave in water.

As mentioned before, it appears that the catheter is acting as a preferential, low-impedance

path for current loops enabling significant heating at the copper edges (See Figure 4.1).

To counteract the resonant heating we devised a strategy of cutting the continuous copper catheter into segments much shorter than $\lambda/2$ length. In the simulations, the catheter links were made to be about 1 cm long with a gap between the links of about 1 mm. Figure 4.7 shows simulated electric field, and Figure 4.8 shows simulated heating for a segmented vs. continuous catheter of length $l = \lambda/2$. While the continuous catheter showed significant heating, the segmented counter-part showed much less heating and in fact stayed below the FDA heating limit of 3 $^{\circ}C$. It is crucial to note that the copper catheter in these experiments remains cool; it is the tissue adjacent to the tips that heats up.

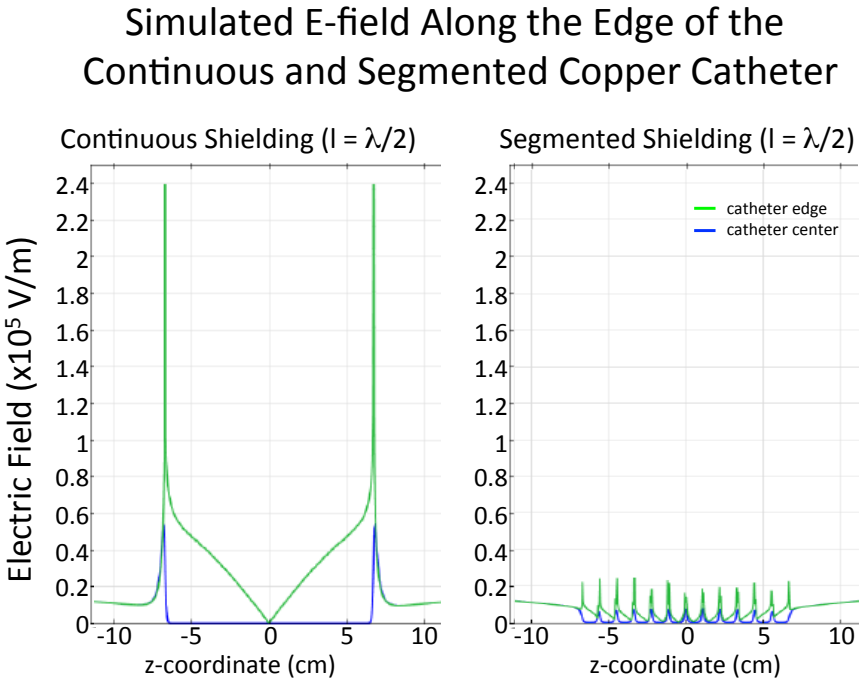

Figure 4.7: Illustration depicting COMSOL simulation of the electric field of segmented vs. continuous catheter of length 13.2 cm (half-wavelength). Simulation shows much higher electric field on the edges of the continuous copper catheter compared to the edges and center of the segmented copper catheter.

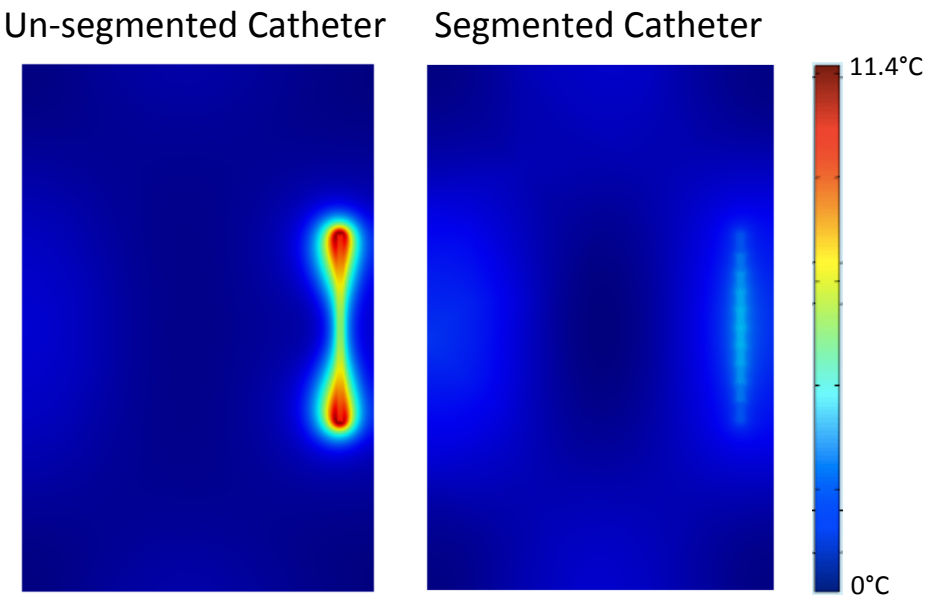

Figure 4.8: Illustration depicting COMSOL simulation of heating of segmented vs. continuous catheter of length 13.2 cm (half-wavelength). Simulation show dangerous heating for the continuous catheter, while the segmented catheter stays under the safety limit.

4.3 Experimental Heating Measurements

According to FDA guidelines for Implanted Medical Devices, an implant should not heat more than 3 $^{\circ}C$ over a 15-minute period when exposed to a high heat-deposition sequence [54]. Following the experimental guidelines set by the FDA we constructed a phantom mimicking electrical and thermal properties of human tissue. Both thermal and electrical properties depend primarily on the conductivity, σ. Conductivity in water changes with concentration of sodium chloride, NaCl, according to [61]

$$\sigma = 10.3 \text{ (S/m)} \text{ [NaCl]/(mol/L)} + 0.0082 \text{ (S/m)} \tag{4.12}$$

Table 4.3 is a list of average conductivities in human organs.

Tissue	σ (S/m)
blood	1.25
fat	0.037
muscle	0.72
heart	0.77

Table 4.3: Table of tissue conductivities at 127.74 MHz [59].

A conductivity of 1 S/m was chosen as the concentration of the tissue phantom. Also, in order to reduce convective cooling, the phantom was gelled with agarose to an approximate concentration 0.25% by mass. At this concentration of agarose, the gel remained fairly liquid to allow for insertion of copper tubes and temperature probes. Following the preparation of the phantom, the conductivity was independently verified with a conductivity meter (Model: UX-19601-03, Cole Parmer).

The heating experiments were done in a plastic tub, 38 cm x 25 cm x 8 cm (approximately 15 in x 10 in x 3 in) in size.

Reproducing the sequence of tests in the simulations, the phantom was then positioned in the iso-center of the MRI scanner with the long axis parallel to the bore of the scanner. It was then imaged with a standard body coil using a sequence set at First Level as defined by FDA safety limits in Table 4.1. The imaging sequence was a Balanced Steady State Free Precession sequence (trueFISP) with FOV of 30 cm x 30 cm oriented parallel to the coronal plane (corresponding to the 38 cm x 25 cm plane of the phantom), TR of 4.26 ms, TE of 2.13 ms, a duty cycle of 0.3 and flip angle of 59° (highest allowed by the system). A series of 15 minutes temperature measurements were made at 16 uniformly positioned spots in the rectangular phantom. These measurements were made with a 4-probe optical-fiber temperature system (Reflex^{TM}from Neoptix Inc.). The results were then interpolated and plotted in MATLAB (The MathWorks, Inc.). The temperature map is shown in Figure 4.9. The measurements show a maximum temperature rise of about $3°C$, with highest recorded temperature measured at the edges parallel to the scanner bore. Both the magnitude and the temperature distribution agree quite closely with simulated results shown in Figure 4.5. Even without any metallic devices any conductive tissue will heat in the MR environment.

The next step was to introduce the copper catheter into the tissue phantom. Thin walled copper tube (K&S Engineering) with OD = 1/8 in (3.175 mm) and wall thickness of 0.014 in (0.036 mm) was chosen for this experiments. As in simulations, several different lengths and two different catheter geometries (continuous vs. segmented) were tested. Figure 4.10 shows the continuous and segmented catheter used in the heating tests. Different length catheters were prepared and tested for each geometry. Four temperature probes were used to measure temperature rise adjacent to the copper catheter and the tissue gel itself. The first probe was placed at the tip of the catheter, the second was placed 1 cm from the tip towards the center of the catheter, the third was placed at the center of the catheter and the fourth was placed in the center of the tissue phantom. Figure 4.11 shows the heating curves over a 15 minute period measured by the four temperature probes.

The first series of tests were run on the continuous lengths of copper tube (Figure 4.10A) and the second series of tests were run on the same lengths of tubing which were segmented into 1 cm links, that is $< 4\%$ of 1 wavelength at 3T (Figure 4.10B). In both cases the copper tubes were slid over an OD: 1/16 in polytetrafluoroethylene (PTFE) tubing (McMaster Carr Inc.). In the segmented case, the 1 cm links were separated by 1mm Buna-N rubber o-rings (McMaster Carr Inc.).

The same RF pulse sequence that was used in the tissue phantom experiment described above, was used to test the heating of the copper catheter as well. Figure 4.11 shows a heating

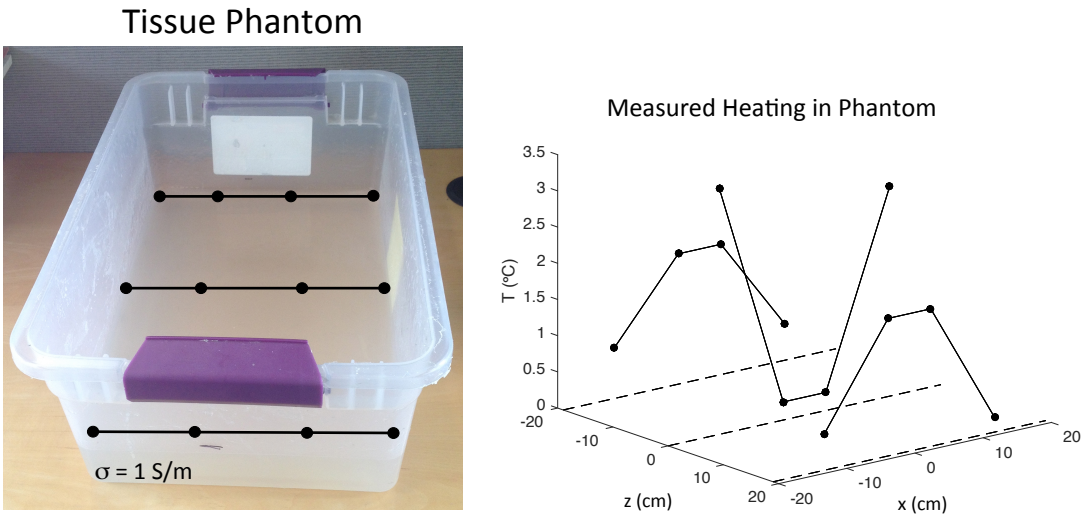

Figure 4.9: Figure on the left is a photograph of the rectangular tissue phantom ($\sigma = 1$ S/m) of dimension 38 cm x 25 cm x 8 cm. On the right is a corresponding temperature measurement after the phantom was subjected to a high SAR imaging sequence for 15 minutes. The measured results show higher heating at the edges versus the center and corners, which agree with simulated results shown in Figure 4.5.

curve over a 15-minute period for one of the continuous copper tubes ($l = \lambda/2 = 13.2$ cm). The shape of the curve is consistent to one predicted by Newton's Law of Heating (and Cooling)

$$\dot{Q} = mC_p\dot{T} = hA\Delta T \tag{4.13}$$

where Q is the thermal energy in J, m is the mass in kg, C_p is the specific heat in J/(kg K), h is the heat transfer coefficient in W/(m^2 K), A is the heat transfer surface area in m^2, T is the absolute temperature in K, and $\Delta T = T(t) - T_{\text{env}}$ is the thermal gradient between the object and the surrounding environment. The solution to the above equation has an exponential rise or decay form

$$T(t) = T_{env} + \Delta T e^{-\frac{hA}{mC_p}t} \tag{4.14}$$

Figure 4.12 is a plot of maximum heating for a catheter with continuous shielding and segmented shielding. As in simulations continuous shielding causes tissue heating that exceeds the FDA limits described in Table 4.1. On the other hand the catheter with segmented shielding stays within the FDA safety limits, and in fact was about the same as normal heating of the surrounding phantom.

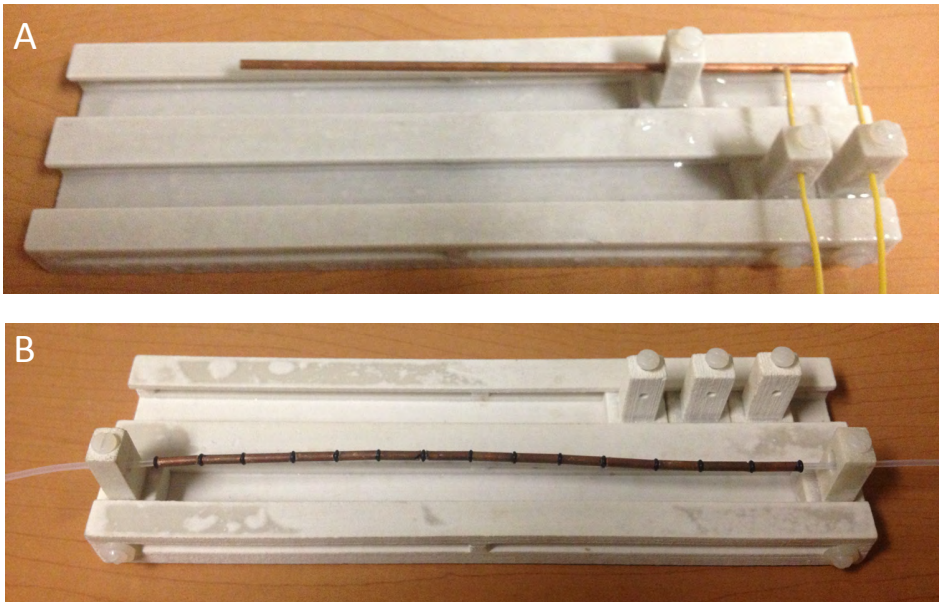

Figure 4.10: (A) shows a continuous tube in the plastic testing apparatus. The figure also shows two temperature probes to measure heating next to the tip of the tube. (B) shows a copper tube segmented into 1 cm links by 1mm Buna-N rubber o-rings.

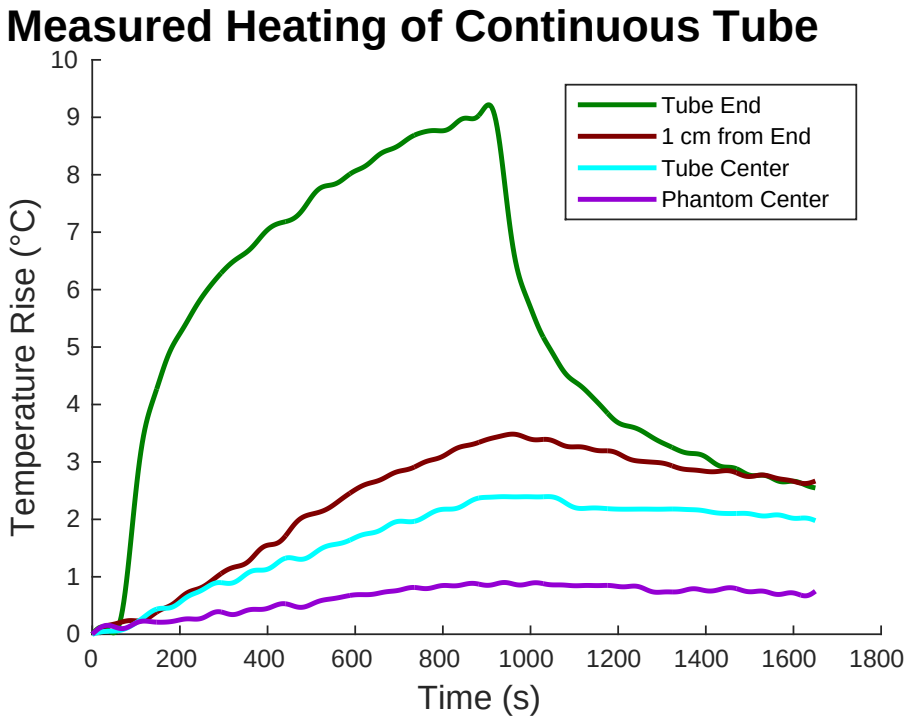

Figure 4.11: Measured heating curve over a 15 minute period for 2 probes placed near the tip of the continuous copper tube of length $l = \lambda/2 = 13.2$ cm. The temperature probe right next to the tip shows heating close to 9 °C, while the temperature probe that was placed 1cm away (along the length of the copper tube towards the center) shows significantly less heating. This is consistent with simulations shown in Figure 4.8.

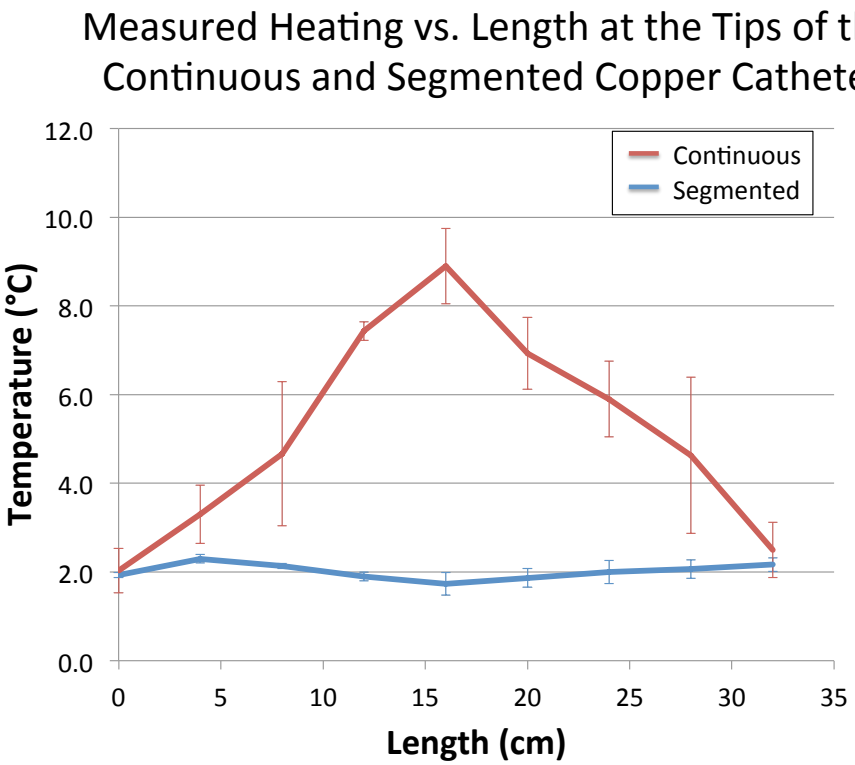

Figure 4.12: Measured maximum heating of continuous and segmented catheter versus length. As in simulations, the catheter with the continuous shielding heated far above the FDA safety limit of $3°C$, while the catheter with segmented shielding stayed within the FDA safety limits, and in fact did not heat more than the expected heating of the tissue phantom by itself.

4.4 Conclusions

These results suggest that segmenting the RF shield seems to be an effective method of keeping heating below harmful levels. Both experiment and simulations demonstrate that heating stays below the FDA set limit of 3 °C, even when the segmented catheter is exposed to a high SAR sequence. The next step was to show that the RF catheter is able to achieve clinically significant contrast.

Chapter 5

Saline Angiography: Design and Evaluation of Custom MRI Imaging Sequence

5.1 Robust Contrast in the presence of B_0 and B_1 variations and motion

Nearly all MRI pulse sequences suffer from artifacts due to B_0 and B_1 variations and motion, and are the three most devastating sources of artifacts in MRI. Some pulse sequences are particularly robust to certain of these known challenges. Here, we plan to employ adiabatic inversion pulses, which enjoy near perfect immunity to B_1 variations. We also plan to use RF pulses with adequate bandwidth to work robustly over the entire expected off-resonance field (typically about 10 ppm B_0 inhomogeneity due to air in the nearby lungs). Because all of our suppression relies on the z-component of magnetization, we do not expect significant motion artifacts in the tissue suppression. However, we plan to use a real-time imaging sequence [62], to suppress motion artifacts in the coronary artery tree. Furthermore, the saline is in the z-magnetization state, and hence, it is also robustly magnetized while in the catheter, regardless of B_0, B_1 or motion. We also plan to show that significant inflow time can be achieved by using spectral spatial pulses that avoids excitation (and thus reception) of fat in the tissue. Hence, all of the above steps produce robust suppression of the background tissue, without variations due to B_1 and B_0 inhomogeneity or variations due to motion.

Here I describe an approach that was taken to evaluate the effectiveness of imaging coronary arteries using injections of saline through a copper shielded catheter. In short, an inversion recovery preparation sequence was used to null all tissues not shielded by the RF-catheter, followed by a fast readout sequence.

The preliminary set of experiments were done in Berkeley's Brain imaging center on a 3 Tesla scanner. All sequence and pulse development were done in Berkeley's preclinical

imaging center on the 7 Tesla scanner.

5.2 Inversion Recovery Magnetization Preparation

Our proposed nulling method was to use an Inversion Recovery Magnetization Preparation (IR). Standard IR can be used to null signal from one specific tissue type to maximize contrast in the image. An inversion pulse, also called a 180° or π pulse, flips the initial longitudinal magnetization (M_0) of all tissues in the direction opposite to the main magnetic field ($\mathbf{B}_0$). The spins then undergo T_1 relaxation as they re-align back to the main field. This is known as inversion recovery. The longitudinal time-dependent signal, $M_z(t)$, is calculated from Equation 2.4 and is given by

$$M_z(t) = M_0 + (M_z(0) - M_0)e^{-t/T_1} \tag{5.1}$$

where M_0 is the equilibrium magnetization, $M_z(0)$ is the initial magnetization at $t = 0$, and T_1 is the relaxation time. Figure 5.1 illustrates magnetization in 3 types of tissues after an inversion pulse. All tissues have distinct rates of recovery, and will exhibit zero magnetization at different points in time (this time is usually called the TI time). To obtain maximum contrast, an image can be acquired when one tissue exhibits zero magnetization.

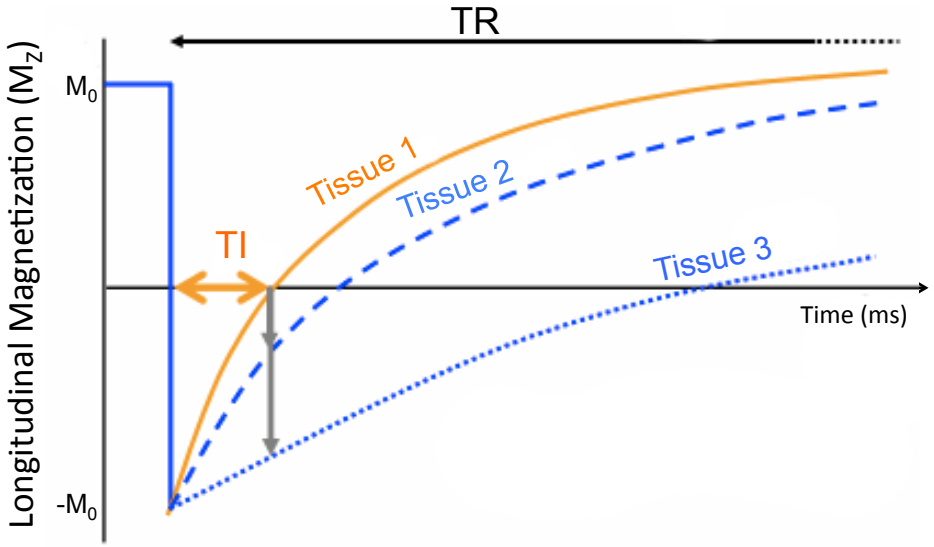

Figure 5.1: Diagram depicting inversion recovery of 3 types of tissues following an application of an inversion pulse. All three tissues are recovering exponentially towards equilibrium, M_0. If imaging occurs at t = TI post inversion, then Tissue 1 will have no signal, and Tissue 2 and 3 will have signal in a ratio corresponding to the gray arrows.

A TI for a tissue with relaxation time, T_1, is calculated by setting Equation 5.1 to 0 with $M_0 = 1$ and $M_z(0) = -1$. TI is then,

$$TI = -T_1 \ln(0.5) \tag{5.2}$$

To test the feasibility of using inversion recovery with a shielded catheter, a single tissue imaging phantom, similar to those used in the heating and shielding experiments, was created. The phantom consisted of 1/16 in OD plastic tubing embedded in a 2% Agarose / 98% water solution. One end of the tubing was shielded with 1 cm copper links separated by 1 mm rubber o-rings. Manganese chloride was added to adjust the T_1 relaxation time of the phantom to be similar to that of human tissue. The relaxation time versus manganese concentration is given by [63]

$$\frac{1}{T_1} = 0.000181\ (\text{ms}^{-1}) + 0.00743\ (\text{ms}^{-1})\ [Mn^{+2}]/(\text{mM}) \tag{5.3}$$

where T_1 is in milliseconds, and $[Mn^{+2}]$ is in milliMolar. The manganese concentration was adjusted so that the phantom material had a T_1 of about 300 ms (which would correspond to an inversion time, TI of 203 ms). Following the preparation of the solution, the gel was allowed to set over the tubing in a 15 cm diameter plastic container.

A standard non-selective inversion recovery magnetization-prepared rapid gradient-echo (IR-MPRAGE) sequence [64] with total acquisition time of 5.1 minutes, 256 x 240 matrix, 16 cm x 16 cm FOV, slice thickness of 1 cm, TR of 600 ms, flip angle of 5 degrees, TE of 3.49 ms, and TI of 203 ms was used to test the effectiveness of the copper shielding. All tests were done at the Berkeley 3T MRI system. The phantom and the corresponding maximum intensity projection image (MIP) collected with no inversion pulse is shown in Figure 5.2.

The inflow distance can be estimated from solving the Bloch Equation (Equation 2.4). Figure 5.3 shows excitation pulses from an IR-MPRAGE sequence and the corresponding M_{xy} magnetization of the freshly in-flowing saline exiting the catheter.

The graph shows a dropping signal as saline experiences more excitation pulses. This is due to the fact that the T_1 relaxation time is relatively high compared to the timing between the pulses – the signal does not have time to recover before the next excitation. If we assume that the stationary background tissue is completely nulled by the inversion pulses, then the calculations predict an inflow time of about 40 cm before the saline signal will drop below the noise floor. Figure 5.4 is a graph of the saline signal along with the corresponding contrast versus background. Where

$$\text{Contrast} = \frac{\text{Saline Signal}}{\text{Background Signal}} \tag{5.4}$$

After adjusting the inversion time to null the background phantom ($TI = 203$ ms), saline was injected, first, from the shielded side, and then from the unshielded side. Figure 5.5 is a MIP of the flow phantom described above. The image on the left is of in-flowing saline

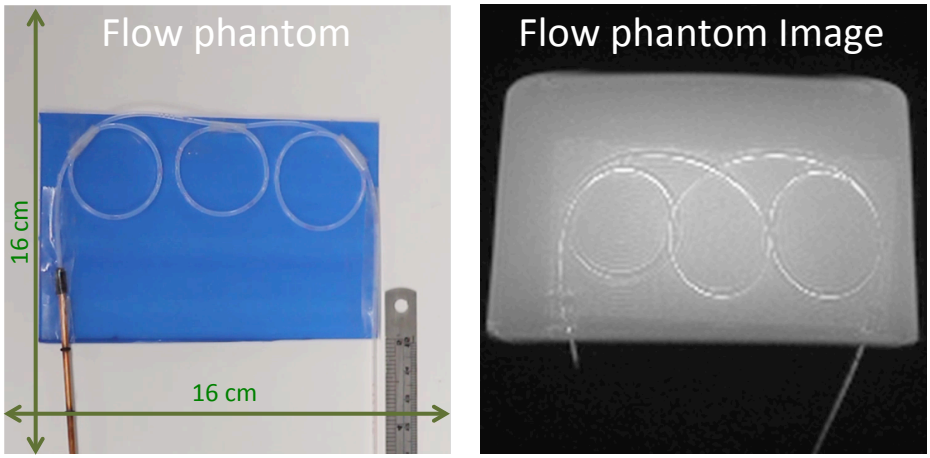

Figure 5.2: Photo of the flow phantom and the corresponding maximum intensity projection image of the 3D image acquired with the MPRAGE sequence (16 cm x 16 cm FOV and total acquisition time of 5.1 minutes). The flow phantom is embedded into a 2% Agarose/98% Water gel for imaging. Saline injected on the left side will be shielded from RF excitation pulses, while saline injected on the right side will not.

injected from the shielded side, while the image on the right is an image of in-flowing saline injected from the unshielded side.

The inflow distance and the signal drop-off agree with theoretical calculation described above. Saline injected from the shielded catheter was able to penetrate about 4 times further (about 40 cm compared to 10 cm) into the flow phantom before getting nulled.

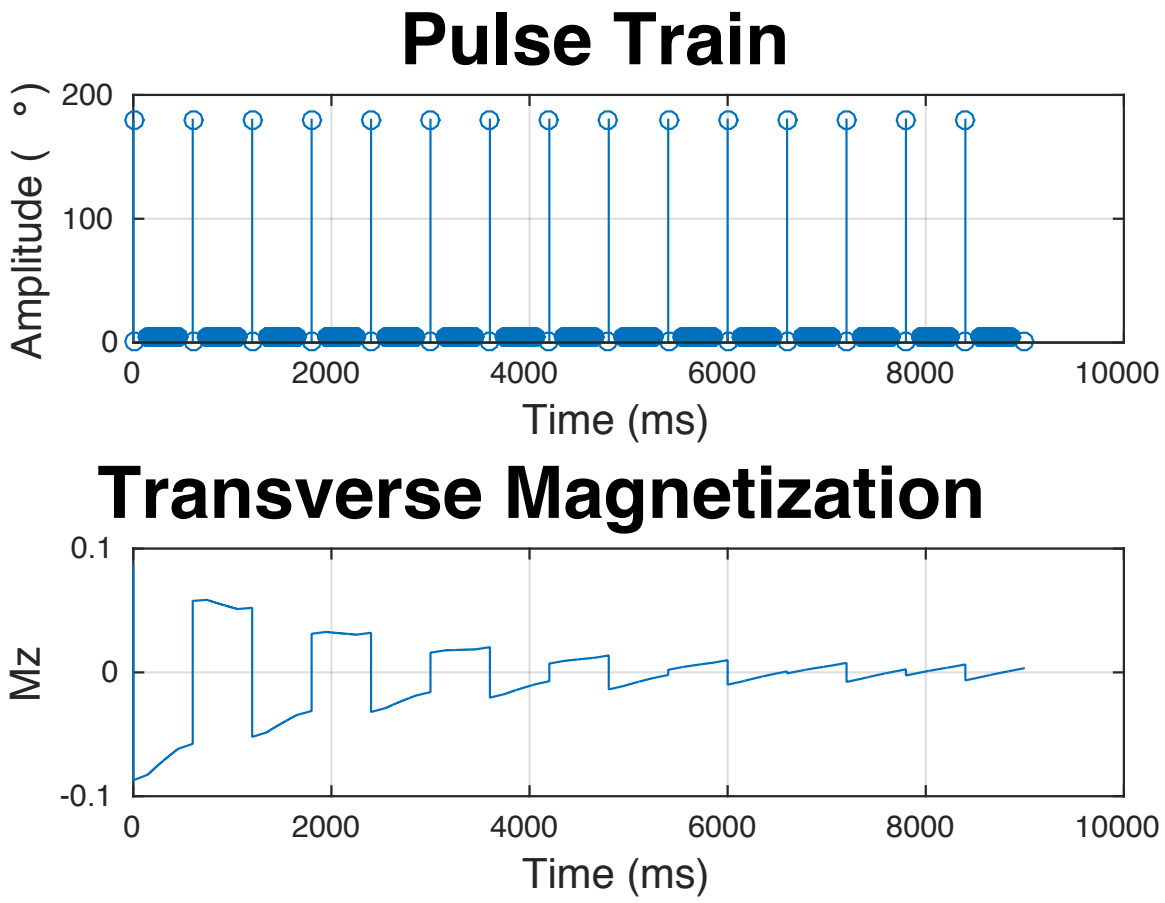

Figure 5.3: MPRAGE RF pulses and corresponding M_{xy} magnetization. The graph shows a dropping signal as saline experiences more excitation pulses. The saline will have a limited wash-in time before getting nulled by the inversion pulses.

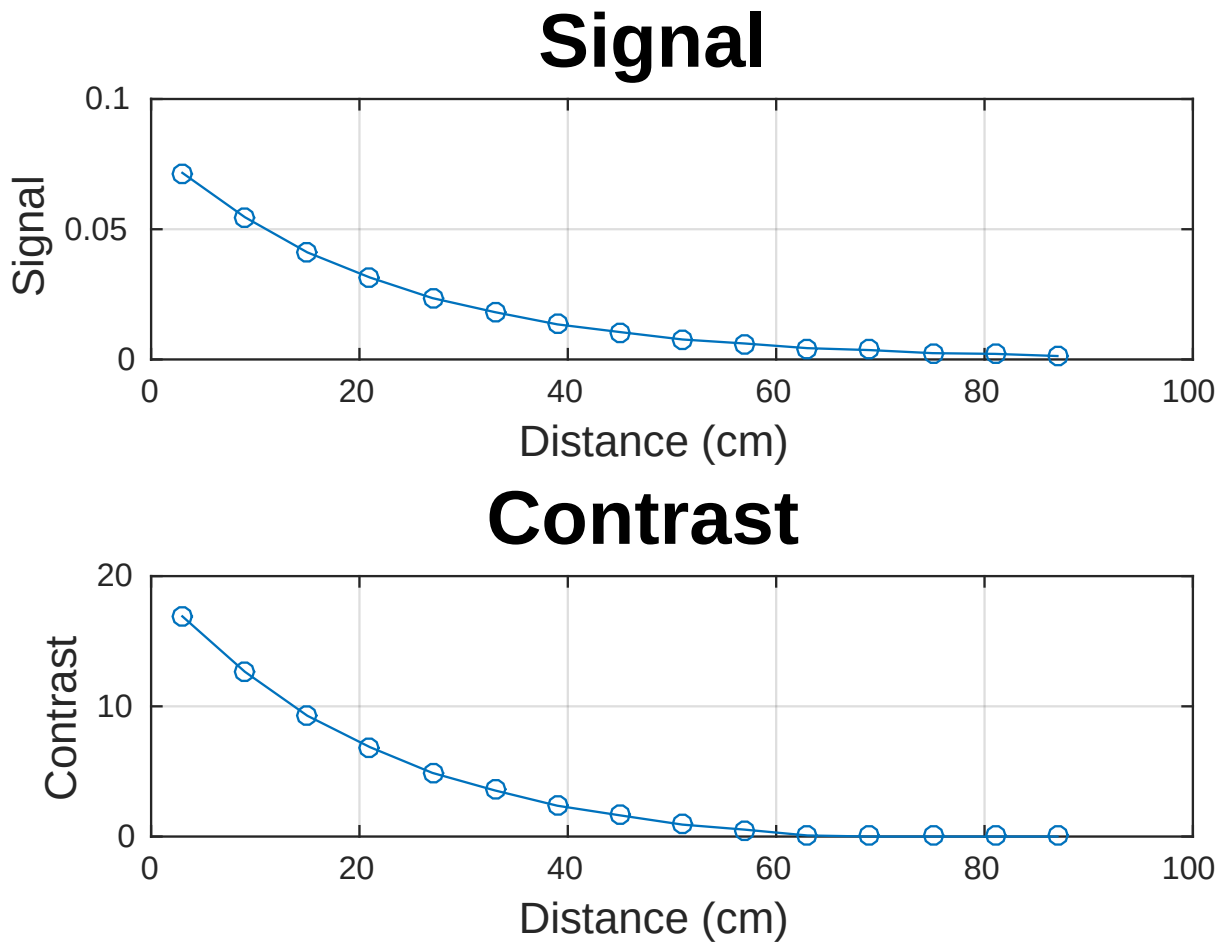

Figure 5.4: MRAGE pulses, and the simulated saline signal and corresponding contrast for an inversion recovery MPRAGE sequence with TR of 600 ms, flip angle of 5°, and TE of 3.49 ms. Simulation show an expected flow-in distance of about 40 cm, before signal drops below a detectable level.

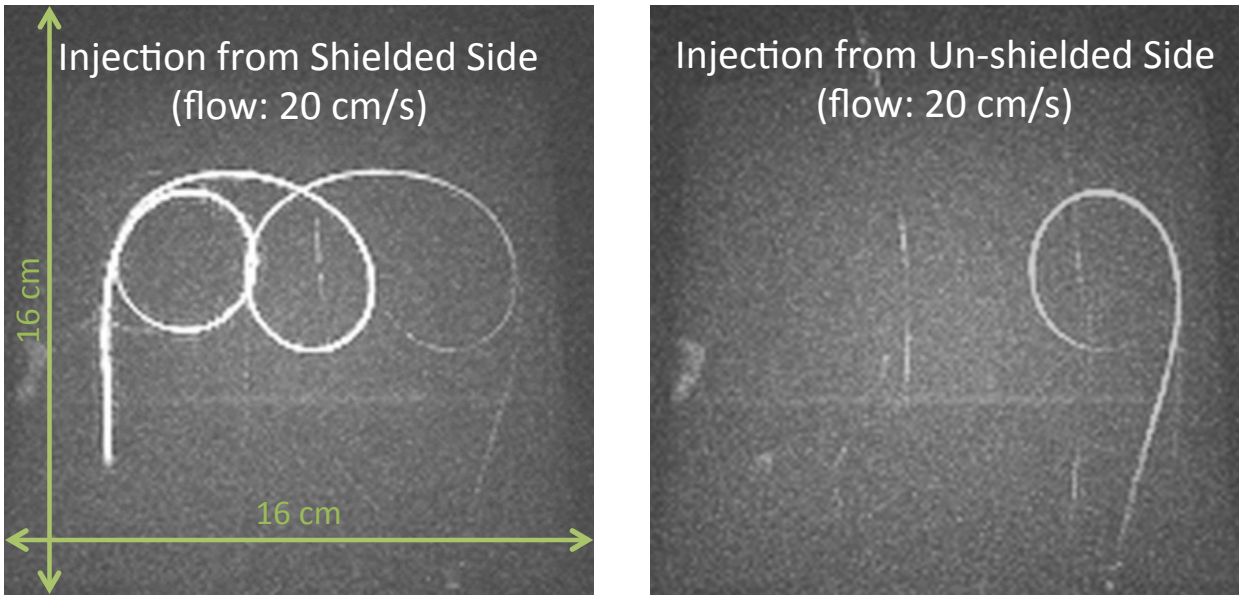

Figure 5.5: Flow phantom images (acquired with non-selective inversion recovery MPRAGE sequence with total acquisition time of 5.1 min., 256 x 230 matrix, 16 cm x 16 cm FOV, slice thickness of 1 cm, TR of 1500 ms, flip angle of 5 degrees, TE of 3.49 ms, and TI of 203 ms) comparing saline injections with and without a shielded catheter. Saline injected from the unshielded side begins to experience nulling pulses before saline injected from the shielded side. As predicted, saline injected from the shielded side has a substantially higher flow-in distance compared to the saline injected from the unshielded side.

5.3 Adiabatic Pulses

Standard inversion pulses are susceptible to B_1 and B_0 inhomogeneity. A class of inversion pulses called Adiabatic pulses [65, 66] are used to robustly invert spins in the presence of RF and B_0 inhomogeneity – the two biggest challenges in MRI. This robustness is, in part, due to the fact that adiabatic pulses invert spins for any pulse amplitude over a certain threshold. An adiabatic pulse, also called the hyperbolic secant pulse, is given by

$$B_1(t) = A(\text{sech}(\beta t))^{1+iu} \tag{5.5}$$

where A is the amplitude of the pulse, and constants β and μ define the bandwidth. Due to the magnitude of the pulses in MRI, it is convenient to express the amplitude of a B_1 pulse in terms of units of Gauss [G], where 1 G = 100 μT.

As mentioned before, the air-tissue boundary in MRI causes about a 10 ppm (equivalent to 3003 Hz at 7T) shift in the precession frequency, and thus transmit and receive frequency, of the spins next to the boundary. The bandwidth, BW, for an adiabatic pulse in rad/s is given by

$$\text{BW} = 2\mu\beta \tag{5.6}$$

Figure 5.6 is a graph of hyperbolic secant pulse with duration of 4 ms, μ of 5 and β of 1887 rad/s (BW of 18,868 rad/s or 10 ppm).

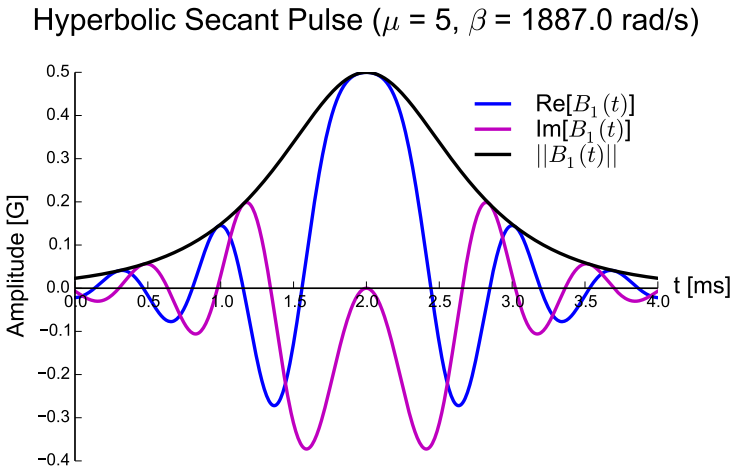

Figure 5.6: Graph showing the real and imaginary parts along with the envelope for a certain adiabatic pulse (A = 0.5 G, μ = 5, and β = 1887 rad/s).

The Bloch Equation, Equation 2.4, can be solved to calculate magnetization, **M**, after an application of an RF pulse, $B_1(t)$. On this time scale we can ignore the T_1 and T_2 relaxation

terms, so that the equation in matrix form becomes

$$\frac{d\mathbf{M}}{dt} = \begin{bmatrix} 0 & (\gamma B_0 - \omega) & -\gamma B_{1,y}(t) \\ -(\gamma B_0 - \omega) & 0 & \gamma B_{1,x}(t) \\ \gamma B_{1,y}(t) & -\gamma B_{1,x}(t) & 0 \end{bmatrix} \begin{bmatrix} M_x \\ M_y \\ M_z \end{bmatrix} \tag{5.7}$$

For the 4 ms pulse shown in Figure 5.6, the 3 components of the magnetization are shown in Figure 5.7.

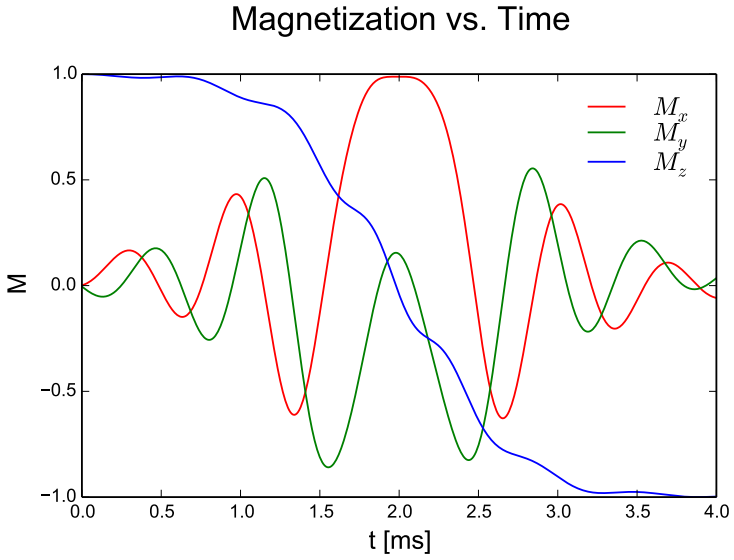

Figure 5.7: Graph showing the 3 components of the simulated magnetization after a 4 ms adiabatic pulse (A = 0.5 G, $\mu = 5$, and $\beta = 1887$ rad/s). At the end of the pulse, the longitudinal magnetization, M_z is flipped 180°.

As mentioned previously, adiabatic pulses fully invert spins for pulse amplitudes over a certain threshold. Figure 5.8 is a graph of magnetization versus pulse amplitude for the same 4 ms pulse. M_z is fully inverted for pulse amplitudes larger than A = 0.3 G.

The inversion profile over a range of frequencies can be simulated by solving Equation 5.7. Also, when $\mu \geq 2$, the inversion profile is approximately given by [65]

$$\frac{M_z}{M_0} \approx \tanh\left(\frac{\pi}{2}\left(\frac{\omega}{\beta} + \mu\right)\right) \tanh\left(\frac{\pi}{2}\left(\frac{\omega}{\beta} - \mu\right)\right) \tag{5.8}$$

Both the estimated and simulated inversion profile over a range of pulse frequencies is shown in Figure 5.9. As expected, this pulse is able to invert off-resonance spins over a bandwidth of 10 ppm, and should be suitable to use in areas close to the lungs.

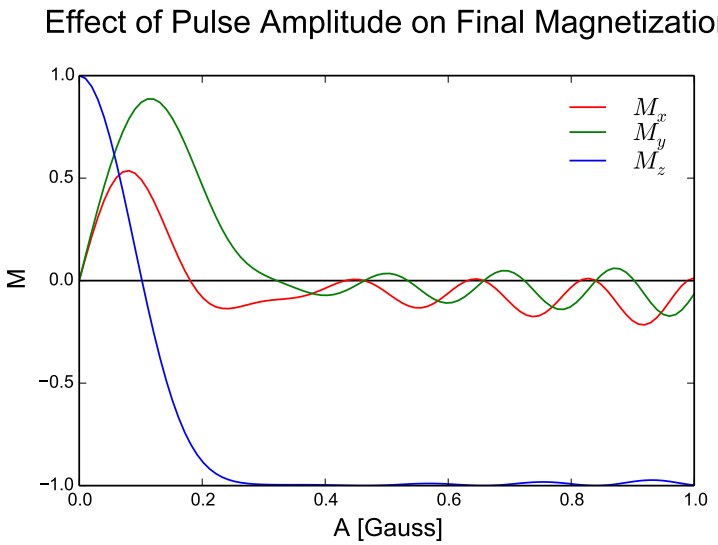

Figure 5.8: Graph showing the 3 components of the simulated magnetization after a 4 ms adiabatic pulse over a range of amplitudes. When A is above 0.3 G, the magnetization is fully inverted.

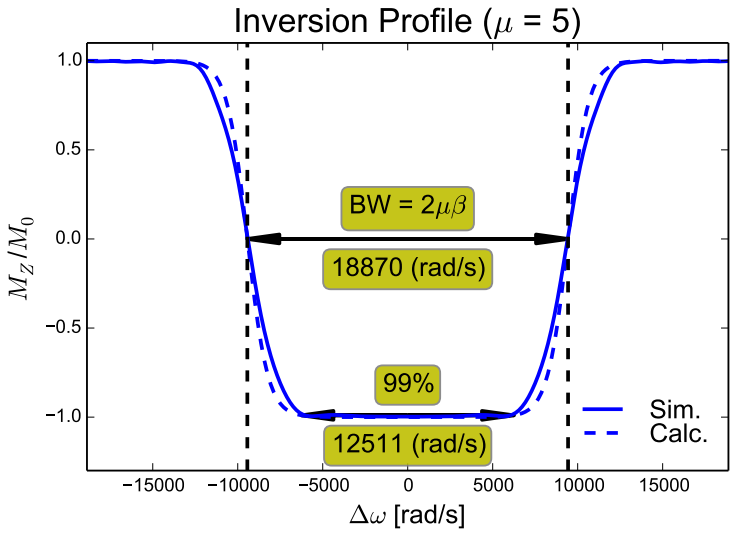

Figure 5.9: Simulated inversion profile for an adiabatic pulse demonstrating inversion of off-resonance spins over a bandwidth of 10 ppm (18870 rad/s at 7T) away from resonance. Simulated results agree quite well with the calculated results from Equation 5.8.

The adiabatic pulse described above was implemented and verified on a 7T Bruker Scanner. A solution containing a mixture of cupric sulfate ($CuSO_4$) and water was prepared in a 15 ml tube. Similar to manganese chloride described earlier, $CuSO_4$ dissolved in water acts as a T_1 shortening agent. The T_1 of the solution was set to be 300 ms. An inversion recovery Gradient Echo (IR-GRE) sequence (128 x 128 matrix, FOV of 4.5 cm x 4.5 cm, slice thickness of 0.9 cm, TR of 1000 ms, TE of 6 ms, flip angle of 90° and TI of 203 ms) was implemented with the adiabatic inversion pulse. The power of the adiabatic pulse was slowly increased from 0 W to 800 W (maximum power allowed by the scanner amplifiers). Figure 5.10 shows an image of the axial slice through the phantom at 0 W power and a corresponding signal vs. power graph as the power is being ramped up. As predicted by simulations (Figure 5.8), the adiabatic pulse is able to fully invert magnetizations at pulse powers above 100 W.

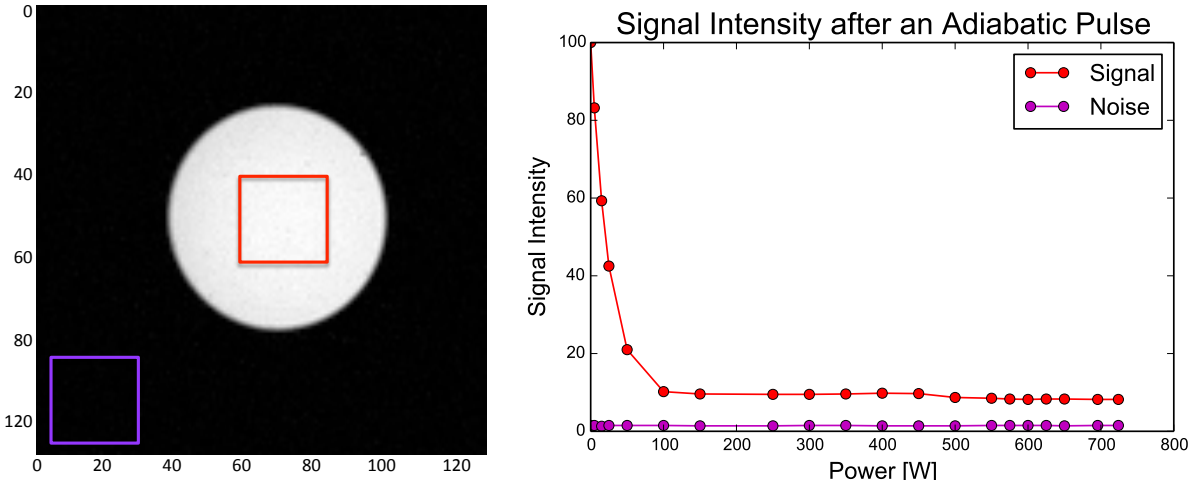

Figure 5.10: On the left is an image of an axial slice of a tube filled with a solution of $CuSo_4$ collected with a GRE sequence. On the right is a graph of signal intensity in the tube vs. pulse power of an adiabatic pulse. An IR-GRE pulse sequence with an adiabatic inversion pulse over 100 W nulls the signal inside the tube.

To further assess the adiabatic pulse, the same solution of $CuSo_4$, a solution of oil and a solution of alcohol each in a 2 ml tubes were imaged. The power for the adiabatic pulse was set to 500 W, and TI time was slowly changed from 190 ms to 600 ms. A 32 x 32 axial slice is shown in Figure 5.11. Also in the figure is a graph of the average signal from the center of the phantom versus TI time. The IR-GRE sequence with an adiabatic inversion pulse is able to sequentially null all three phantom solutions.

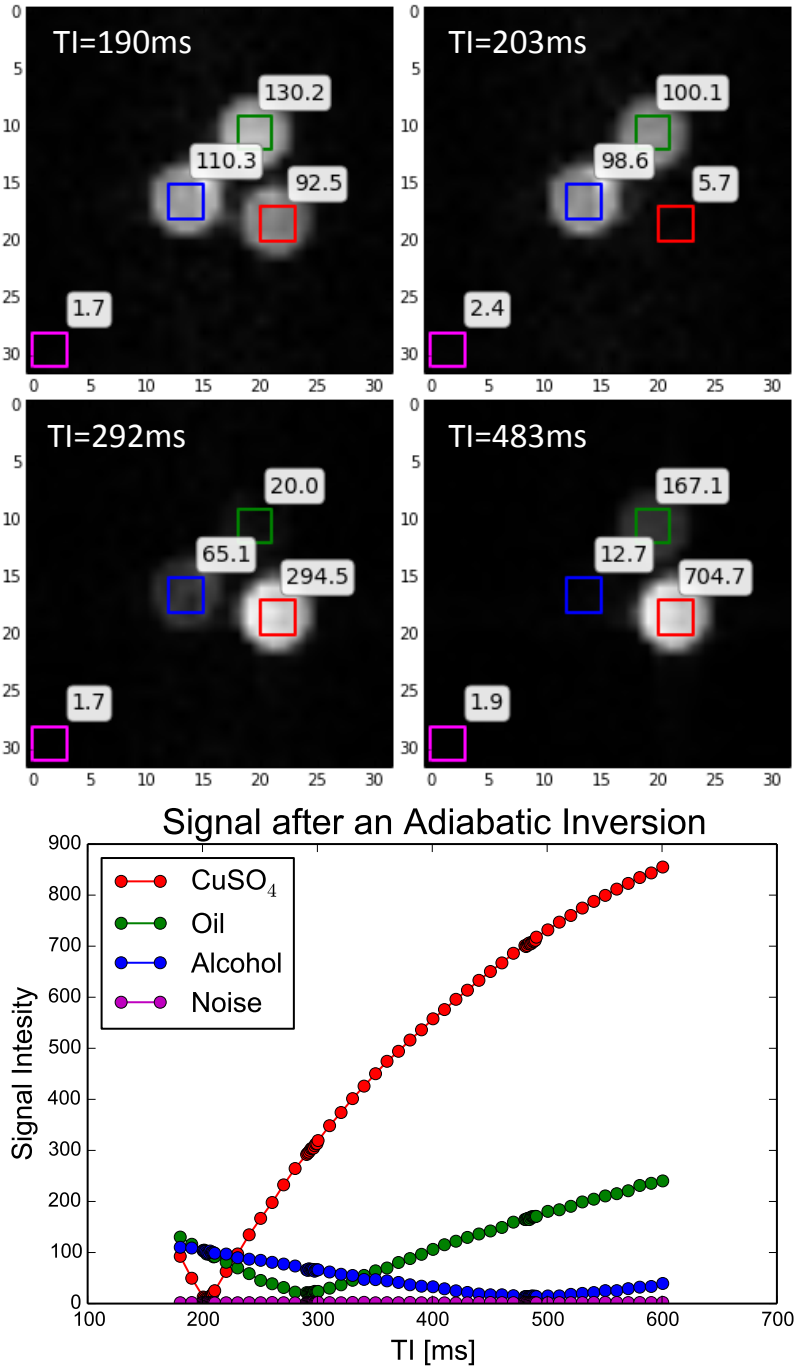

Figure 5.11: At the top is a series of four images with different TI times following an adiabatic inversion pulse. On the bottom is a graph of signal vs. TI time. A single adiabatic pulse can robustly null each of the 3 tubes.

5.4 Multiple Inversion Recovery

We have seen that we can reliably null a single tissue. To null multiple tissues, we decided to use Multiple Inversion Recovery (MIR) sequence [67]. MIR uses a series of inversion pulses following a saturation pulse to robustly null multiple background tissues. For our case, the saline inside the RF-catheter will not experience the MIR pulses and will retain all of its magnetization into the imaging stage. Figure 5.12 is a diagram of pulses for the MIR sequence.

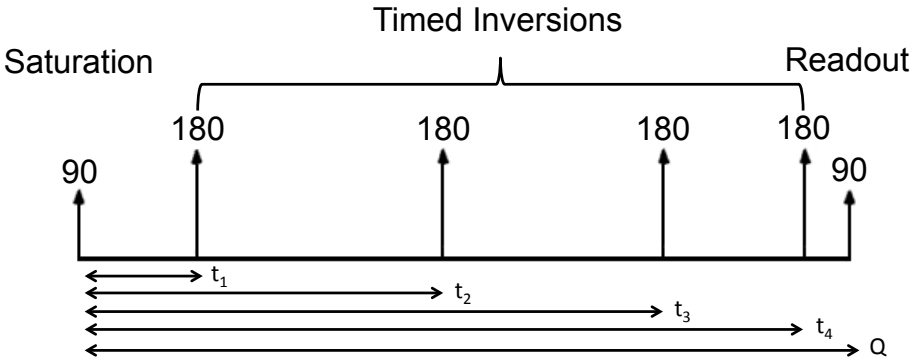

Figure 5.12: Diagram of the pulses in Multiple Inversion Recovery pulse sequence. MIR uses a series inversion pulses following a saturation pulse to robustly null multiple background tissues at precisely the same time, Q.

The longitudinal magnetization after a 2-Inversion MIR sequence is given by

$$M_z(t = Q) = 1 + 2e^{-(Q-t_1)/T_1} - 2e^{-(Q-t_2)/T_1} - e^{-Q/T_1} \tag{5.9}$$

The background tissue in the heart is composed primarily of myocardial muscle, pericardial fat, and blood. Assuming nominal parameters for T1-relaxation of these tissues from Table 2.1, we have optimized the MIR sequence to null each of these background tissues to $< 0.1\%$. Even with some variation (up to 10% uncertainty) in T1-relaxation values, the MIR sequence is still able to suppress the background tissue to $< 1\%$. Figure 5.13 shows the simulated longitudinal magnetization for muscle, fat, and blood. If we time the saline injection to occur right after the 1st inversion pulse, it will be shielded from all of the preceding pulses.

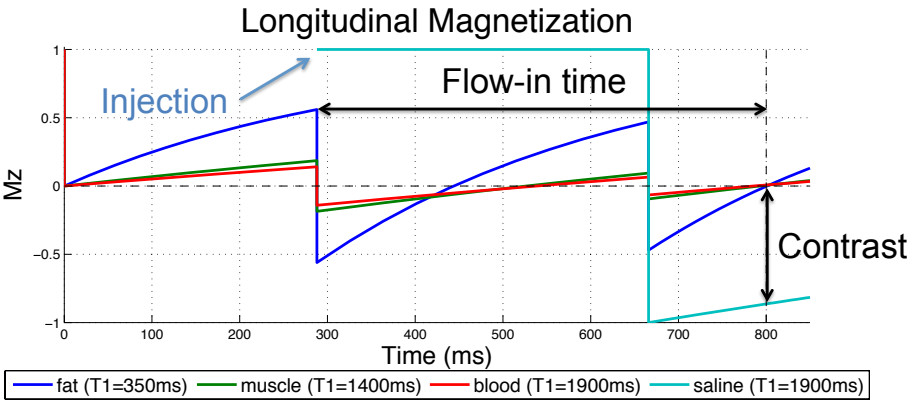

Figure 5.13: Simulated longitudinal magnetization of fat, muscle, blood and injected saline during a MIR sequence. The saline is shielded by the RF catheter from the first two pulses. This sequence along with the RF catheter should be able to achieve good contrast, as well as long flow-in time for the saline.

The sequence in Figure 5.13 has been optimized for highest contrast between the saline and the three background tissues and to allow for enough flow-in time (500 ms) of the saline into heart. The simulated sequence along with the RF catheter is able to achieve a 100:1 SNR, which should be more then sufficient for clinical images.

To test the sequence, we again utilized a 7 Tesla small animal scanner at the Berkeley Preclinical Imaging center. Although the T_1s will be different due to the higher field strength, the results will be directly translatable to the clinical 3 Tesla scanner.

A standard Gradient Echo (GRE) sequence was modified to include a saturation pulse and 2 adiabatic inversion pulses. Figure 5.14 shows the MIR prep added to the front of the GRE sequence (the GRE sequence diagram is shown in Figure 2.4).

To simulate fat and muscle tissues, oil and cupric sulfate ($CuSO_4$) solutions were prepared and put into 2 ml tubes. First, a standard GRE sequence (128 x 128 matrix, FOV of 2.25 cm x 1 cm, Slice Thickness of 0.9 cm, TR of 2000 ms, and TE of 6 ms, and flip angle of 90°) was acquired of the phantom. An axial slice of the phantom is shown in Figure 5.15A. Both oil and $CuSO_4$ solution have a fairly high signal, 38.8 and 101.2 respectively. Next a single inversion was added to try to null each solution individually. A T_1 mapping sequence was used to estimate the T_1 relaxation time for each solution. T_1 of the $CuSO_4$ solution was measured to be 300 ms and T_1 of oil was measured to be 492ms. Images with inversion times of 203 ms and 341 ms are shown in Figure 5.15B and C. Both the $CuSO_4$ and oil solutions were individually nulled by an application of a single adiabatic inversion pulse.

The final step was to apply the MIR sequence. Equation 5.9 was minimized using Nelder-Mead method implemented in SciPy. The predicted magnetization is shown in Figure 5.16, and the result of the MIR sequence acquired with $t_1 = 840$ ms, $t_2 = 1351$ ms, and $Q = 1500$ ms is shown in Figure 5.15D.

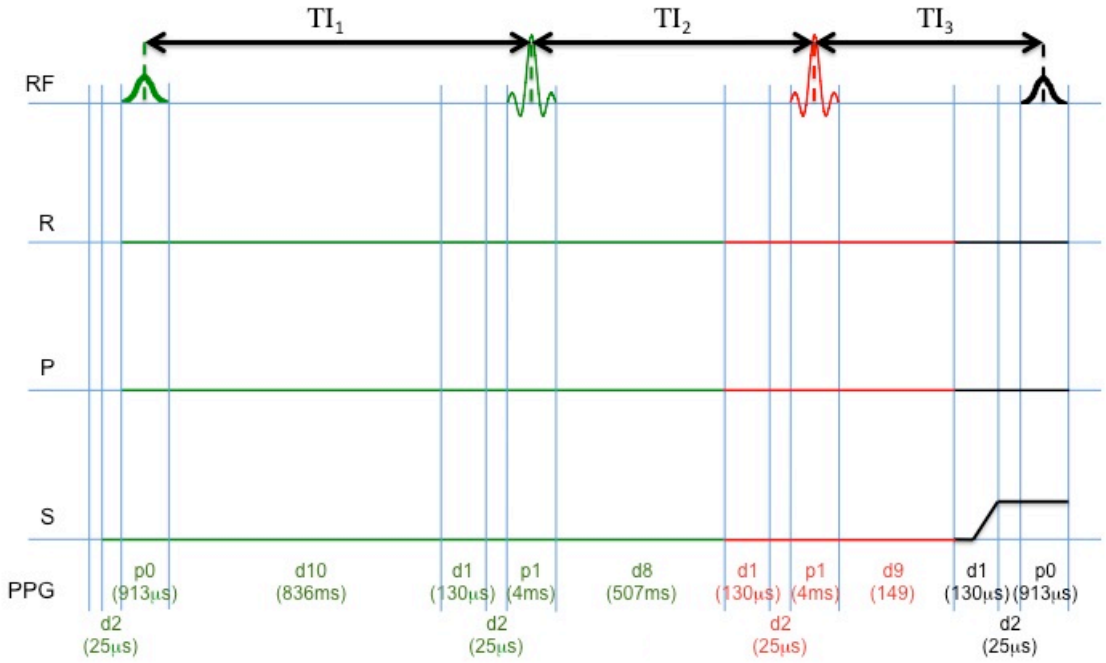

Figure 5.14: Sequence Diagram of MIR sequence on the 7T Bruker scanner. A saturation pulse is followed by two adiabatic inversion pulses before the standard GRE imaging sequence.

Both simulations and measurements show that multiple inversion recovery does an excellent job nulling multiple tissues. It also appears from the simulations that the in-flow time is primarily controlled by the lowest T_1 species, which is fat.

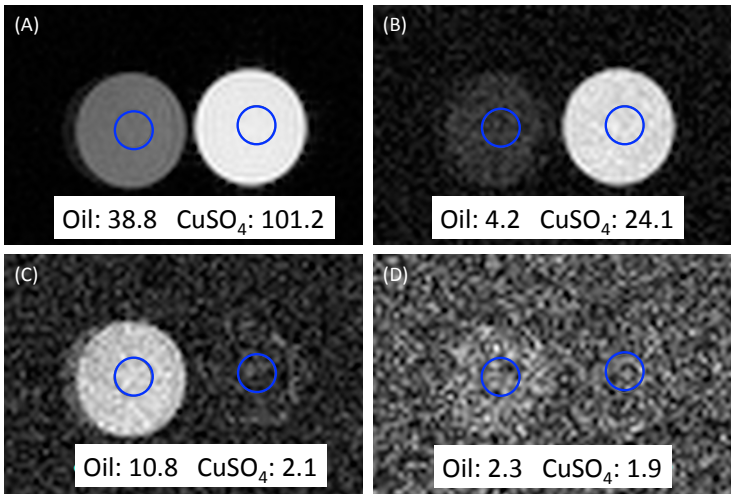

Figure 5.15: (A) is an image of an axial slice of a 2 solution phantom acquired with a standard GRE sequence. The left tube is oil/water solution with a $T_1 = 492$ ms and the right tube is a $CuSO_4$ solution with a $T_1 = 300$ ms. (B) is the phantom image acquired after a single inversion adiabatic pulse ($TI = 341$ ms). (C) is the phantom image acquired after a single inversion adiabatic pulse ($TI = 203$ ms). (D) is the image of the phantom after a 2-Inversion MIR sequence optimized to null both solution. MIR is able to null both Oil and $CuSO_4$ almost down to the noise floor.

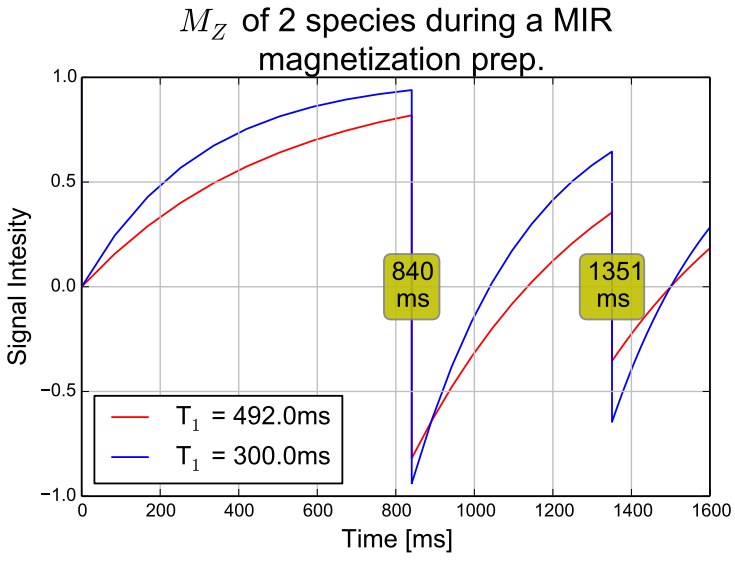

Figure 5.16: Predicted longitudinal magnetization for 2 solutions after a 2-Inversion MIR sequence. At t = 1500 ms, both of the tissues should have no signal.

5.5 Spectral Spatial Pulses

In order to have better control over the in-flow time we proposed to use Spectral Spatial (SS) pulses [68] during the imaging stage of the sequence. SS pulses have the ability to selectively excite (or in this case not excite) species that are off-resonance. Fat happens to have a 3.5 ppm shift relative to water, so SS pulses are well suited to not excite the fat signal.

SS pulses are used to independently excite over spatial position and frequency. Table 5.1 is a list of parameters that were used to design a true-null SS pulse to not excite the fat signal.

Parameter	Value	Description
f_{null}	1.043 kHz	Null center frequency (chemical shift of fat at 7T).
SBW	6	Spatial bandwidth.
TBW	4	spectral time-bandwidth.
$G_{spatial}$	18.75 G/cm	Maximum strength of spatial gradient lobes.
G_{spectral}	1 G/cm	Spectral gradient strength.
S	290 G/cm/ms	Maximum gradient slew rate.

Table 5.1: Table of parameters used in designing a Spectral Spatial Pulse.

Given the constraints of the system (Gradient Strength, Gradient Slew Rates and RF power) and parameters defined above, an SS pulse with characteristics shown in Table 5.2 was designed.

Characteristic	Value	Description
T	5.9 ms	Total pulse duration.
t_{sp}	240 ms	Subpulse duration.
BW_{sp}	25.032 kHz	Subpulse bandwidth.
S_{th}	0.31 cm	Slice Thickness.
n_{sp}	16	Number of RF subpulses (number of gradient lobes).
t_{sp}	0.24 ms	Duration of each subpulse.
passband	0.676 kHz	Spectral passband for excited signal.

Table 5.2: Table of Spectral Spatial Pulse characteristics.

The simulated Gradient and RF waveforms are shown in Figure 5.17. The RF pulse envelope and the spectral gradient, G_{spectral}, control the frequency excitation profile. The RF subpulses and the spatial gradient, G_{spatial} control the spatial excitation profile (influences parameters like slice thickness).

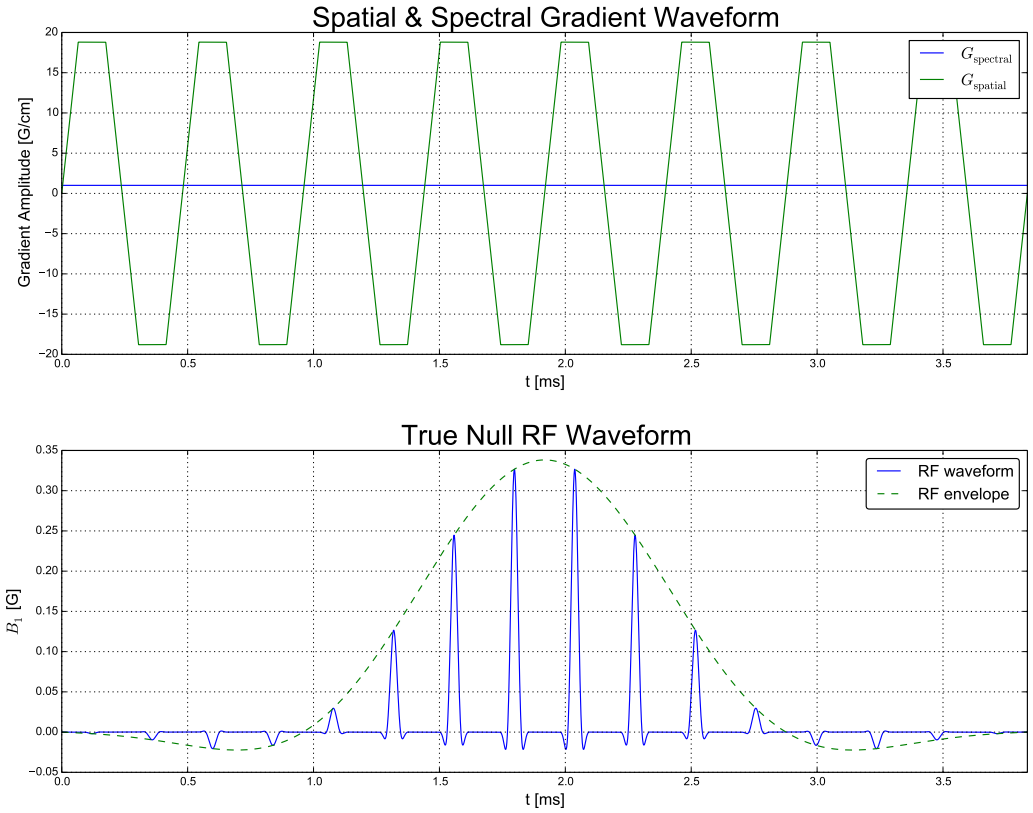

Figure 5.17: Gradient and RF Waveforms of Spectral Spatial Pulse designed to null fat at 3.5 ppm.

To characterize the expected performance of the above SS pulse, the slice and frequency profiles were first simulated and then measured with a standard Spin Echo sequence (64 x 64 matrix, 4.5 cm x 4.5 cm FOV, slice thickness of 3.2 mm, TR of 100 ms, TE of 9 ms, and flip angle of 90°). Measured and Simulated slice profiles are shown in Figure 5.18. The y-axis is the spatial slice profile, and the x-axis is the spectral profile. As expected the slice thickness is about 3 mm, and there is no excitation at 1.048 kHz – the chemical shift of fat.

To validate the above sequence a water/oil phantom was created. Two 2ml tubes, one filled with $CuSO_4$ solution and the other with oil, were placed in a 50 ml falcon tube filled with water. Two axial slices were acquired with a standard Spin Echo sequence (128 x 128 matrix, 4.5 cm x 4.5 cm FOV, slice thickness of 3.2 mm, TR of 2000 ms, TE of 9 ms, and flip angle of 90°). As expected, the sequence acquired with the SS pulse (Figure 5.19B) produces significantly less signal from oil, and in fact has about a 10-fold reduction in oil signal as compared to the sequence acquired with a conventional Sinc pulse (Figure 5.19A).

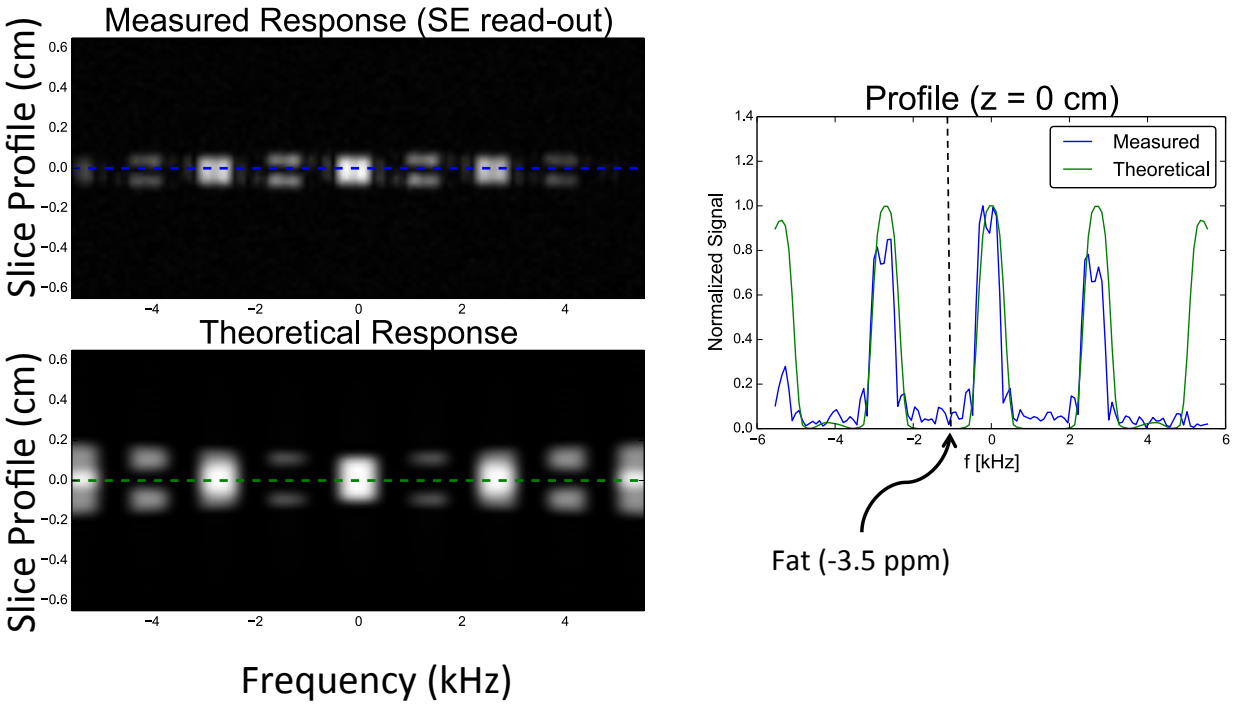

Figure 5.18: Simulated and measured spectral and spatial profile for a SS pulse. The SS pulse is designed not to excite fat in a slice thickness of about 3 mm. Measured results agree closely with the simulated results.

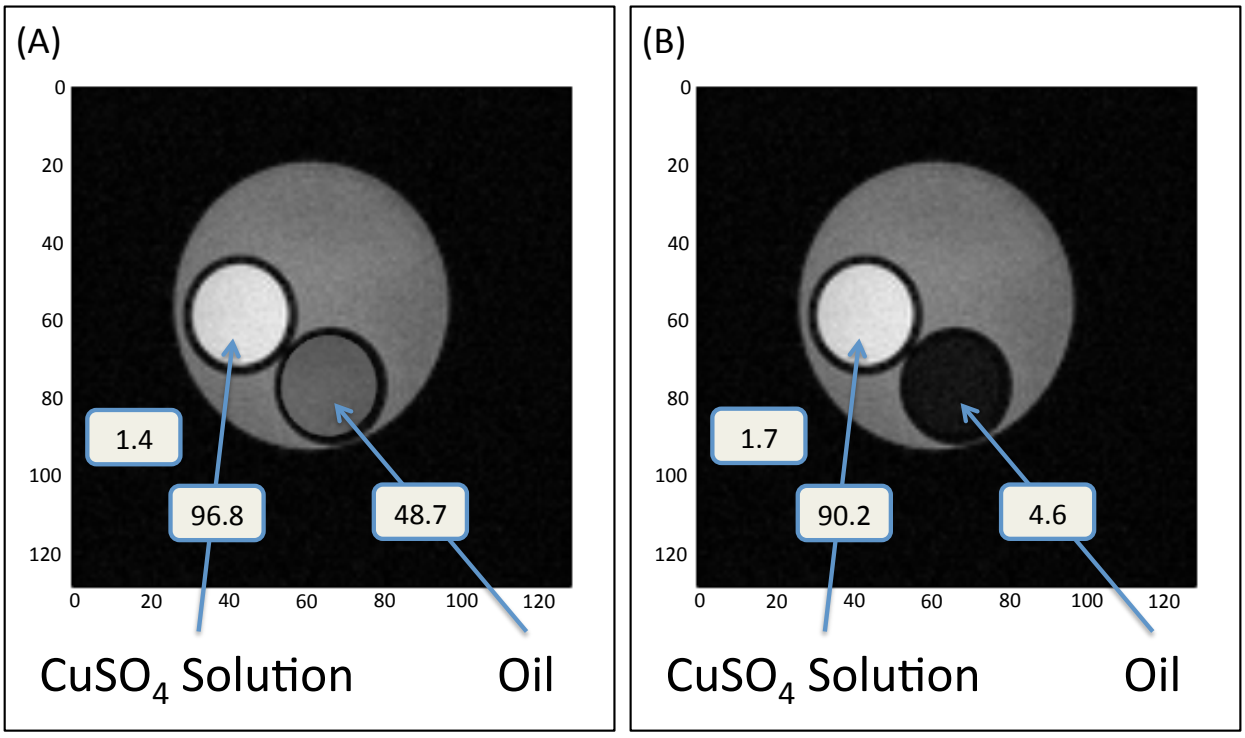

Figure 5.19: Comparison of water/oil phantom with and without a Spectral Spatial pulse. (A) is an image acquired with a conventional Sinc pulse, while (B) is an image acquired with a spectral spatial pulse. The spectral spatial pulse has about a 10-fold lower signal as compared to a conventional pulse.

5.6 Flow Phantom Testing

The next step was to combine MIR, adiabatic inversion pulses and spectral spatial pulses into one sequence. SS pulses were implemented within a single-shot FLASH framework and combined with adiabatic inversion MIR prep sequence.

A flow phantom (Figure 5.20) allowing injections with and without shielded catheter was designed to fit into the smaller 7T bore. The main body of the phantom was made out of 2.5 in OD cast acrylic. A bifurcating channel was then laser cut into a 1/8 in piece of acrylic and placed within the main vessel. As with previous iterations of phantoms, the phantom solution was made with $CuSO_4$-Water mixture with a T_1 of 300 ms. The injected saline had a T_1 of about 1500 ms. Two 1/8 in OD PTFE tubes fed into the bifurcating channel. One of the tubes was shielded with a 50 μm to 100 μm layer of electroplated copper, segmented into 0.5 cm to 1 cm links with 1 mm gaps (the links were 0.5 cm around the bend of the catheter to decrease the radius of curvature). The other tube was left unshielded. Another 1/8 in OD PTFE tube provided an outlet for the flowing saline.

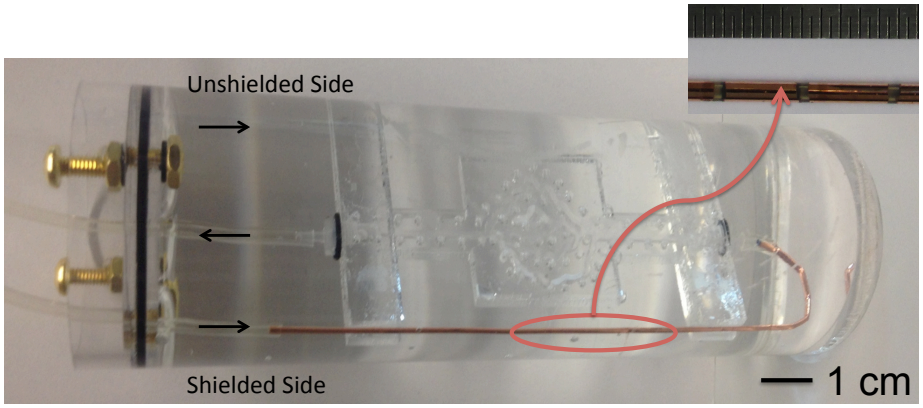

Figure 5.20: Three-port Flow Phantom. The top and bottom ports are the unshielded and shielded inlets respectively. The middle port is an outlet. The shielded layer was segmented into 0.5 cm to 1 cm sections with 1 mm gaps (the links were 0.5 cm around the bend of the catheter to decrease the radius of curvature).

MIR was designed to null both the 300 ms and the 1500 ms specie. Three single-shot FLASH coronal images were acquired (128 x 128 matrix, 5 cm x 6 cm FOV, slice thickness of 7 mm, TR of 3.686 ms, TE of 1.87 ms, a flip angle of 15°, and a total acquisition time of 572 ms). The first image (Figure 5.21A) has no flow, the second image (Figure 5.21B) is with saline injected through the unshielded side, and the third image (Figure 5.21C) is with saline injected through the shielded side. As with previous flow experiments, the shield layer over the catheter allowed for about a 4-fold deeper saline penetration as compared to the unshielded catheter.

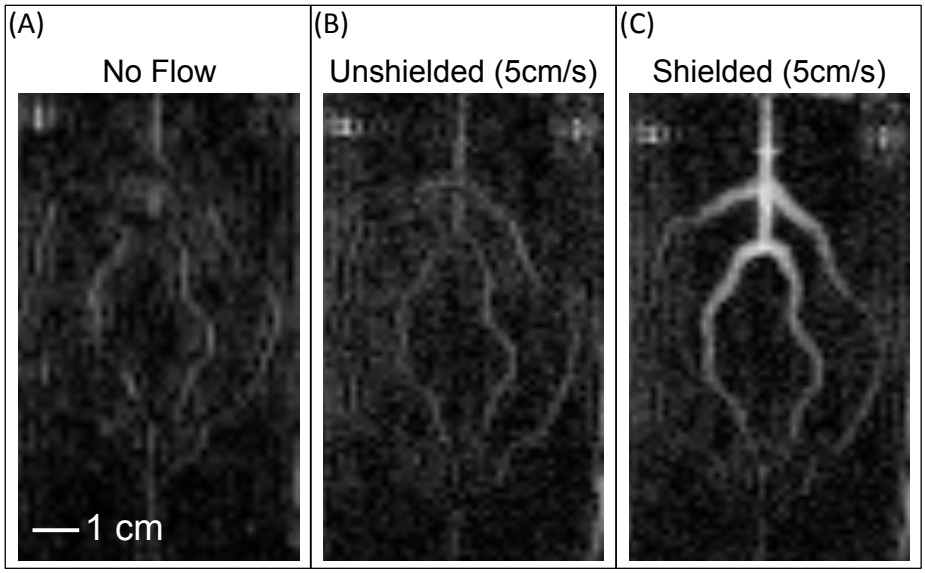

Figure 5.21: Coronal images acquired with adiabatic pulse multiple inversion recovery with spectral spatial single-shot FLASH readout. (A) is an image with no saline flowing. (B) is an image with saline injected through the unshielded side. (C) is an image with saline injected through the shielded side. As with previous flow experiments, the shield layer over the catheter allowed a substantially deeper saline penetration as compared to the unshielded catheter.

5.7 Real-Time MRI with RTHawk

To assess the RF catheter on existing real-time systems, a new phantom was constructed and then imaged at the 3T clinical system with an RTHawk real-time imaging system. The same phantom recipe was followed as the one described in Section 5.2. A hemostatic valve was added to allow for an easy introduction of the RF catheter into the phantom. Figure 5.22 is an image of the completed phantom. A peristaltic pump would be able to continuously pump water through the phantom to simulate blood flow in the coronaries. Saline could then be injected through a catheter introduced through the hemostatic valve.

A new larger catheter was designed to fit freely into the hemostatic valve and be able to maneuver through the bends of the phantom. Tin plated copper ferrules (length: 0.5 cm - 1 cm, ID: 2.3 mm, wall thickness: 150 μm from Thomas and Betts Inc.) were glued over 7 French PEBAX^{TM} tubing (Apollo Medical Inc.). The whole assembly was then covered with P2-140-006-40-CLR clear Palladium^{TM} heat shrink (Cobalt Polymers Inc.). The catheter is shown in Figure 5.22.

Imaging was done with an RTHawk real-time system on a 3T scanner. A peristaltic pump was set to continuously pump water at 20 cm/s. A shielded catheter. Images were acquired with at 37 Frames/sec with a GRE sequence with spiral readout (135 x 135 Matrix,

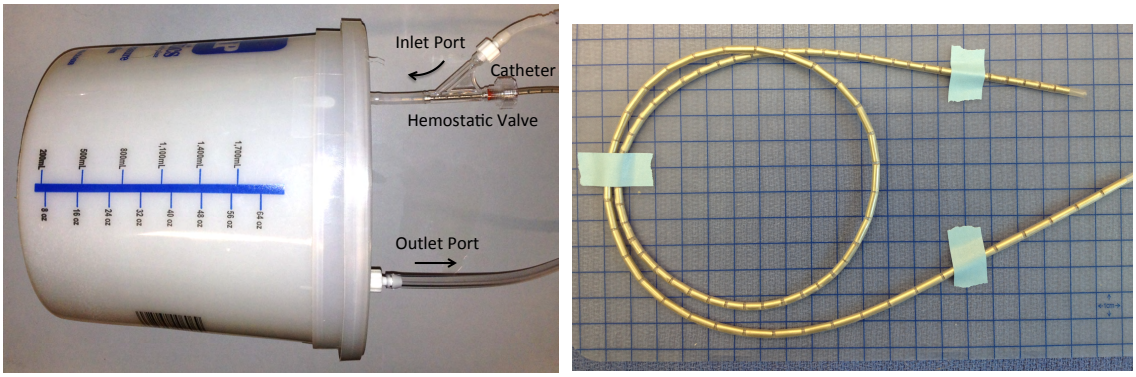

Figure 5.22: (Left) Flow phantom used on the RTHawk system. (Right) RF Catheter. A hemostatic valve allows for an insertion of the catheter into the phantom.

32 cm x 32 cm FOV, slice thickness of 5 mm, TR of 13.52 ms, TE of 2.940 ms, and flip angle of 40°). Water (same T_1 as already flowing water) was injected through the catheter into already flowing water inside the phantom. Figure 5.23 shows four frames. Frame 1 is the image prior to the injection – flowing water has no signal. Frame 35 is the image at the onset of injection. Frame 55 is the image at the point of deepest penetration after the injection. Frame 70 is the image collected post injection.

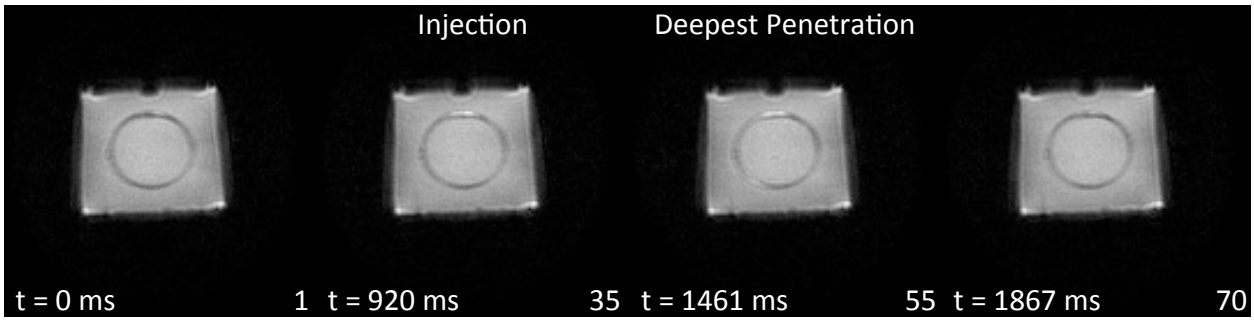

Figure 5.23: Images acquired by the RTHawk real-time system. Shown are 4 frames from a 37 frame/second acquisition. Frame 1 is the image prior to the injection. Frame 35 is the image at the onset of injection. Frame 55 is the image at the point of deepest penetration after the injection. Frame 70 is the image collected post injection. The RF catheter allows for the saline to penetrate into the phantom before being suppressed by the imaging sequence.

The initial testing demonstrated the feasibility of using the RF shielding to protect the saline inside the catheter. However, further modification and optimization need to be done to the stocked sequence in order to get better background saturation.

5.8 Conclusions

We have seen that the RF shielded catheter, together with Multiple Inversion Recovery preparation sequence, adiabatic inversions and Spectral Spatial pulses could reliably null the background tissue as well as allow deep penetration of the injected saline into the vessels. Also, tests done on the RTHawk real-time system are very promising and indicated that this technique could be promising with existing systems. Further work and optimization in modifying existing real-time sequences should greatly improve the currently achieved contrast.

Chapter 6

MPI Angiography: Experimental Evaluation of Feasibility - Tracer Biodistribution and Clearance

MPI is uniquely positioned as a safe imaging modality for patients with CKD due to the use of safer SPIO tracers. SPIOs are cleared through the liver and spleen, as opposed to the kidneys [69]. In assessing MPI's utility in for angiographic imaging, it is important to be able to assess tracer short-term biodistribution as well as long-term clearance from the body. Long term circulation is important for clinical applications such as cardiovascular, stroke and tumor imaging. For angiography with MPI it will be important to have a long circulating particle. On the other hand, excessively long clearance time could be a safety concern and limit the ability to do consecutive imaging studies. Here, I describe the biodistribution and clearance for the two most commonly used tracers in MPI: Ferucarbotran (Meito Sangyo Co., Japan) and LodeSpin (LS-oo8) (LodeSpin Labs, Seattle, WA). I also show that LodeSpin (LS-008) tracer has a long blood circulation time that should be beneficial to angiography applications.

6.1 SPIO Tracers

Ferucarbotran is an aqueous suspension of multi-core carboxydextran-coated magnetite nanoparticles, originally designed as a liver-targeting MRI contrast agent [70, 71, 72], but adopted to be used in MPI. LodeSpin (LS-008) is a PEG-coated single-core magnetite nanoparticle, designed as a long circulating MPI tracer [73, 72]. Table 6.1 is list of characteristics for each tracer.

Name	Ferucarbotran	LS-008
Supplier	Meito Sngyo Co., Japan	LodeSpin Labs, Seattle WA
Coating agent	Carboxydextran	PMAO-PEG
Core Diameter	3 nm to 5 nm	26.3 nm ± 1.5 nm
Hydrodynamic Diameter	45 nm to 72 nm	78
Concentration of Iron (Fe)	5.7 mg/ml	2.35 mg/ml

Table 6.1: Table of MPI tracer characteristics.

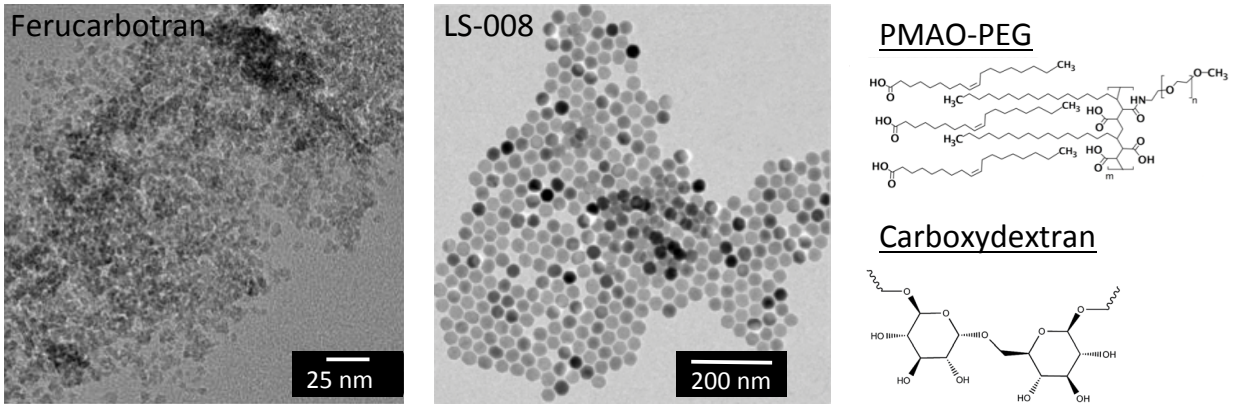

Figure 6.1: TEM images of MPI tracers (images courtesy of LodeSpin Labs) along with a chemical diagram of the coatings.

6.2 Experimental Setup

Six groups of Fisher 344 female rats were used for the biodistribution and clearance experiments. The first group (n = 3, weight = 134 g ± 5 g, 10 weeks old) received an injection of Ferucarbotran, and was imaged over 70 days. The second group (n = 3, weight = 117 g ± 3 g, 8 weeks old) received an injection of Ferucarbotran, and was imaged over 2 days. The third group (n = 3, weight 131 g ± 6 g, 9 weeks old) received an injection of LodeSpin (LS-008), and was imaged over 70 days. The fourth group (n = 3, weight = 119 g ± 8 g, 8 weeks old) received an injection of LS-008, and was imaged over 2 days. The fifth group (n = 2, weight = 157 g ± 4 g, 20 weeks old) received no injection, and was kept alive for 70 days. Finally, the sixth group (n = 3, weight = 116 g ± 5 g, 8 weeks old) received no injection, and was kept alive for 2 days. All groups were euthanized and validation was conducted with inductively couple plasma - optical emission spectrometry (ICP-OES). Figure 6.2 is a flow chart describing the experiment.

Prior to all procedures, animals were anesthetized with an isoflurane/oxygen mixture (induction at 3.5% isoflurane and 1 L/min flow; maintenance at 2-3% isoflurane and 1 L/min flow). For groups 1, 2, 3 and 4, the tracer was diluted in sterile 0.9% saline solution, and

then injected through a catheter as a bolus at a dose of 5 mg Fe/kg into the tail vein of the animal. To ensure complete delivery of the tracer, the catheter lines were flushed with 0.9% saline solution up to a total injected volume of 1 ml. All animal experiments were performed in compliance with the Animal Care and Use Committee (ACUC) at UC Berkeley.

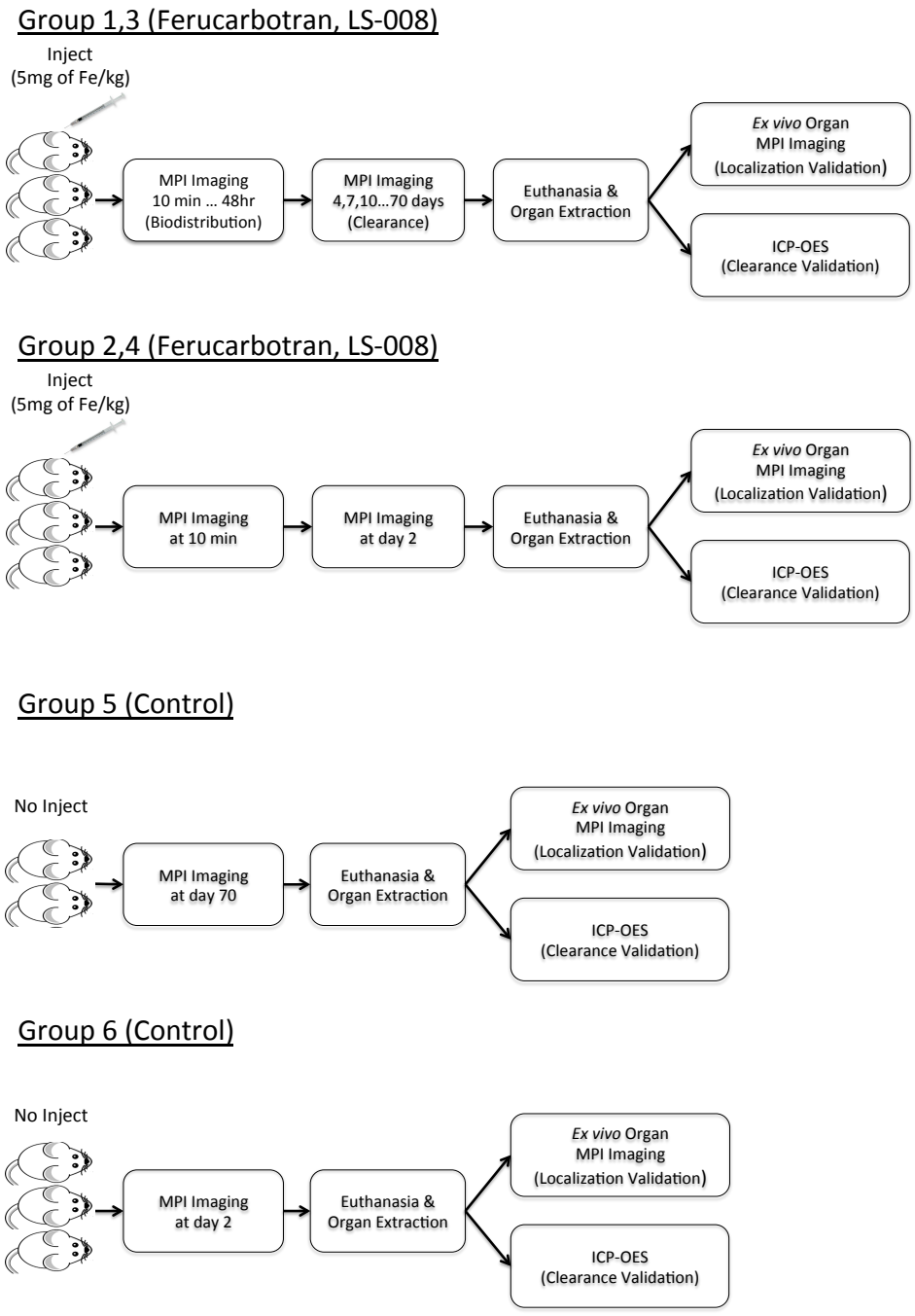

Figure 6.2: Flowchart of the tracer biodistribution and long-term clearance animal experiment.

The rats were imaged with respiratory gating (SA Instruments Inc., Stony Brook, NY) using a 3.5 T/m x 3.5 T/m x 7 T/m field free point MPI imager [38] with a 20.025 kHz and 40 mTpp excitation field in z, and FOV of 4.0 cm x 4.0 cm x 10.5 cm. The animals were positioned in dorsal recumbency for imaging. For Groups 1 and 3, the animals were imaged at 10 minutes, 30 minutes, 1 hour, 2 hours, 4 hours, 6 hours, 12 hours, 1 day and 2 days and then twice a week over the next 70 days. For Groups 2 and 4, the animals were imaged right after the injection and then again at day 2. For Group 5, the animals were imaged at day 70. For Group 6, the animals were imaged at day 2. All animals were ordered from the same facility and kept on the same diet for the duration of the experiment. After the last imaging time point the animals were sacrificed via isoflurane over-dose.

6.3 Blood Half-Life

To assess the blood half-life of each tracer, an ROI was drawn over the jugular vein of each animal at each time point up to 48 hours. A region growing algorithm, seeded with the maximum voxel, was used to isolate the jugular vein. The blood half-life was calculated by using a non-linear least-squares 1st order exponential fit to the average value in the ROI over all animals at each time point. Figure 6.3 shows MPI images of the biodistribution overlaid onto an X-Ray projection image and Figure 6.4 shows blood half-life curves for both tracers over 48 hours. Almost no signal was detected for Ferucarbotran, so no fit was done.

As expected, in animals injected with the liver-targeting agent, Ferucarbotran, most of the tracer cleared into the liver immediately following the injection. On the other hand, the LodeSpin (LS-008) particles persisted in the blood with a half-life of 4.2 hours.

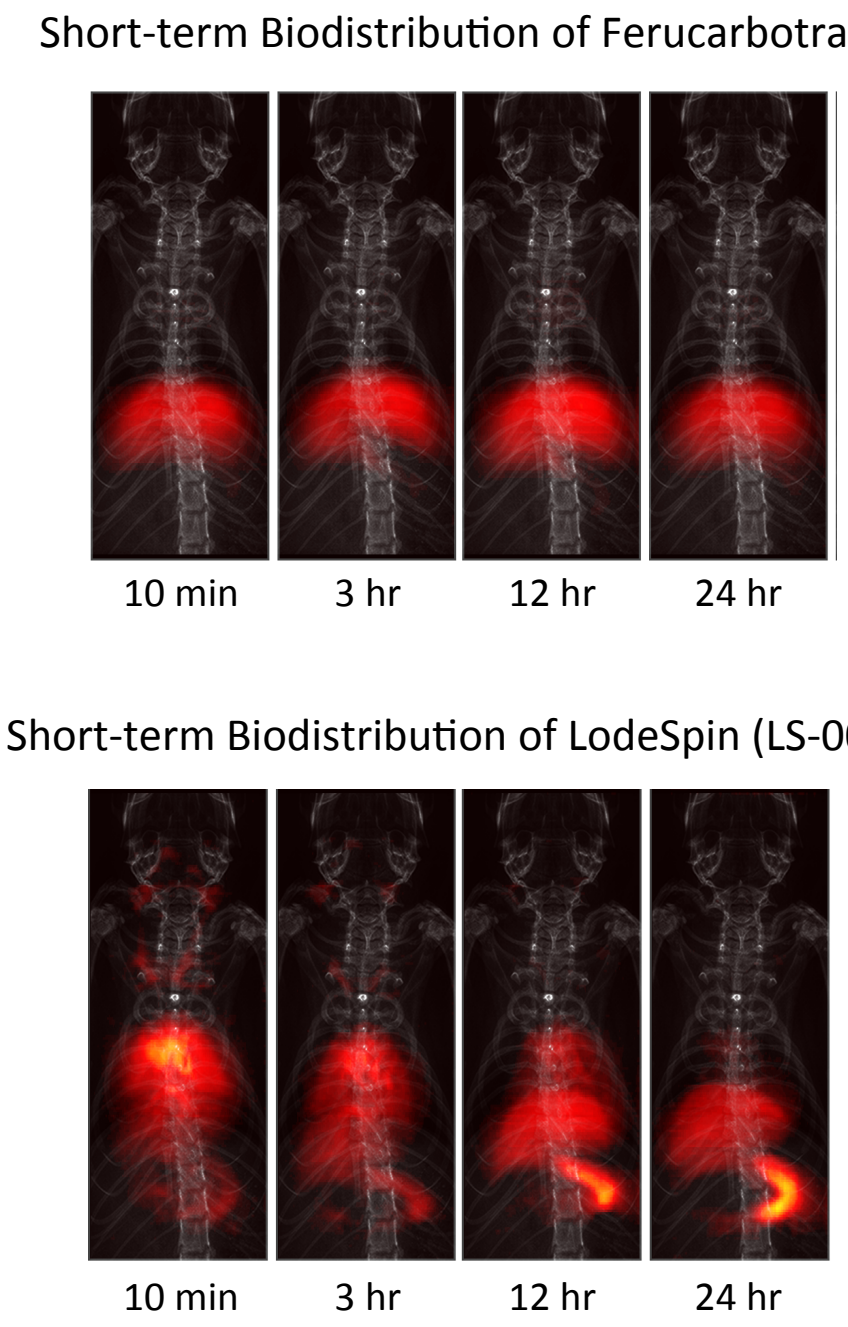

Figure 6.3: Short-term biodistribution MPI images overlaid on an X-ray projection for Ferucarbotran and LodeSpin (LS-008). Ferucarbotran is immediately cleared to the liver, while LodeSpin (LS-008) stays circulating in the blood with a half life of 4.2 hours.

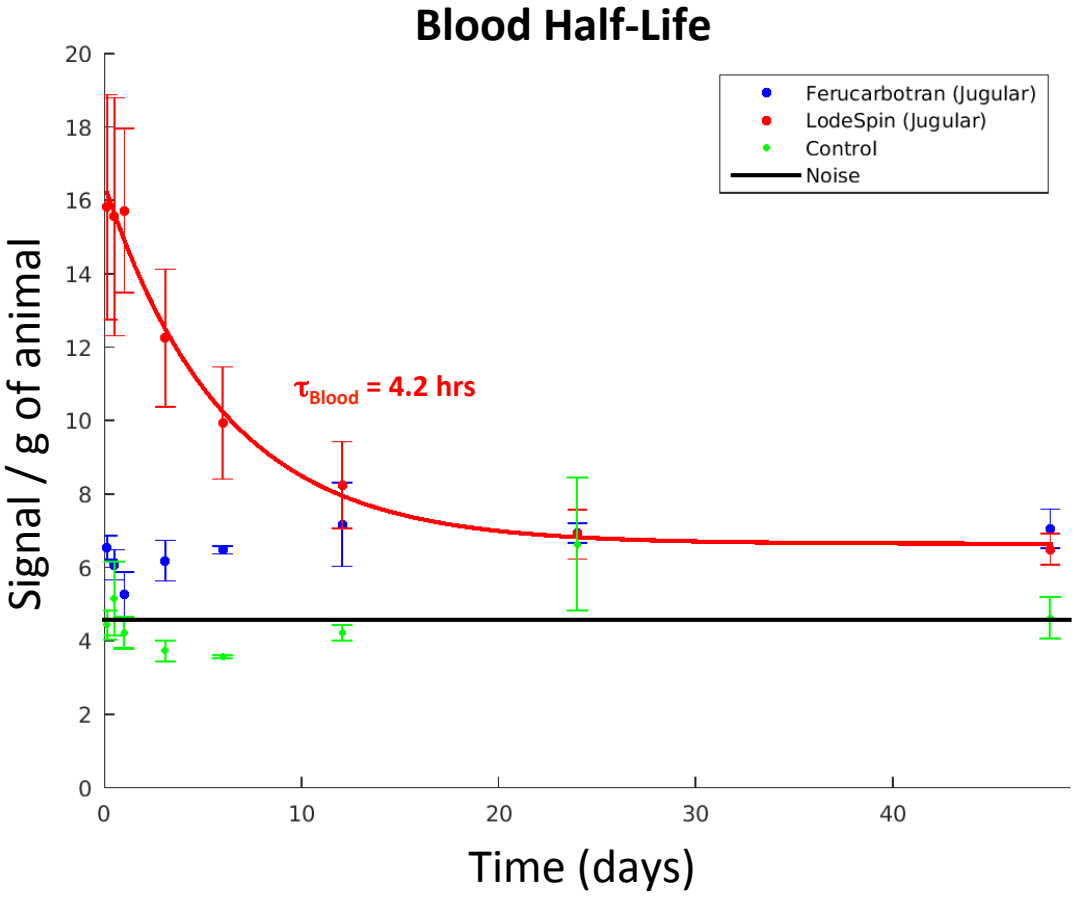

Figure 6.4: Short-term biodistribution curves for Ferucarbotran and LodeSpin (LS-008). As expected, LodeSpin (LS-008) stays in the blood (half-life 4.2 hours), while Ferucarbotran is almost immediately cleared to the liver.

6.4 Long-term Clearance

A similar algorithm to the one used to measure the blood half-life was used to assess the clearance half-life in both liver and spleen. Average signal in both organs was determined for all time points over the 70-day period. Figure 6.5 shows MPI images overlaid on an X-Ray projection image, and Figure 6.6 and Figure 6.7 show iron clearance curves in liver and spleen for Ferucarbotran and LodeSpin (LS-008) over a 70-day period.

Ferucarbotran cleared from the liver with a half-life of 5.6 days and from the spleen with a half-life of 4.0 days. LodeSpin (LS-008) cleared from the liver with a half-life of 6.5 days and from the spleen with a half-life of 18.2 days.

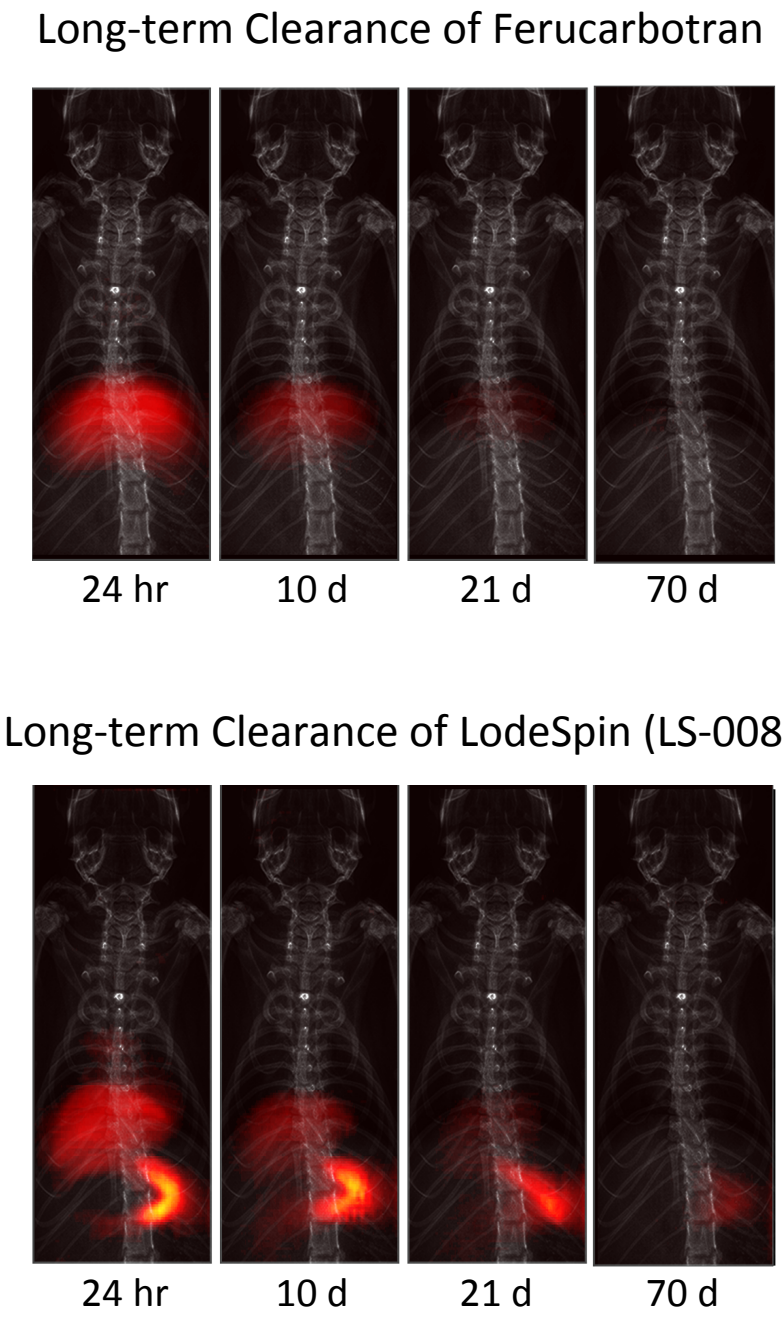

Figure 6.5: Long-term clearance MPI Images overlaid on a projection X-ray for Ferucarbotran and LodeSpin (LS-008). Ferucarbotran is mostly clearing by the liver, while LodeSpin (LS-008) is mostly cleared by the spleen.

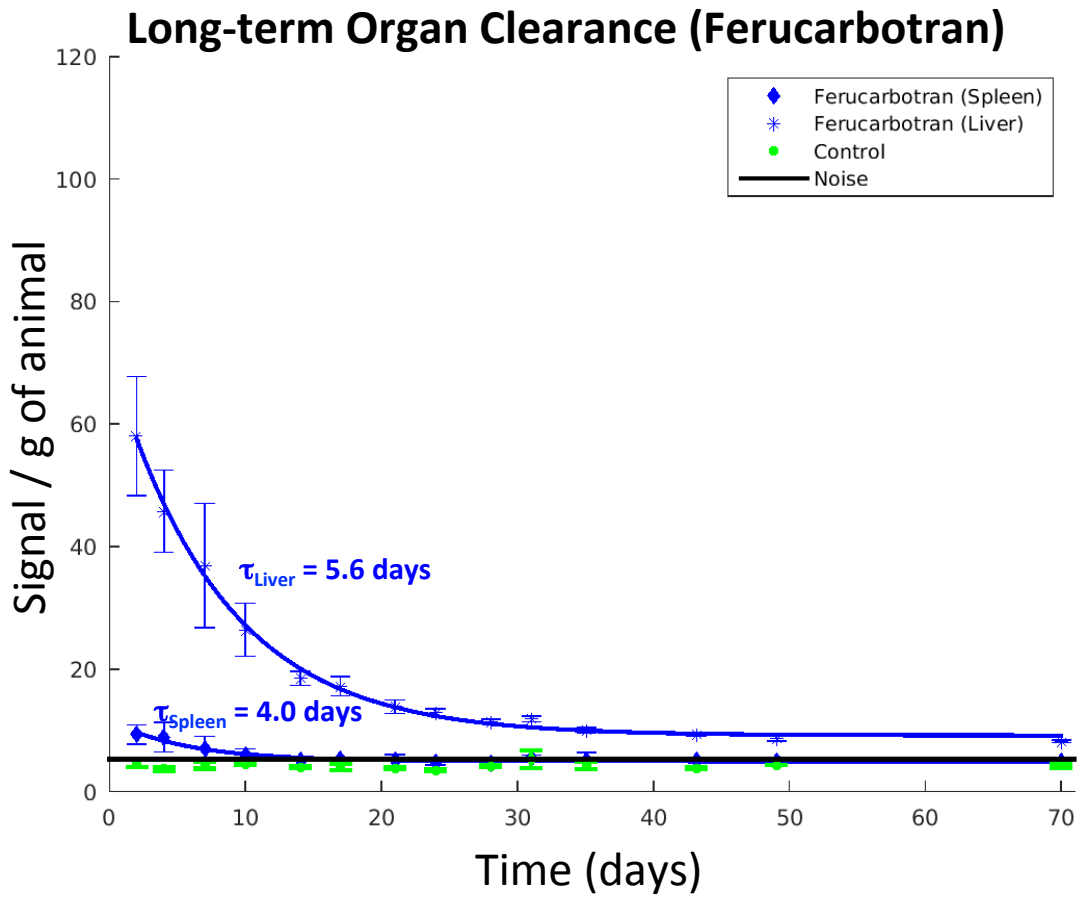

Figure 6.6: Long-term clearance curves for Ferucarbotran. Ferucarbotran is cleared out by the liver (half-life of 5.6 days) and the spleen (half-life of 4.0 days).

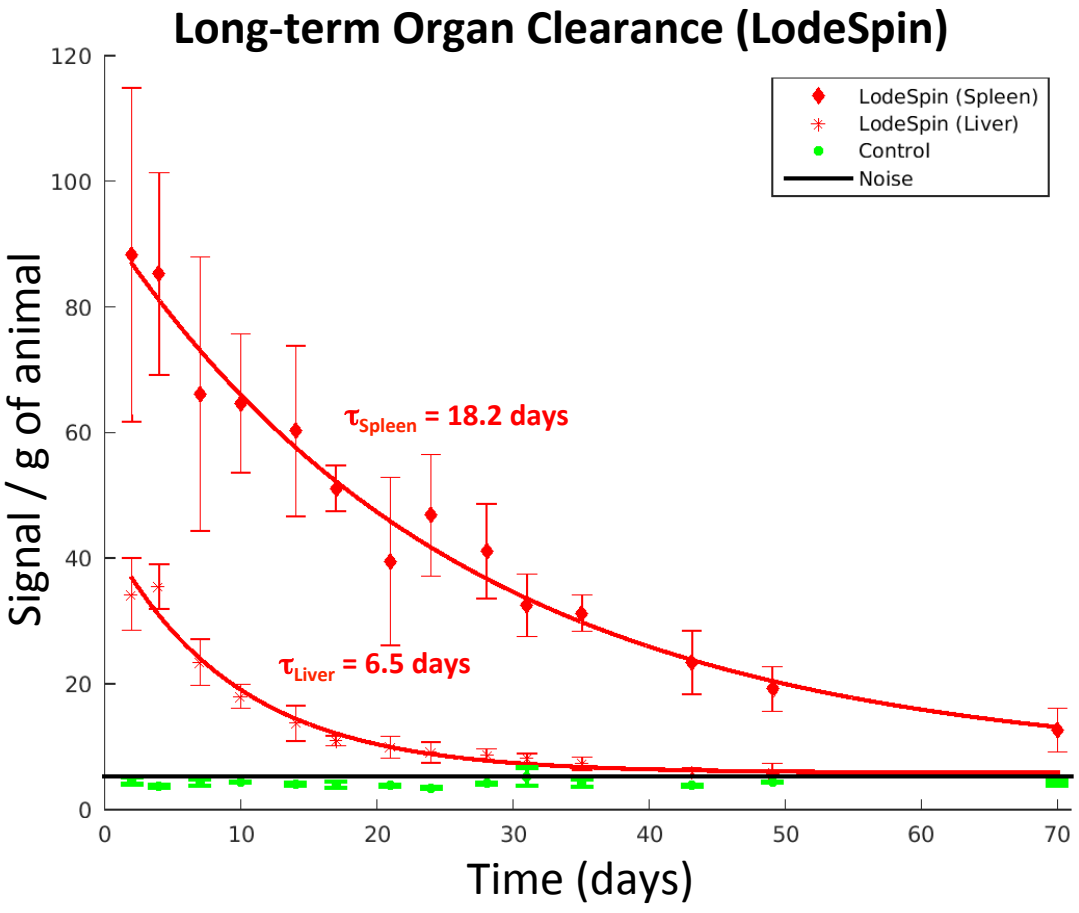

Figure 6.7: Long-term clearance curves for LodeSpin (LS-008) (right). LodeSpin (LS-008) is cleared out by the spleen (half-life of 18.2 days) and the liver (half-life of 6.5 days).

6.5 Iron Localization with *ex vivo* MPI

Following the last time point, all animals were euthanized via an overdose of isoflurane. Liver, spleen, kidneys, lungs and heart were removed and imaged in the MPI scanner following the same imaging protocol as used for *in vivo* imaging.

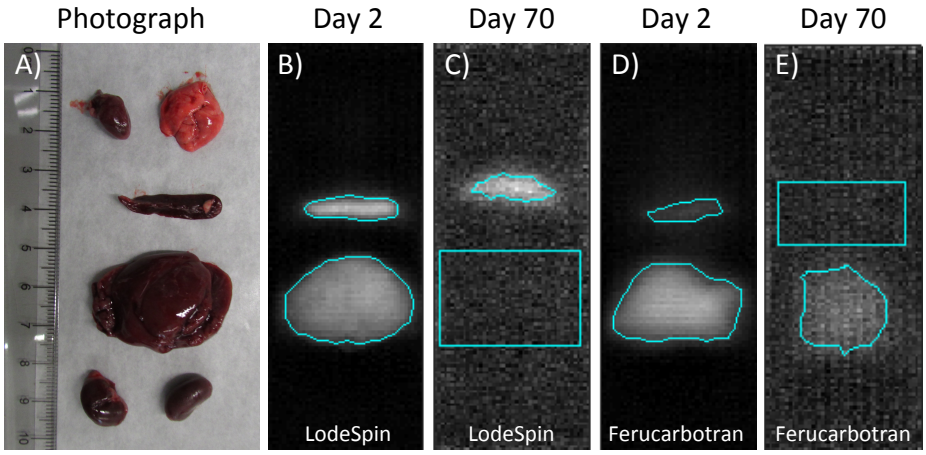

Figure 6.8: (A) Photograph of the extracted liver, spleen, kidneys, lungs and heart (rat 2 from Group 4). (B) MPI image of extracted organs at day 2 after the injection of LodeSpin (rat 2 from Group 4). (C) MPI image of extracted organs at day 70 after the injection of LodeSpin (rat 2 from Group 3). (D) MPI image of extracted organs at day 2 after the injection of Ferucarbotran (rat 2 from Group 2). (E) MPI image of extracted organs at day 70 after the injection of Ferucarbotran (rat 2 from Group 1). For both tracers, only the liver and spleen have an MPI signal at day 2. At day 70, LodeSpin only has a signal in the spleen and Ferucarbotran only has signal in the liver.

Figure 6.8A is a photograph of the extracted organs. For both tracers, only the liver and spleen were visible in MPI at day 2 (Figure 6.8B and D). At day 70, LodeSpin (LS-008) was only visible in the spleen (Figure 6.8C), as oppose to Ferucarbotran that was only visible in the liver (Figure 6.8E). Using the same region growing algorithm, an average signal was determined in an ROI drawn over liver and spleen and an average signal per gram of tissue was determined. Results are shown in Figure 6.9. This is in excellent agreement with *in vivo* data shown in Figure 6.6 and Figure 6.7.

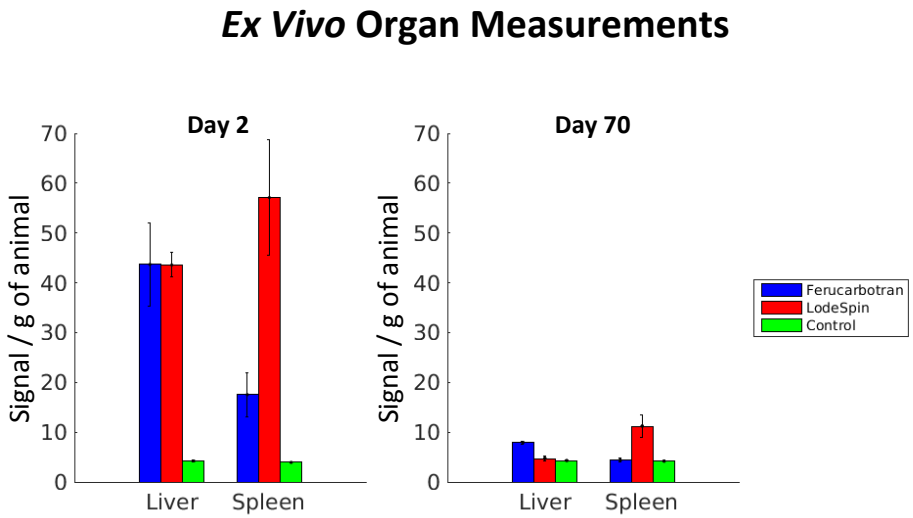

Figure 6.9: *Ex vivo* Organ measurements for Ferucarbotran and LodeSpin (LS-008) at day 2 and day 70. As with in vivo data, LodeSpin is mostly cleared by the spleen, while Ferucarbotran is mostly cleared by the liver. No signal was seen in the heart, lungs or kidneys.

6.6 Iron Clearance Validation with ICP

To verify that SPIOs are actually being cleared from liver and spleen, a total iron concentration was determined via a standard ICP-OES measurement (OptimaTM 5300 DV (PerkinElmer Inc., Waltham, MA). To prepare the samples for ICP measurement, each organ was first lyophilized for 2 days, and then ground into a homogeneous fine powder. A 10 to 20 mg sample was then digested in 70% HNO3 (trace metal grade) overnight and diluted to 2% HNO3 solution to match the concentration of ICP standards prepared for calibration. Concentration of each sample was then determined from the calibration curve and average iron content (in mg of Fe/ g tissue) was calculated.

At day 2, both liver and spleen in animals injected with SPIOS show elevated iron content as compared to the control animals. At day 72 the total iron concentration drops almost to the level of the control animals, which is consistent with MPI measurements.

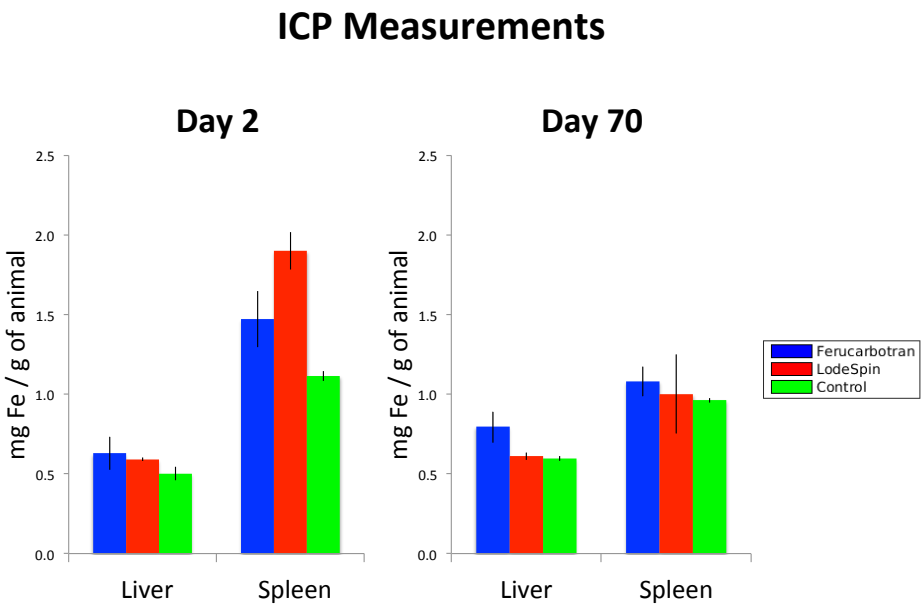

Figure 6.10: ICP Organ measurements for Ferucarbotran and LodeSpin (LS-008) at day 2 and day 70. At day 70, both LodeSpin and Ferucarbotran Iron levels are down to that of the control group.

6.7 Conclusions

In this experiment, we were able to successfully track the biodistribution and clearance of both tracers with MPI. The long circulation of LodeSpin (LS-008) makes it a good candidate for angiographic procedures. For both tracers, clearance is consistent with the rates reported in the literature for tracers cleared by the mononuclear phagocyte system (MPS) to the liver and spleen [69, 74, 75, 76, 77]. It appears that LodeSpin particles, which were designed for long circulation, were taken up by macrophages circulating in the blood and cleared to the spleen [69]. On the other hand, Ferucarbotran was almost immediately taken up by the Kupffer cells of the liver [69].

Chapter 7

Conclusion

In conclusion, we described two methods for imaging patients with Chronic Kidney Disease. These methods should be much safer alternatives of medical imaging for this population of patients, since they do not rely on an injection of harmful contrast agents. MR Saline Angiography shows great promise as an alternative method for imaging coronary arteries. On the other hand, MPI is an emerging imaging modality that shows great promise in areas of magnetic hyperthermia for non-invasive treatment of tumors, immune cell and stem cell tracking, non-targeted cancer imaging, and tracking of micron sized drug delivery mechanisms.

For MR Saline Angiography, shielding of the saline from the MRI RF pulses is paramount for sufficient contrast. However, a conventional catheter with RF shielding would heat surrounding tissue to dangerous levels. We showed that segmenting the RF Catheter significantly reduced heating while retaining the desired shielding characteristics. For the customized MR sequence, we showed that Multiple Inversion recovery prep with adiabatic pulses was able to robustly null multiple background tissues, while the RF catheter significantly increased flow-in time. In implementing Spectral Spatial pulses, we were able to exclude fat from the excitation to further increase flow-in time. The initial results from the real-time MR system are promising. However, further pulse sequence customization is required.

For MPI we were able to image vasculature *in vivo*. We have successfully demonstrated that MPI is able to track both short-term biodistribution and long-term clearance of SPIO particles. Both MPI and ICP measurement showed that the injected SPIOs were cleared from the system.

We aim to match X-ray angiography in contrast and speed with our safe saline contrast. Therefore, future work for MR Saline Angiography include scaling up the shielded catheter to large animal models and implementing the sequences on real-time imaging systems. Demonstrating saline angiography *in vivo* will be essential for the evaluation of the technique for clinical use. Furthermore, the shielded catheters need to be fine-tuned to match existing catheters for ease of transition into the clinic.

In MPI, the nanoparticle tracer is fundamental to the imaging technique itself. No MPI image exists without the MPI tracer. Thus, the development of tailored particles – whether

for long circulation time, for organ-specific targeting, or high resolution imaging – is crucial for every MPI imaging application. This work serves as a stepping stone for the *in vivo* evaluation of these emerging particles by assessing several fundamental nanoparticle properties, specifically biodistribution and clearance. In the future, this work will be extended to specific MPI applications such as cancer diagnosis, angiography and brain imaging.

Bibliography

[1] National Kidney Foundation. *About Chronic Kidney Disease*. URL: https://www.kidney.org/kidneydisease/aboutckd.

[2] Josef Coresh et al. "Prevalence of Chronic Kidney Disease in the United States". In: *JAMA* 298.17 (Nov. 2007), pp. 2038–2047. ISSN: 0098-7484. DOI: 10.1001/jama.298.17.2038. URL: http://jama.jamanetwork.com/article.aspx?doi=10.1001/jama.298.17.2038.

[3] George Dangas et al. "Contrast-induced nephropathy after percutaneous coronary interventions in relation to chronic kidney disease and hemodynamic variables." In: *The American journal of cardiology* 95.1 (Jan. 2005), pp. 13–9. ISSN: 0002-9149. DOI: 10.1016/j.amjcard.2004.08.056. URL: http://www.ncbi.nlm.nih.gov/pubmed/15619387.

[4] Ernesto L Schiffrin, Mark L Lipman, and J. F.E. Mann. "Chronic Kidney Disease: Effects on the Cardiovascular System". In: *Circulation* 116.1 (July 2007), pp. 85–97. ISSN: 0009-7322. DOI: 10.1161/CIRCULATIONAHA.106.678342.

[5] Dariush Mozaffarian et al. "Heart Disease and Stroke Statistics,–2016 Update". In: *Circulation* 133.4 (Jan. 2016), e38–e360. ISSN: 0009-7322. DOI: 10.1161/CIR.0000000000000350.

[6] "Comparison of global estimates of prevalence and risk factors for peripheral artery disease in 2000 and 2010: a systematic review and analysis". In: *The Lancet* 382.9901 (Oct. 2013), pp. 1329–1340. ISSN: 01406736. DOI: 10.1016/S0140-6736(13)61249-0. URL: http://dx.doi.org/10.1016/S0140-6736(13)61249-0%20http://linkinghub.elsevier.com/retrieve/pii/S0140673613612490.

[7] *Ionizing Radiation Exposure of the Population of the United States*. 160. National Council on Raiation Protection and Measurements, 2009, pp. 95–115.

[8] Crownover B.K. and Bepko J.L. "Appropriate and safe use of diagnostic imaging". In: *American Family Physician* 87 (2013), pp. 494–501. ISSN: 1532-0650. URL: http://www.aafp.org/afp/2013/0401/p494.pdf$%5Cbackslash$nhttp://ovidsp.ovid.com/ovidweb.cgi?T=JS%7B%5C&%7DPAGE=reference%7B%5C&%7DD=emed11%7B%5C&%7DNEWS=N%7B%5C&%7DAN=2013206181.

[9] Peter A McCullough et al. "Acute Renal Failure After Coronary Intervention: Incidence, Risk Factors, And Relationship to Mortality". In: *The American Journal of Medicine* 103.4 (1997), pp. 368–375. ISSN: 00029343. DOI: 10.1016/S0002-9343(97)00150-2.

[10] Peter McCullough. "Outcomes of contrast-induced nephropathy: Experience in patients undergoing cardiovascular intervention". In: *Catheterization and Cardiovascular Interventions* 67.3 (2006), pp. 335–343. ISSN: 15221946. DOI: 10.1002/ccd.20658.

[11] Stanley Goldfarb et al. "Contrast-Induced Acute Kidney Injury: Specialty-Specific Protocols for Interventional Radiology, Diagnostic Computed Tomography Radiology, and Interventional Cardiology". In: *Mayo Clinic Proceedings* 84.2 (Feb. 2009), pp. 170–179. ISSN: 00256196. DOI: 10.4065/84.2.170. URL: http://linkinghub.elsevier.com/retrieve/pii/S0025619611608252.

[12] Joshua R. Hwang et al. "Contrast Volume Use in Manual vs Automated Contrast Injection Systems for Diagnostic Coronary Angiography and Percutaneous Coronary Interventions". In: *Canadian Journal of Cardiology* 29.3 (2013), pp. 372–376. ISSN: 0828282X. DOI: 10.1016/j.cjca.2012.11.023. URL: http://dx.doi.org/10.1016/j.cjca.2012.11.023.

[13] Rekha Raju et al. "Reduced iodine load with CT coronary angiography using dual-energy imaging: A prospective randomized trial compared with standard coronary CT angiography". In: *Journal of Cardiovascular Computed Tomography* 8.4 (July 2014), pp. 282–288. ISSN: 19345925. DOI: 10.1016/j.jcct.2014.06.003. arXiv: NIHMS150003. URL: http://linkinghub.elsevier.com/retrieve/pii/S0039606006007173%20http://linkinghub.elsevier.com/retrieve/pii/S1934592514001531.

[14] Peter Lanzer. *Diagnostics of Vascular Diseases Principles and Technology*. Berlin, Heidelberg: Springer Berlin Heidelberg, 1997. ISBN: 978-3-642-64437-5.

[15] Abdulrahman Almutairi et al. "Dual energy CT angiography of peripheral arterial disease: Feasibility of using lower contrast medium volume". In: *PLoS ONE* 10.9 (2015), pp. 1–15. ISSN: 19326203. DOI: 10.1371/journal.pone.0139275.

[16] Kyongtae T. Bae. "Intravenous Contrast Medium Administration and Scan Timing at CT: Considerations and Approaches". In: *Radiology* 256.1 (2010), pp. 32–61. ISSN: 0033-8419. DOI: 10.1148/radiol.10090908. URL: http://radiology.rsna.org/content/256/1/32.abstract$%5Cbackslash$nhttp://radiology.rsna.org/content/256/1/32.full.pdf.

[17] Jesse Jones et al. "Radiation Dose From Medical Imaging: A Primer for Emergency Physicians". In: *Western Journal of Emergency Medicine* 13.2 (2012), pp. 202–210. ISSN: 1936900X. DOI: 10.5811/westjem.2011.11.6804. URL: http://www.escholarship.org/uc/item/95r6r7mz.

[18] Alessandro Napoli et al. "Peripheral Arterial Occlusive Disease : Diagnostic Performance and Effect on Therapeutic Management of 64-Section CT angiography". In: *Radiology* 261.3 (2011), pp. 976–986. ISSN: 1527-1315. DOI: 10.1148/radiol.11103564/-/DC1. URL: http://radiology.rsna.org/content/suppl/2011/10/03/radiol.11103564.DC1.

[19] Sang-Min Lee et al. "Silicon Strip Detector for a novel 2D dosimetric method for radiotherapy treatment verification". In: *Radiotherapy and Oncology* 15.4 (2012), pp. 176–180. ISSN: 15071367. DOI: 10.1016/j.rpor.2010.09.001. URL: http://www.pubmedcentral.nih.gov/articlerender.fcgi?artid=3216506%7B%5C&%7Dtool=pmcentrez%7B%5C&%7Drendertype=abstract$%5Cbackslash$nhttp://linkinghub.elsevier.com/retrieve/pii/S150713671000101X$%5Cbackslash$nhttp://linkinghub.elsevier.com/retrieve/pii/S0167814012703250$%5Cbackslash$nhttp://link.aip.org/link/JVTAD6/v19/i5/p2116/s1%7B%5C&%7DAgg=doi$%5Cbackslash$nhttp://stacks.iop.org/1742-6596/194/i=13/a=132035?key=crossref.5f9c28ce2043b3bad8ac01db20619fc2$%5Cbackslash$nhttp://link.springer.com/10.1007/978-3-642-00829-0$%5Cbackslash$nhttp://www.ncbi.nlm.nih.gov/pubmed/23041410$%5Cbackslash$nhttp://www.ncbi.nlm.nih.gov/.

[20] Eugene C Lin. "Radiation Risk From Medical Imaging". In: *Mayo Clinic Proceedings* 85.12 (2010), pp. 1142–1146. ISSN: 0025-6196. DOI: http://dx.doi.org/10.4065/mcp.2010.0260. URL: http://www.sciencedirect.com/science/article/pii/S0025619611603698.

[21] Joachim H. Ix et al. "Association of chronic kidney disease with clinical outcomes after coronary revascularization: The arterial revascularization therapies study (ARTS)". In: *American Heart Journal* 149.3 (2005), pp. 512–519. ISSN: 00028703. DOI: 10.1016/j.ahj.2004.10.010.

[22] R.W. Katzberg and C. Haller. "Contrast-induced nephrotoxicity: Clinical landscape". In: *Kidney International Supplement* 100 (Apr. 2006), pS3.

[23] Martin R Prince et al. "Incidence of nephrogenic systemic fibrosis at two large medical centers." In: *Radiology* 248.3 (2008), pp. 807–816. ISSN: 0033-8419. DOI: 10.1148/radiol.2483071863.

[24] Aneet Deo, Mitchell Fogel, and Shawn E. Cowper. "Nephrogenic systemic fibrosis: A population study examining the relationship of disease development to gadolinium exposure". In: *Clinical Journal of the American Society of Nephrology* 2.2 (2007), pp. 264–267. ISSN: 15559041. DOI: 10.2215/CJN.03921106.

[25] Elizabeth a Sadowski et al. "Nephrogenic systemic fibrosis: risk factors and incidence estimation." In: *Radiology* 243.1 (2007), pp. 148–157. ISSN: 0033-8419. DOI: 10.1148/radiol.2431062144.

[26] Dale R. Broome. "Nephrogenic systemic fibrosis associated with gadolinium based contrast agents: A summary of the medical literature reporting". In: *European Journal of Radiology* 66.2 (2008), pp. 230–234. ISSN: 0720048X. DOI: 10.1016/j.ejrad.2008.02.011.

[27] Chris Brede and Vinod Labhasetwar. "Applications of nanoparticles in the detection and treatment of kidney diseases." In: *Advances in chronic kidney disease* 20.6 (2013), pp. 454–65. ISSN: 1548-5609. DOI: 10.1053/j.ackd.2013.07.006. URL: http://www.sciencedirect.com/science/article/pii/S1548559513001109.

[28] Min Lu et al. "FDA report: Ferumoxytol for intravenous iron therapy in adult patients with chronic kidney disease". In: *American Journal of Hematology* 85.5 (2010), pp. 315–319. ISSN: 03618609. DOI: 10.1002/ajh.21656.

[29] Greg J Stanisz et al. "T1, T2 relaxation and magnetization transfer in tissue at 3T." In: *Magnetic resonance in medicine : official journal of the Society of Magnetic Resonance in Medicine / Society of Magnetic Resonance in Medicine* 54.3 (Sept. 2005), pp. 507–12. ISSN: 0740-3194. DOI: 10.1002/mrm.20605. URL: http://www.ncbi.nlm.nih.gov/pubmed/16086319.

[30] Garry E Gold et al. "Musculoskeletal MRI at 3.0 T: relaxation times and image contrast." In: *AJR. American journal of roentgenology* 183.2 (Aug. 2004), pp. 343–51. ISSN: 0361-803X. DOI: 10.2214/ajr.183.2.1830343. URL: http://www.ajronline.org/content/183/2/343.long%20http://www.ncbi.nlm.nih.gov/pubmed/15269023.

[31] Bernhard Gleich and Jürgen Weizenecker. "Tomographic imaging using the nonlinear response of magnetic particles". In: *Nature* 435.7046 (June 2005), pp. 1214–1217. ISSN: 0028-0836. DOI: 10.1038/nature03808. URL: http://www.ncbi.nlm.nih.gov/pubmed/15988521%20http://www.nature.com/doifinder/10.1038/nature03808.

[32] Emine U Saritas et al. "Magnetic Particle Imaging (MPI) for NMR and MRI researchers". In: *Journal of Magnetic Resonance* 229 (Apr. 2013), pp. 116–126. ISSN: 10907807. DOI: 10.1016/j.jmr.2012.11.029. URL: http://dx.doi.org/10.1016/j.jmr.2012.11.029%20http://linkinghub.elsevier.com/retrieve/pii/S1090780712003734.

[33] Bo Zheng et al. "Magnetic Particle Imaging tracks the long-term fate of in vivo neural cell implants with high image contrast". In: *Scientific Reports* 5 (Sept. 2015), p. 14055. ISSN: 2045-2322. DOI: 10.1038/srep14055. URL: http://www.nature.com/articles/srep14055.

[34] Bo Zheng et al. "Quantitative Magnetic Particle Imaging Monitors the Transplantation, Biodistribution, and Clearance of Stem Cells In Vivo". In: *Theranostics* 6.3 (2016), pp. 291–301. ISSN: 1838-7640. DOI: 10.7150/thno.13728. URL: http://thno.org/v06p0291.

[35] J Rahmer et al. "Nanoparticle encapsulation in red blood cells enables blood-pool magnetic particle imaging hours after injection." In: *Physics in medicine and biology* 58.12 (2013), pp. 3965–77. ISSN: 1361-6560. DOI: 10.1088/0031-9155/58/12/3965. URL: http://www.ncbi.nlm.nih.gov/pubmed/23685712.

[36] Patrick Goodwill et al. "In Vivo and Ex vivo experimental MPI angiography with high selection field strength and tailored SPIO nanoparticles". In: *2015 5th International Workshop on Magnetic Particle Imaging (IWMPI)*. IEEE, Mar. 2015, pp. 1–1. ISBN: 978-1-4799-7269-2. DOI: 10.1109/IWMPI.2015.7106988. URL: http://ieeexplore.ieee.org/xpl/articleDetails.jsp?arnumber=7106988%7B%5C&%7Dfilter%7B%%7D3DAND%7B%%7D28p%7B%5C_%7DIS%7B%5C_%7DNumber%7B%%7D3A7106981%7B%%7D29%20http://ieeexplore.ieee.org/lpdocs/epic03/wrapper.htm?arnumber=7106988.

[37] R Matthew Ferguson et al. "Optimizing magnetite nanoparticles for mass sensitivity in magnetic particle imaging". In: *Medical physics* 38.3 (2011), pp. 1619–1626.

[38] Patrick William Goodwill et al. "X-Space MPI: Magnetic Nanoparticles for Safe Medical Imaging". In: *Advanced Materials* 24.28 (2012), pp. 3870–3877. ISSN: 1521-4095. DOI: 10.1002/adma.201200221. URL: http://dx.doi.org/10.1002/adma.201200221.

[39] Patrick W Goodwill and Steven M Conolly. "The X-space formulation of the magnetic particle imaging process: 1-D signal, resolution, bandwidth, SNR, SAR, and magnetostimulation." In: *IEEE transactions on medical imaging* 29.11 (Nov. 2010), pp. 1851–9. ISSN: 1558-254X. DOI: 10.1109/TMI.2010.2052284. URL: http://www.ncbi.nlm.nih.gov/pubmed/20529726.

[40] Gregory J Dehmer et al. "A contemporary view of diagnostic cardiac catheterization and percutaneous coronary intervention in the United States: a report from the Cath-PCI Registry of the National Cardiovascular Data Registry, 2010 through June 2011." In: *Journal of the American College of Cardiology* 60.20 (Nov. 2012), pp. 2017–31. ISSN: 1558-3597. DOI: 10.1016/j.jacc.2012.08.966. URL: http://www.ncbi.nlm.nih.gov/pubmed/23083784.

[41] Justin J. Konkle et al. "Twenty-fold acceleration of 3D projection reconstruction MPI". In: *Biomedizinische Technik/Biomedical Engineering* 58.6 (Jan. 2013), pp. 565–576. ISSN: 1862-278X. DOI: 10.1515/bmt-2012-0062. URL: http://www.degruyter.com/view/j/bmte.2013.58.issue-6/bmt-2012-0062/bmt-2012-0062.xml.

[42] Silvio Dutz and Rudolf Hergt. "Magnetic particle hyperthermia–a promising tumour therapy?" In: *Nanotechnology* 25.45 (2014), p. 452001. ISSN: 1361-6528. DOI: 10.1088/0957-4484/25/45/452001. URL: http://www.ncbi.nlm.nih.gov/pubmed/25337919.

[43] Rudolf Hergt et al. "Magnetic particle hyperthermia: nanoparticle magnetism and materials development for cancer therapy". In: *Journal of Physics: Condensed Matter* 18.38 (2006), S2919–S2934. ISSN: 0953-8984. DOI: 10.1088/0953-8984/18/38/S26.

[44] Masashige Shinkai. "Functional magnetic particles for medical application". In: *Journal of Bioscience and Bioengineering* 94.6 (2002), pp. 606–613. ISSN: 13891723. DOI: 10.1016/S1389-1723(02)80202-X.

[45] Eric T Ahrens and Jeff W M Bulte. "Tracking immune cells in vivo using magnetic resonance imaging." In: *Nature reviews. Immunology* 13.10 (2013), pp. 755–63. ISSN: 1474-1741. DOI: 10.1038/nri3531. URL: http://dx.doi.org/10.1038/nri3531.

[46] Hiroshi Maeda, Hideaki Nakamura, and Jun Fang. "The EPR effect for macromolecular drug delivery to solid tumors: Improvement of tumor uptake, lowering of systemic toxicity, and distinct tumor imaging in vivo". In: *Advanced Drug Delivery Reviews* 65.1 (2013), pp. 71–79. ISSN: 0169409X. DOI: 10.1016/j.addr.2012.10.002. URL: http://dx.doi.org/10.1016/j.addr.2012.10.002.

[47] Theresa M. Allen and Pieter R. Cullis. "Liposomal drug delivery systems: From concept to clinical applications". In: *Advanced Drug Delivery Reviews* 65.1 (2013), pp. 36–48. ISSN: 0169409X. DOI: 10.1016/j.addr.2012.09.037. URL: http://dx.doi.org/10.1016/j.addr.2012.09.037.

[48] C O'Callaghan and P W Barry. "The science of nebulised drug delivery." In: *Thorax* 52 Suppl 2.Suppl 2 (1997), S31–S44. ISSN: 0040-6376. DOI: 10.1136/thx.52.2008.S31.

[49] Shihong Li et al. "Novel multifunctional theranostic liposome drug delivery system: Construction, characterization, and multimodality MR, near-infrared fluorescent, and nuclear imaging". In: *Bioconjugate Chemistry* 23.6 (2012), pp. 1322–1332. ISSN: 10431802. DOI: 10.1021/bc300175d. arXiv: NIHMS150003.

[50] SM Park et al. "MRI safety: RF-induced heating near straight wires". In: *IEEE Transactions on Magnetics* 41.10 (Oct. 2005), pp. 4197–4199. ISSN: 0018-9464. DOI: 10.1109/TMAG.2005.854803. URL: http://ieeexplore.ieee.org/xpls/abs%7B%5C_%7Dall.jsp?arnumber=1519579%20http://ieeexplore.ieee.org/lpdocs/epic03/wrapper.htm?arnumber=1519579.

[51] Cristina Armenean et al. "RF-induced temperature elevation along metallic wires in clinical magnetic resonance imaging: influence of diameter and length." In: *Magnetic resonance in medicine : official journal of the Society of Magnetic Resonance in Medicine / Society of Magnetic Resonance in Medicine* 52.5 (Nov. 2004), pp. 1200–6. ISSN: 0740-3194. DOI: 10.1002/mrm.20246. URL: http://www.ncbi.nlm.nih.gov/pubmed/15508156.

[52] Gary Fenical; In Compliance. *The Basic Principles of Shielding*. 2014. URL: http://incompliancemag.com/article/the-basic-principles-of-shielding/.

[53] a Haase et al. "FLASH imaging: Rapid NMR imaging using low flip-angle pulses". In: *Journal of Magnetic Resonance* 67 (Dec. 1986), pp. 258–266. ISSN: 10907807. DOI: 10.1016/j.jmr.2011.09.021. URL: http://www.ncbi.nlm.nih.gov/pubmed/22152368%20http://linkinghub.elsevier.com/retrieve/pii/S1090780711003338.

[54] Loren A. Zaremba. "FDA Guidelines for Magnetic Resonance Equipment Safety". In: *Proceedings of the American Association of Physicists in Medicine* (2002).

[55] wikipedia. *Specific absorption rate*. URL: https://en.wikipedia.org/wiki/Specific_absorption_rate.

[56] W R Nitz et al. "On the heating of linear conductive structures as guide wires and catheters in interventional MRI." In: *Journal of magnetic resonance imaging : JMRI* 13.1 (Jan. 2001), pp. 105–14. ISSN: 1053-1807. URL: http://www.ncbi.nlm.nih.gov/pubmed/11169811.

[57] C.J. Yeung, R.C. Susil, and Ergin Atalar. "Modeling of RF heating due to metal implants in MRI". In: *IEEE Antennas and Propagation Society International Symposium (IEEE Cat. No.02CH37313)*. Vol. 1. IEEE, 2002, pp. 823–826. ISBN: 0-7803-7330-8. DOI: 10.1109/APS.2002.1016469. URL: http://ieeexplore.ieee.org/lpdocs/epic03/wrapper.htm?arnumber=1016469.

[58] Jian-Ming Jin. "Electromagnetics in magnetic resonance imaging". In: *IEEE Antennas and Propagation Magazine* 40.6 (1998), pp. 7–22. ISSN: 10459243. DOI: 10.1109/74.739187. URL: http://libproxy.gist.ac.kr/bb85077/%7B%5C_%7DLib%7B%5C_%7DProxy%7B%5C_%7DUrl/ieeexplore.ieee.org/articleDetails.jsp?arnumber=739187.

[59] Italian National Research Council - Institute for Applied Physics. *Dielectric Properties of Body Tissues*. URL: http://niremf.ifac.cnr.it/tissprop/htmlclie/htmlclie.php.

[60] The Foundation for Research on Information Technologies in Society. *Heat Capacity of Tissue*. URL: http://www.itis.ethz.ch/virtual-population/tissue-properties/database/heat-capacity/.

[61] EXW Foxboro. *Table Of Conductivity vs. Concentration For Common Solutions*. URL: http://myweb.wit.edu/sandinic/Research/conductivity%20v%20concentration.pdf.

[62] Juan M Santos, Graham a Wright, and John M Pauly. "Flexible real-time magnetic resonance imaging framework." In: *Conference proceedings : ... Annual International Conference of the IEEE Engineering in Medicine and Biology Society. IEEE Engineering in Medicine and Biology Society. Conference* 2 (2004), pp. 1048–1051. ISSN: 1557-170X. DOI: 10.1109/IEMBS.2004.1403343.

[63] Joris Tchouala Nofiele and Hai-Ling Margaret Cheng. "Ultrashort Echo Time for Improved Positive-Contrast Manganese-Enhanced MRI of Cancer". In: *PLoS ONE* 8.3 (Mar. 2013), pp. 1–8. DOI: 10.1371/journal.pone.0058617. URL: http://dx.doi.org/10.1371/journal.pone.0058617.

[64] J P Mugler and J R Brookeman. "Three-dimensional magnetization-prepared rapid gradient-echo imaging (3D MP RAGE)." In: *Magnetic resonance in medicine : official journal of the Society of Magnetic Resonance in Medicine / Society of Magnetic Resonance in Medicine* 15.1 (July 1990), pp. 152–7. ISSN: 0740-3194. URL: http://www.ncbi.nlm.nih.gov/pubmed/2374495.

[65] M.S Silver, R.I Joseph, and D.I Hoult. "Selective spin inversion in nuclear magnetic resonance and coherent optics through an exact solution of the Bloch-Riccati equation". In: *Physical Review A* 31.4 (Apr. 1985), pp. 2753–2755. ISSN: 0556-2791. DOI: 10.1103/PhysRevA.31.2753. URL: http://linkinghub.elsevier.com/retrieve/pii/0022236484901811%20http://link.aps.org/doi/10.1103/PhysRevA.31.2753.

[66] Steven Conolly, Dwight Nishimura, and Albert Macovski. "A selective adiabatic spin-echo pulse". In: *Journal of Magnetic Resonance (1969)* 83.2 (1989), pp. 324–334. ISSN: 00222364. DOI: 10.1016/0022-2364(89)90194-7.

[67] S Mani et al. "Background suppression with multiple inversion recovery nulling: applications to projective angiography." In: *Magnetic resonance in medicine : official journal of the Society of Magnetic Resonance in Medicine / Society of Magnetic Resonance in Medicine* 37.6 (June 1997), pp. 898–905. ISSN: 0740-3194. URL: http://www.ncbi.nlm.nih.gov/pubmed/9178242.

[68] C H Meyer et al. "Simultaneous spatial and spectral selective excitation." In: *Magnetic resonance in medicine : official journal of the Society of Magnetic Resonance in Medicine / Society of Magnetic Resonance in Medicine* 15.2 (Aug. 1990), pp. 287–304. ISSN: 0740-3194. URL: http://www.ncbi.nlm.nih.gov/pubmed/2392053.

[69] Luo Gu et al. "In vivo clearance and toxicity of monodisperse iron oxide nanocrystals". In: *ACS Nano* 6.6 (2012), pp. 4947–4954. ISSN: 19360851. DOI: 10.1021/nn300456z.

[70] Maha R a Abdollah et al. "Prolonging the circulatory retention of SPIONs using dextran sulfate: in vivo tracking achieved by functionalisation with near-infrared dyes." In: *Faraday discussions* 00 (2014), pp. 1–18. ISSN: 1359-6640. DOI: 10.1039/c4fd00114a. URL: http://www.ncbi.nlm.nih.gov/pubmed/25298115.

[71] K. Lüdtke-Buzug et al. "Particle-size distribution of dextran- and carboxydextran-coated superparamagnetic nanoparticles for magnetic particle imaging". In: *IFMBE Proceedings* 25.8 (2009), pp. 226–229. ISSN: 16800737. DOI: 10.1007/978-3-642-03887-7-63.

[72] Richard Mathew Ferguson et al. "Tailoring the magnetic and pharmacokinetic properties of iron oxide magnetic particle imaging tracers". In: *Biomedizinische Technik/Biomedical Engineering* 58.6 (Jan. 2013), pp. 493–507. ISSN: 1862-278X. DOI: 10.1515/bmt-2012-0058. URL: http://www.degruyter.com/view/j/bmte.2013.58.issue-6/bmt-2012-0058/bmt-2012-0058.xml.

[73] Amit P. Khandhar et al. "Monodisperse magnetite nanoparticle tracers for in vivo magnetic particle imaging". In: *Biomaterials* 34.15 (May 2013), pp. 3837–3845. ISSN: 01429612. DOI: 10.1016/j.biomaterials.2013.01.087. URL: http://linkinghub.elsevier.com/retrieve/pii/S0142961213001427.

[74] Michael Levy et al. "Long term in vivo biotransformation of iron oxide nanoparticles". In: *Biomaterials* 32.16 (2011), pp. 3988–3999. ISSN: 01429612. DOI: 10.1016/j.biomaterials.2011.02.031. URL: http://linkinghub.elsevier.com/retrieve/pii/S0142961211001839.

[75] Ting Liu et al. "Quantitative Evaluation of the Reticuloendothelial System Function with Dynamic MRI". In: *PLoS ONE* 9.8 (2014), e103576. ISSN: 1932-6203. DOI: 10.1371/journal.pone.0103576. URL: http://dx.plos.org/10.1371/journal.pone.0103576.

[76] F Roohi et al. "Studying the effect of particle size and coating type on the blood kinetics of superparamagnetic iron oxide nanoparticles". In: *Int J Nanomedicine* 7 (2012), pp. 4447–4458. ISSN: 1178-2013. DOI: 10.2147/IJN.S33120. URL: http://www.ncbi.nlm.nih.gov/pubmed/22927759.

[77] Constantin Scharlach, Carsten Warmuth, and Eyk Schellenberger. "Determination of blood circulation times of superparamagnetic iron oxide nanoparticles by T2* relaxometry using ultrashort echo time (UTE) MRI". In: *Magnetic Resonance Imaging* (2015). ISSN: 0730725X. DOI: 10.1016/j.mri.2015.06.017. URL: http://linkinghub.elsevier.com/retrieve/pii/S0730725X15001629.